

# Jordan Journal of Mechanical and Industrial Engineering (JJMIE)

JJMIE is a high-quality scientific journal devoted to fields of Mechanical and Industrial Engineering. It is published by Hashemite University in corporation with the Jordanian Scientific Research Support Fund.

## EDITORIAL BOARD

---

### Editor-in-Chief

Prof. Ahmed M. Al-Ghandoor

### Assistant Editor

Dr. Mohammad A Gharaibeh.

### Editorial board

Prof. **Mohammad Ahmad Hamdan**  
University of Jordan

Prof. **Naseem Sawaqed**  
Mutah University

Prof. **Amin Al Robaidi**  
Al Balqa Applied University

Prof. **Naser Al-Huniti**  
University of Jordan

Prof. **Mohammad Hayajneh**  
Jordan University of Science and Technology

## THE INTERNATIONAL ADVISORY BOARD

---

**Abu-Qudais, Mohammad**  
Jordan University of Science & Technology, Jordan

**Abu-Mulaweh, Hosni**  
Purdue University at Fort Wayne, USA

**Afaneh Abdul-Hafiz**  
Robert Bosch Corporation, USA

**Afonso, Maria Dina**  
Institute Superior Tecnico, Portugal

**Badiru, Adedji B.**  
The University of Tennessee, USA

**Bejan, Adrian**  
Duke University, USA

**Chalhoub, Nabil G.**  
Wayne State University, USA

**Cho, Kyu-Kab**  
Pusan National University, South Korea

**Dincer, Ibrahim**  
University of Ontario Institute of Technology,  
Canada

**Douglas, Roy**  
Queen's University, U. K

**El Bassam, Nasir**  
International Research Center for Renewable  
Energy, Germany

**Haik, Yousef**  
United Arab Emirates University, UAE

**Jaber, Jamal**  
Al- Balqa Applied University, Jordan

**Jubran, Bassam**  
Ryerson University, Canada

**Kakac, Sadik**  
University of Miami, USA

**Khalil, Essam-Eddin**  
Cairo University, Egypt

**Mutoh, Yoshiharu**  
Nagaoka University of Technology, Japan

**Pant, Durbin**  
Iowa State University, USA

**Riffat, Saffa**  
The University of Nottingham, U. K

**Saghir, Ziad**  
Ryerson University, Canada

**Sarkar, MD. Abdur Rashid**  
Bangladesh University of Engineering &  
Technology, Bangladesh

**Signer, Dennis**  
Wichita State University, USA

**Sopian, Kamaruzzaman**  
University Kebangsaan Malaysia, Malaysia

**Tzou, Gow-Yi**  
Yung-Ta Institute of Technology and Commerce,  
Taiwan

## EDITORIAL BOARD SUPPORT TEAM

---

### Language Editor

Dr. Qusai Al-Debyan

### Publishing Layout

Eng. Ali Abu Salimeh

## SUBMISSION ADDRESS:

---

Prof. Ahmed Al-Ghandoor, Editor-in-Chief  
Jordan Journal of Mechanical & Industrial Engineering,  
Hashemite University,  
PO Box 330127, Zarqa, 13133 , Jordan  
E-mail: jjmie@hu.edu.jo



Hashemite Kingdom of Jordan



Hashemite University

Jordan Journal of  
Mechanical and Industrial Engineering

JJMIE

*An International Peer-Reviewed Scientific Journal*  
*Financed by Scientific Research Support Fund*

<http://jjmie.hu.edu.jo/>

ISSN 1995-6665

# Jordan Journal of Mechanical and Industrial Engineering (JJMIE)

JJMIE is a high-quality scientific journal devoted to fields of Mechanical and Industrial Engineering. It is published by The Jordanian Ministry of Higher Education and Scientific Research in corporation with Hashemite University.

**Introduction:** The Editorial Board is very committed to build the Journal as one of the leading international journals in mechanical and industrial engineering sciences in the next few years. With the support of the Ministry of Higher Education and Scientific Research and Jordanian Universities, it is expected that a heavy resource to be channeled into the Journal to establish its international reputation. The Journal's reputation will be enhanced from arrangements with several organizers of international conferences in publishing selected best papers of the conference proceedings.

**Aims and Scope:** *Jordan Journal of Mechanical and Industrial Engineering* (JJMIE) is a refereed international journal to be of interest and use to all those concerned with research in various fields of, or closely related to, mechanical and industrial engineering disciplines. *Jordan Journal of Mechanical and Industrial Engineering* aims to provide a highly readable and valuable addition to the literature which will serve as an indispensable reference tool for years to come. The coverage of the journal includes all new theoretical and experimental findings in the fields of mechanical and industrial engineering or any closely related fields (Materials, Manufacturing, Management, Design, Thermal and Fluid, Energy, Control, Mechatronics, and Biomedical). The journal also encourages the submission of critical review articles covering advances in recent research of such fields as well as technical notes.

## Guide for Authors

---

### **Manuscript Submission:**

High-quality submissions to this new journal are welcome now and manuscripts may be either submitted online or email.

**Online:** For online and email submission upload one copy of the full paper including graphics and all figures at the online submission site, accessed via <http://jjmie.hu.edu.jo>. The manuscript must be written in MS Word 2010 Format. All correspondence, including notification of the Editor's decision and requests for revision, takes place by e-mail and via the Author's homepage, removing the need for a hard-copy paper trail.

### **Submission address and contact:**

Prof. Ahmed Al-Ghandoor  
Editor-in-Chief  
*Jordan Journal of Mechanical & Industrial Engineering*,  
Hashemite University,  
PO Box 330127, Zarqa, 13115, Jordan  
E-mail: [jjmie@hu.edu.jo](mailto:jjmie@hu.edu.jo)

**Types of contributions:** Original research papers and Technical reports

**Corresponding author:** Clearly indicate who is responsible for correspondence at all stages of refereeing and publication, including post-publication. Ensure that telephone and fax numbers (with country and area code) are provided in addition to the e-mail address and the complete postal address. Full postal addresses must be given for all co-authors.

**Original material:** Submission of an article implies that the work described has not been published previously (except in the form of an abstract or as part of a published lecture or academic thesis), that it is not under consideration for publication elsewhere, that its publication is approved by all authors and that, if accepted, it will not be published elsewhere in the same form, in English or in any other language, without the written consent of the Publisher. Authors found to be deliberately contravening the submission guidelines on originality and exclusivity shall not be considered for future publication in this journal.

**Withdrawing:** If the author chooses to withdraw his article after it has been assessed, he shall reimburse JJMIE with the cost of reviewing the paper.

### **Manuscript Preparation:**

---

**General:** Editors reserve the right to adjust style to certain standards of uniformity. Original manuscripts are discarded after publication unless the Publisher is asked to return original material after use. Please use MS Word 2010 for the text of your manuscript.

**Structure:** Follow this order when typing manuscripts: Title, Authors, Authors title, Affiliations, Abstract, Keywords, Introduction, Main text, Conclusions, Acknowledgements, Appendix, References, Figure Captions, Figures and then Tables. Please supply figures imported into the text AND also separately as original graphics files. Collate acknowledgements in a separate section at the end of the article and do not include them on the title page, as a footnote to the title or otherwise.

**Text Layout:** Use 1.5 line spacing and wide (3 cm) margins. Ensure that each new paragraph is clearly indicated. Present tables and figure legends on separate pages at the end of the manuscript. If possible, consult a recent issue of the journal to become familiar with layout and conventions. All footnotes (except for table and corresponding author footnotes) should be identified with superscript Arabic numbers. To conserve space, authors are requested to mark the less important parts of the paper (such as records of experimental results) for printing in smaller type. For long papers (more than 4000 words) sections which could be deleted without destroying either the sense or the continuity of the paper should be indicated as a guide for the editor. Nomenclature should conform to that most frequently used in the scientific field concerned. Number all pages consecutively; use 12 or 10 pt font size and standard fonts.

**Corresponding author:** Clearly indicate who is responsible for correspondence at all stages of refereeing and publication, including post-publication. The corresponding author should be identified with an asterisk and footnote. Ensure that telephone and fax numbers (with country and area code) are provided in addition to the e-mail address and the complete postal address. Full postal addresses must be given for all co-authors. Please consult a recent journal paper for style if possible.

**Abstract:** A self-contained abstract outlining in a single paragraph the aims, scope and conclusions of the paper must be supplied.

**Keywords:** Immediately after the abstract, provide a maximum of six keywords (avoid, for example, 'and', 'of'). Be sparing with abbreviations: only abbreviations firmly established in the field may be eligible.

**Symbols:** All Greek letters and unusual symbols should be identified by name in the margin, the first time they are used.

**Units:** Follow internationally accepted rules and conventions: use the international system of units (SI). If other quantities are mentioned, give their equivalent in SI.

**Maths:** Number consecutively any equations that have to be displayed separately from the text (if referred to explicitly in the text).

**References:** All publications cited in the text should be presented in a list of references following the text of the manuscript.

*Text:* Indicate references by number(s) in square brackets in line with the text. The actual authors can be referred to, but the reference number(s) must always be given.

*List:* Number the references (numbers in square brackets) in the list in the order in which they appear in the text.

**Examples:**

**Reference to a journal publication:**

[1] M.S. Mohsen, B.A. Akash, "Evaluation of domestic solar water heating system in Jordan using analytic hierarchy process". Energy Conversion & Management, Vol. 38 (1997) No. 9, 1815-1822.

**Reference to a book:**

[2] Strunk Jr W, White EB. The elements of style. 3rd ed. New York: Macmillan; 1979.

**Reference to a conference proceeding:**

[3] B. Akash, S. Odeh, S. Nijmeh, "Modeling of solar-assisted double-tube evaporator heat pump system under local climate conditions". 5th Jordanian International Mechanical Engineering Conference, Amman, Jordan, 2004.

**Reference to a chapter in an edited book:**

[4] Mettam GR, Adams LB. How to prepare an electronic version of your article. In: Jones BS, Smith RZ, editors. Introduction to the electronic age, New York: E-Publishing Inc; 1999, p. 281-304

**Free Online Color :** If, together with your accepted article, you submit usable color and black/white figures then the journal will ensure that these figures will appear in color on the journal website electronic version.

**Tables:** Tables should be numbered consecutively and given suitable captions and each table should begin on a new page. No vertical rules should be used. Tables should not unnecessarily duplicate results presented elsewhere in the manuscript (for example, in graphs). Footnotes to tables should be typed below the table and should be referred to by superscript lowercase letters.

**Notification:** Authors will be notified of the acceptance of their paper by the editor. The Publisher will also send a notification of receipt of the paper in production.

**Copyright:** All authors must sign the Transfer of Copyright agreement before the article can be published. This transfer agreement enables Jordan Journal of Mechanical and Industrial Engineering to protect the copyrighted material for the authors, but does not relinquish the authors' proprietary rights. The copyright transfer covers the exclusive rights to reproduce and distribute the article, including reprints, photographic reproductions, microfilm or any other reproductions of similar nature and translations.

**Proof Reading:** One set of page proofs in MS Word 2010 format will be sent by e-mail to the corresponding author, to be checked for typesetting/editing. The corrections should be returned within **48 hours**. No changes in, or additions to, the accepted (and subsequently edited) manuscript will be allowed at this stage. Proofreading is solely the author's responsibility. Any queries should be answered in full. Please correct factual errors only, or errors introduced by typesetting. Please note that once your paper has been proofed we publish the identical paper online as in print.

**Author Benefits:**

*No page charges:* Publication in this journal is free of charge.

*Free offprints:* One journal issues of which the article appears will be supplied free of charge to the corresponding author and additional offprint for each co-author. Corresponding authors will be given the choice to buy extra offprints before printing of the article.



<b>PAGES</b>	<b>PAPERS</b>
161 - 169	<b>Nonlinear Natural Frequencies and Primary Resonance of Euler-Bernoulli Beam with Initial Deflection using Nonlocal Elasticity Theory.</b> <i>Ma'en S. Sari , Ahmad Al-Qaisia.</i>
171 - 177	<b>Parallel Translating Mechanism Process-Oriented Mathematical Model and 3-D Model for Cylindrical Gears with Curvilinear Shaped Teeth.</b> <i>CHANG Qinglin, HOU Li</i>
179– 188	<b>Multimode Input Shaping Control of Flexible Robotic Manipulators Using Frequency-Modulation.</b> <i>Ziyad Masoud , Mohammad Nazzal , Khaled Alhazza</i>
189– 198	<b>OPTIMIZATION OF VOLUMETRIC WEAR RATE OF AA7075-TiC METAL MATRIX COMPOSITE BY USING TAGUCHI TECHNIQUE.</b> <i>V.RamakoteswaraRao , N.Ramanaiah , M.M.M.Sarcar</i>
199– 203	<b>Greenhouse Gas Emissions Reduction Potential of Jordan's Utility Scale Wind and Solar Projects.</b> <i>Nidal Hussein</i>
205– 210	<b>Load Characteristics of Pick Cutting Coal Seams with Coal and Rock Interface.</b> <i>Chenxu Luo, Shuangxi JING , Xiaoming HAN , Yu LIU , Changlong Du</i>
211– 214	<b>Improving Mixing in Water Aeration Tanks Using Innovative Self-Powered Mixer and Power Reclamation from Aeration Tank.</b> <i>Ammar A. T. Alkhalidi , Patrick Bryar , Ryo S. Amano</i>
215– 229	<b>Novel Approach to Enhance the Performance of Production Systems Using Lean Tools.</b> <i>Hazem Kaylani , Ahmad Almuhtady , Anas M. Atieh .</i>

---



# Nonlinear Natural Frequencies and Primary Resonance of Euler-Bernoulli Beam with Initial Deflection using Nonlocal Elasticity Theory

Ma'en S. Sari<sup>a,\*</sup>, Ahmad Al-Qaisia<sup>b</sup>

<sup>a</sup> Department of Mechanical and Maintenance Engineering, German Jordanian university, Amman 11180, Jordan

<sup>b</sup> Department of Mechanical Engineering, The University of Jordan, Amman 11942, Jordan

Received Sept., 5, 2016

Accepted Oct., 20, 2016

## Abstract

In the present work, we study the primary responses of Euler-Bernoulli beam with initial imperfection/rise. The nonlocal elasticity theory was used to derive the mathematical model to account for the scale effect of the considered beam. One type of beams was considered in the analysis; simply supported beam. The multi-mode approach was used to obtain the reduced nonlinear temporal equations of motion that contain quadratic and cubic nonlinear terms. The method of multiple-scales was applied to obtain approximate analytical solutions for the nonlinear natural frequencies in addition to the primary and resonance responses. The obtained results were presented over a selected range of physical parameters for the two types of beams such as; beam initial rise/imperfection, scale effect parameter and excitation level.

© 2016 Jordan Journal of Mechanical and Industrial Engineering. All rights reserved

**Keywords:** Geometric nonlinearity, nonlocal elasticity, beam rise, scale parameter, resonance.

## 1. Introduction

Microelectromechanical systems and nanoelectromechanical systems have gained remarkable consideration due to their significant role in different engineering and modern technology fields, such as aerospace, communications, composites, electronics. These structures have more superior mechanical, electrical, and thermal properties as compared to other structures at the normal length scale. These properties make them ideal for the use in highly sensitive and high frequency devices for different applications [1].

In order to design a realistic model of a micro or a nanostructure and to well understand, optimize, and improve their performance, the small-scale effects and the atomic forces must be taken into consideration. In objects at the micro and nano scales, the dimensions, wavelengths, and sizes of these structures are no longer considered much larger than the characteristic dimensions of the microstructure. In these cases, the internal length scales of the material are comparable with the structure size. Moreover, the particles affect each other by long range cohesive forces in addition to the contact forces and heat diffusion. Consequently, the internal length scale should be considered as a material parameter, called nonlocal parameter, in the constitutive and governing equations and relations.

Although the experimental and atomistic simulations and models are both capable of showing the effects of the small-scale on the mechanical properties of the micro/nanostructures, these methods are expensive and restricted by computational capacity. It is well known that the local continuum theories for beams (Euler and Timoshenko) and plates (Kirchhoff and Mindlin) are scale free; therefore they are not able to capture the small scale effect on the mechanical, electrical, and thermal properties for very small beam and plate like structures. This makes them inadequate in describing the dynamical behavior for these structures [2]. In order to apply the continuum mechanics approach in the analysis of the micro and nanostructures, logical and reasonable modifications that take into consideration the scale effect, should be proposed. For this purpose, several theoretical models have been suggested. Among these, the strain gradient theory, the modified coupled stress theory, and the nonlocal elasticity theory which will be utilized in this article to analyze the free vibration problem of nonlocal annular and circular Mindlin plates.

The nonlocal elasticity theory was introduced by Eringen [3] accounts for the small-scale effects arising at the nanoscale level. He assumed that the stress at a point is a function of the strains at all points in the domain. Many researchers applied the nonlocal elasticity theory to study the free vibration, buckling, deflection, and dynamic problems of micro and nanostructures. For example, Reddy [4] obtained analytical solutions for the bending,

\* Corresponding author e-mail: maen.sari@ju.edu.jo.

buckling, and vibration problems for simply supported Euler, Timoshenko, Reddy, and Levinson beams using Eringen's nonlocal theory. Murmu and Adhikari [5] studied the nonlocal transverse in-phase and out-of-phase vibrations of double nanobeam systems, in which explicit closed form expressions for natural frequencies were derived. Shakouri *et al.* [6] applied the Galerkin approach to study the free vibration problem of nonlocal Kirchhoff plates with different boundary conditions. It was shown that the nonlocal parameter and Poisson's ratio have significant effects on the vibration. Wang *et al.* [2] applied the Hamilton's principle, Eringen's nonlocal elasticity theory, and Timoshenko beam theory to analyze the free vibration problem of micro/nanobeams. Their study concluded that the effects of small scale, rotary inertia, and transverse shear deformation are important on the vibration behavior of short and stubby micro/nanobeams.

Moreover, Murmu and Adhikari [7] applied the differential quadrature method and the nonlocal elasticity theory to study the free vibration of a rotating carbon nanotube modeled as an Euler-Bernoulli beam. It was shown that the vibration is significantly influenced by the angular velocity, preload, and the nonlocal parameter. Lu *et al.* [8] derived the dispersion relation for a harmonic flexural wave propagation in an Euler-Bernoulli beam, as well as the frequency equations and modal shape functions of the beam with different boundary conditions based on Eringen's nonlocal elasticity theory. Murmu and Pradhan [9] implemented the nonlocal elasticity theory to study the vibration response of single graphene sheets embedded in an elastic medium modeled as Winkler and Pasternak foundations. The differential quadrature method was employed in their analysis to solve the fundamental natural frequencies of plates with clamped and simply supported edges.

In a similar manner, Murmu and Pradhan [1] applied the nonlocal elasticity theory to investigate the free vibration problem of nanoplates under uniaxially prestressed conditions. In their study the differential quadrature method was utilized to obtain the fundamental natural frequencies for simply supported and clamped nanoplates. Moreover, it was observed that buckling occurs at a smaller critical compressive load compared to the classical plate theory. Gürses *et al.* [10] studied the free vibration analysis of thin nano-sized annular sector plates, where Eringen's nonlocal elasticity theory was utilized to formulate the equation of motion. Additionally, the discrete singular convolution method was applied after transforming the irregular physical domain into a rectangular domain by using geometric coordinate transformation. It was shown that the effects of the nonlocal parameter are significant in the vibration analysis. Hashemi *et al.* [11] applied an exact analytical approach along with Eringen's theory to study the free vibration problem of thick circular and annular functionally graded Mindlin nanoplates with different combinations of boundary conditions. The effects of the plate radius, material properties which vary through the material according to a power-law distribution, and the nonlocal parameter on the natural frequencies were examined. In another study, Hashemi *et al.* [12] introduced potential functions and used the separation of variables method to obtain closed form solutions for nonlocal rectangular

Mindlin plates with Levy-type boundary conditions. In their study, the effects of the nonlocal parameter, thickness to length ratio, and aspect ratio on the natural frequencies were investigated.

Ansari and Arash [13] applied the generalized differential quadrature method, Eringen's nonlocal elasticity theory, and the molecular dynamics simulations. Their purpose was to carry out the vibration analysis of single layered graphene sheets modeled as rectangular Mindlin plates, and to evaluate the appropriate values of the nonlocal parameter appropriate to each boundary condition. Duan and Wang [14] obtained exact solutions for the axisymmetric bending of micro and nano circular plates under general loading using a nonlocal plate theory. It was concluded that nonlocal parameter has a significant effect on the deflections, moments, and bending stiffness.

As stated by Ansari *et al.* [15], structures at the micro and nano scales are capable of undergoing large deformations within the elastic limit, which makes the nonlinear analysis obviously important. In their study, the homotopy perturbation method was applied to study the nonlinear vibrations of multiwalled carbon nanotubes embedded in an elastic medium. They showed that changing the material of the elastic medium has an influence on the vibration characteristics.

Fu *et al.* [16] investigated the nonlinear free vibration of embedded multiwalled carbon tubes using the incremental harmonic balanced method. It was shown that the surrounding elastic medium, van der Waals forces and aspect ratio of the multi-wall nanotubes have significant effects on the amplitude frequency response curves. It was noticed that in [15] and [16] the small scale effects were not taken into consideration; therefore, Ansari *et al.* [17] developed a nonlocal elastic beam model and adopted the incremental harmonic balance method to investigate the effects of the length scale, geometrical parameters, temperature rise and the elastic medium on the nonlinear frequency and displacement of embedded multiwalled carbon nanotubes. On the other hand, during the fabrication, manufacturing, assembling, and handling of such mechanical parts, structures with an initial deflection (slack) may be produced. As a result, this deflection will have an influence on the dynamics, vibration, and stability characteristics of the structure.

Al-Qaisia and Hamdan [18] presented an analytical study of nonlinear frequency veering of an elastic Euler-Bernoulli, hinged-hinged with one torsional spring at one end, resting on a Winkler elastic foundation and subjected to a static lateral load with an initial 1/4 sine shape rise due a constant differential edge settlement. A combined numerical-analytical procedure which accounts for the nonlinear interdependence between the lateral deflection and induced axial force due to mid-plane stretching was used to determine the beam static deflection. The assumed single mode approach was used to obtain the nonlinear temporal equation which contains quadratic and cubic nonlinear terms. The harmonic balance method was used to solve the nonlinear free vibration frequency about the static equilibrium deflection. The results of simulation indicate that the vibration amplitude, depending on location of the veering point, has a significant effect on the frequency loci behavior. Also, they extended these analyses to primary resonance response and its stability

under vertical uniformly distributed excitation comprised of a large static part and a harmonically time varying part [19]. The obtained results indicate that the coefficients of the quadratic and cubic nonlinear terms, can vary widely depending on system parameters, and in particular, these coefficients can take positive and negative values, which affect the number of equilibrium positions, while the behavior of the system whether it is of hardening or softening type.

Lacarbonara *et al.* [20] studied the nonlinear response and stability of a hinged–hinged uniform moderately curved beam with a torsional spring at one end. It was shown that varying the initial rise of the beam has an effect on the one-to one auto parametric resonance and on the experienced Hopf and homoclinic bifurcations. Additionally, Ouakad and Younis [21] used a 2D nonlinear curved beam model which was derived by applying a multimode Galerkin approach to study the coupled in-plane and out-of-plane displacements of a carbon nano tube with curvature. They showed that the natural frequencies, mode shapes, mode crossings and mode veering are affected by the variation of the level of slackness and the DC load.

Mayoof and Hawwa [22] studied the nonlinear vibration of a clamped-clamped single wall carbon nanotube with waviness (deflection). The elastic continuum mechanics theory, along with Hamilton's principle, was applied to formulate the problem and derive the equation of motion which involved quadratic and cubic nonlinearities. The dynamics response of the system was investigated, and phase portrait, Poincaré section, and time history diagrams were generated. The results revealed that the nanotube underwent period-doubling bifurcations that were turned into chaos.

Garcia-Sanchez *et al.* [23] detected the bending-mode vibrations of multi and single-wall carbon nanotubes using a scanning force microscopy method. For multiwalled nanotubes, it was found that the resonance frequency is consistent with the elastic beam theory, whereas it is significantly reduced for single-wall nanotubes due to slack generated from fabrication processes. Üstünel *et al.* [24] studied the vibrations of nanotubes modeled as clamped-clamped suspended one-dimensional elastic systems with a slack and downward external forces; it was found that the frequencies are highly affected by the slack.

Al-Qaisia and Hamdan [25], extended the two previous studies [18, 19] on frequency veering by studying the effect of an initial geometric imperfection wavelength, amplitude and degree of localization on the in-plane nonlinear natural frequencies veering and mode localization of an elastic Euler-Bernoulli beam resting on a Winkler elastic foundation. Results were presented for the nonlinear natural frequencies of the first three modes of vibration, for a selected range of physical parameters like; torsional spring constant, elastic foundation stiffness and amplitude and wavelength of a localized and non-localized initial slack.

The present work extends the previous studies in [18, 19 and 25] on beam like-structures with initial imperfections to include the small scale effect on the primary and sub harmonic responses, using the nonlocal elasticity theory to derive the mathematical model.

The present study is organized as follows: First, the governing partial differential equation for the local beam is presented. Then, by applying Eringen's nonlocal theory, the partial equation of motion for the nonlocal beam is derived. Furthermore, the Galerkin method is applied to obtain the reduced order model, using the multi-mode approach. The method of multiple scales is utilized to determine the nonlinear natural frequencies and the frequency response curves for the primary resonance at selected values of parameters for simply supported beams.

## Problem Formulation

### Mathematical Model

The governing nonlinear equation of motion of moderately large amplitude vibration of an Euler-Bernoulli beam with initial deflection, and subjected to a harmonic force is given by:

$$m\hat{w} + EI\hat{w}^{iv} + \hat{c}\hat{w} - \frac{EA}{L}(\hat{w}_0'' + \hat{w}''') \int_0^L \left( \frac{1}{2} \hat{w}'^2 + \hat{w}_0' \hat{w}' \right) d\hat{x} = F_0 \cos(\hat{\Omega}\hat{t}) \quad (1)$$

where  $\hat{w}$  is the transverse deflection,  $\hat{w}_0$  initial deflection “initial rise”,  $l$  is the beam length,  $A$  and  $I$  are beam's area and principal moment of inertia of the cross section  $I$  respectively,  $m$  is the mass per unit length,  $E$  is the Young's modulus of Elasticity,  $F_0$  is the excitation level,  $\hat{c}$  is the coefficient of damping,  $\hat{t}$  is the time, and  $\hat{\Omega}$  is the frequency of excitation. The prime denotes the derivative with respect to the spatial coordinate  $\hat{x}$ , while the dot denotes the derivative with respect to time  $\hat{t}$ .

The bending moment  $M(\hat{x}, \hat{t})$  is given as

$$M(\hat{x}, \hat{t}) = -EI \hat{w}''(\hat{x}, \hat{t}) \quad (2)$$

In light of Eq. (2),  $M''(\hat{x}, \hat{t})$  is given by

$$M''(\hat{x}, \hat{t}) = m \hat{w}''(\hat{x}, \hat{t}) + \hat{c} \hat{w}''(\hat{x}, \hat{t}) - \frac{EA}{L} (\hat{w}_0''(\hat{x}) + \hat{w}''(\hat{x}, \hat{t})) \int_0^L \left( \frac{1}{2} \hat{w}'^2(\hat{x}, \hat{t}) + \hat{w}_0'(\hat{x}) \hat{w}'(\hat{x}, \hat{t}) \right) d\hat{x} - F_0 \cos(\hat{\Omega}\hat{t}) \quad (3)$$

### Nonlocal Theory

In local elasticity theory, the stress at a reference point in a body depends on the strain at the same point. On the other hand, In the nonlocal elasticity theory pioneered by Eringen, the stress at a point in a linear, homogeneous,

isotropic, and elastic domain is related to the stress field at all points in the domain. Eringen's theory is based on the atomic theory of lattice dynamics and experimental results on phonon scattering and dispersion [3, 10].

For nonlocal linear elastic solids, the stress tensor  $t_{ij}$  is defined as:

$$t_{ij} = \int \alpha(|x' - x|) \sigma_{ij}(x') dV(x') \quad (4)$$

where  $x$  is a reference point in the elastic domain,  $\alpha(|x' - x|)$  is the non-local kernel attenuation function. It introduces the nonlocal effects at the reference point  $x$  produced by the local stress  $\sigma_{ij}$  at any point  $x'$ , and  $|x' - x|$  is the distance in Euclidean form.

Eringen introduced a linear differential operator  $\zeta$ , defined by  $\zeta = 1 - (e_0 l)^2 \nabla^2$ , in which  $e_0$  is a material constant estimated by experiments or other models and theories [3]. The nonlocal theory relations could result in approximate solutions to those obtained by atomic theory. The value of  $e_0$  was taken to be 0.39 in Eringen's analysis. Moreover, the constant  $l$  represents the internal characteristic length which is of the same order of the external length.

According to Eringen's theory, the integral constitutive relation of Eq. (4) could be simplified and have the following form:

$$\left(1 - (e_0 l)^2 \nabla^2\right) t_{ij} = \sigma_{ij} \quad (5)$$

Due to its simple form, Eq. (5) has been extensively employed by many researchers in applying the nonlocal theory to study and analyze the vibration and mechanics of micro and nanostructures. According to Eringen's nonlocal elasticity theory, the stresses at a point in the body not only depend on the strain at that point, but also on the strains at all other points of the body [3]. Thus, the nonlocal constitutive relation for the moment is given as:

$$M(\hat{x}, \hat{t}) - (e_0 a)^2 M''(\hat{x}, \hat{t}) = -EI \hat{w}''(\hat{x}, \hat{t}) \quad (6)$$

where  $a$  is an internal characteristic length (e.g. lattice parameter, granular distance, and distance between C-C bonds) [24].

Inserting Eq. (3) into Eq. (6), we obtain:

$$M(\hat{x}, \hat{t}) = (e_0 a)^2 \left[ \int_0^L \left( \frac{1}{2} \hat{w}'^2 + \hat{w}'_0 \hat{w}' \right) d\hat{x} - F_0 \cos(\hat{\Omega} \hat{t}) \right] - EI \hat{w}'' \quad (7)$$

Substituting Eq. (7) into Eq. (6), the equation of the transverse motion of the nonlocal Euler- Bernoulli beam with initial deflection can be written as:

$$\begin{aligned} & m\hat{w} - (e_0 a)^2 m\hat{w}'' + EI\hat{w}^{iv} + \hat{c}\hat{w} - (e_0 a)^2 \hat{c}\hat{w}'' \\ & - \frac{EA}{L} (\hat{w}_0'' + \hat{w}'') \int_0^L \left( \frac{1}{2} \hat{w}'^2 + \hat{w}'_0 \hat{w}' \right) d\hat{x} \\ & + (e_0 a)^2 \frac{EA}{L} (\hat{w}_0^{iv} + \hat{w}^{iv}) \int_0^L \left( \frac{1}{2} \hat{w}'^2 + \hat{w}'_0 \hat{w}' \right) d\hat{x} \\ & = F_0 \cos(\hat{\Omega} \hat{t}) - (e_0 a)^2 (F_0 \cos(\hat{\Omega} \hat{t}))'' \end{aligned} \quad (8)$$

To simplify Eq. (8), the following non-dimensional variables and parameters with respect to the cross sectional area radius of gyration  $r = \sqrt{I/A}$ , are introduced:

$$\begin{aligned} x &= \frac{\hat{x}}{l}, & w &= \frac{\hat{w}}{r}, & w_0 &= \frac{\hat{w}_0}{r}, \\ t &= \hat{t} \sqrt{\frac{EI}{ml^4}}, & \Omega &= \hat{\Omega} \sqrt{\frac{ml^4}{EI}}, \\ c &= \frac{\hat{c}l^2}{\sqrt{mEI}}, & F &= \frac{F_0 l^4}{rEI}, \\ \text{and } \mu^2 &= \frac{(e_0 \hat{a})^2}{l^2} \end{aligned}$$

After substituting the above parameters, Eq. (1) in its simplest form is given as:

$$\begin{aligned} & \frac{\partial^2 w}{\partial t^2} - \mu^2 \frac{\partial^4 w}{\partial x^2 \partial t^2} + \frac{\partial^4 w}{\partial x^4} + c \frac{\partial w}{\partial t} - c\mu^2 \frac{\partial^3 w}{\partial x^2 \partial t} \\ & - \left( \frac{\partial^2 w}{\partial x^2} + \frac{\partial^2 w_0}{\partial x^2} \right) \int_0^1 \left( \frac{1}{2} \left( \frac{\partial w}{\partial x} \right)^2 + \frac{\partial w}{\partial x} \frac{\partial w_0}{\partial x} \right) dx \\ & + \mu^2 \left( \frac{\partial^4 w}{\partial x^4} + \frac{\partial^4 w_0}{\partial x^4} \right) \\ & \int_0^1 \left( \frac{1}{2} \left( \frac{\partial w}{\partial x} \right)^2 + \frac{\partial w}{\partial x} \frac{\partial w_0}{\partial x} \right) dx = F \cos(\Omega t) \end{aligned} \quad (9)$$

The nonlinear integral-partial differential equation (9) can be discretized using the Galerkin's approach by assuming [26,27]:

$$w(x, t) = \sum_{n=1}^N \phi_n(x) q_n(t) \quad (10)$$

where  $N$  is the number of retained modes,  $\phi_n(x)$  are the mode shapes of the linear, undamped, and unforced beam, and  $q_n(t)$  are the generalized coordinates. Substituting Eq. (10) into Eq. (9), multiplying by  $\phi_n(x)$  and integrating over the beam's span, yields the set of the nonlinear ordinary equations:

$$\begin{aligned} & \ddot{q}_m + \omega_m^2 q_m = -c\dot{q}_m + A_{mij} q_i q_j + \\ & B_{mijk} q_i q_j q_k + p_m \cos(\Omega t) \end{aligned}, \quad (11)$$

m=1, 2, ..., N

where:

$$A_{mij} = \frac{1}{\int_0^1 \phi_m^2 dx - \mu^2 \int_0^1 \phi_m'' \phi_m dx} \left( \left( \int_0^1 \phi_i'' \phi_m dx \left( \int_0^1 \phi_j' w_0' dx \right) \right) + \left( \int_0^1 \phi_i' \phi_j' dx \left( \frac{1}{2} \int_0^1 w_0'' \phi_m dx \right) \right) \right) - \left( \mu^2 \int_0^1 \phi_i^{iv} \phi_m dx \left( \int_0^1 \phi_j' w_0' dx \right) \right) - \left( \mu^2 \int_0^1 \phi_i' \phi_j' dx \left( \frac{1}{2} \int_0^1 w_0^{iv} \phi_m dx \right) \right) \right) \quad (12)$$

$$B_{mijk} = \frac{1}{\int_0^1 \phi_m^2 dx - \mu^2 \int_0^1 \phi_m'' \phi_m dx} \left( \left( \int_0^1 \phi_i'' \phi_m dx \left( \int_0^1 \frac{1}{2} \phi_j' \phi_k' dx \right) \right) - \left( \mu^2 \int_0^1 \phi_i^{iv} \phi_m dx \left( \int_0^1 \frac{1}{2} \phi_j' \phi_k' dx \right) \right) \right) \right) \quad (13)$$

$$\omega_m^2 = \frac{1}{\int_0^1 \phi_m^2 dx - \mu^2 \int_0^1 \phi_m'' \phi_m dx} \left( \int_0^1 \phi_m^{iv} \phi_m dx - \left( \left( \int_0^1 w_0'' \phi_m dx \right) + \mu^2 \left( \int_0^1 w_0^{iv} \phi_m dx \right) \right) \left( \int_0^1 w_0' \phi_m' dx \right) \right) \quad (14)$$

$$f_m = F \int_0^1 \phi_m dx$$

$$p_m = \frac{f_m}{\int_0^1 \phi_m^2 dx - \mu^2 \int_0^1 \phi_m'' \phi_m dx} \quad (15)$$

where  $f_m$  is the projection of the force  $F$  onto the  $m^{th}$  mode.

The initial deflection for the simply supported beam is given as:

$$w_0(x, t) = q_0 \sin(\pi x) \quad (16)$$

It is worth mentioning that the initial deflection has a value of  $q_0$  at the midsection of the beam, rather than it satisfies the boundary conditions.

The mode shapes for a simply supported beam are given as:

$$\phi_n(x) = \sin(n\pi x) \quad (17)$$

The boundary conditions for the simply supported beam are given as:

$$w(0, t) = \frac{\partial^2 w(0, t)}{\partial x^2} = w(L, t)$$

$$= \frac{\partial^2 w(L, t)}{\partial x^2} = 0 \quad (18)$$

The boundary conditions for the non-local and local (classical) beams are the same when both ends of the beam are fixed as the scale effect gets nullified. In the present study, the dynamic behavior of beams under consideration will be analyzed for primary resonance using the first five modes.

### Perturbation Analysis

#### Free Vibrations

In the present study, the non-dimensional nonlinear natural frequencies of the nonlinear beam given in Eq. (4) can be obtained by using the Method of Multiple Scales (MMS). The second order approximation of the free undamped nonlinear natural frequency  $\omega_{NL}$  is expressed as a function of the vibration amplitude  $a$  and the parameters of the nonlocal simply supported beams, and given by the expression:

$$\omega_{NL} = \omega_n \left( 1 + \frac{\alpha_{eff}}{\omega_n} a^2 \right) \quad (19)$$

where  $\alpha_{eff}$  is the effective nonlinearity to be defined later, and  $a$  is the amplitude (the initial condition for the displacement) of the beam.

#### Primary Resonance

In case the beam is subjected to primary resonance of the  $n^{th}$  mode, we assume that the contribution of the  $n^{th}$  mode is of lower order than the contributions of other modes. Therefore, we assume  $q_n(t)$  and  $q_m(t)$  to be in the form of [28]:

$$q_n(T_0, T_2, \epsilon) = \epsilon q_{n1} + \epsilon^2 q_{n2} + \epsilon^3 q_{n3}$$

$$q_m(T_0, T_2, \epsilon) = \epsilon^2 q_{m2} + \epsilon^3 q_{m3}, \quad m \neq n \quad (20)$$

where in these equations,  $\epsilon$  is considered as a small and dimensionless parameter, and the two time scales  $T_0$  and  $T_2$  are introduced as  $T_0 = \epsilon^0 t$  and  $T_2 = \epsilon^2 t$ . In order to apply the multiple scales method, the effects of the damping and the excitation terms are scaled to balance the effect of the nonlinearity. Hence,  $c$  and  $p_n$  are scaled as  $\epsilon^2 c$  and  $\epsilon^3 p_n$ . Applying the method of multiple scales yields the *frequency-response curve* as:

$$\sigma = \alpha_{eff} a_n^2 \pm \sqrt{\frac{P_n^2}{4\omega_n^2 a_n^2} - \frac{c^2}{4}} \quad (21)$$

where  $\sigma$  is a detuning parameter introduced such that

$$\Omega = \omega_n + \varepsilon^2 \sigma \quad (22)$$

and  $\alpha_{eff}$  is the effective nonlinearity given by:

$$\alpha_{eff} = -\frac{1}{8\omega_n} \left( \sum_{j=1}^N A_{jnn} (A_{nnj} + A_{njn}) \left( \frac{2}{\omega_j^2} + \frac{1}{\omega_j^2 - 4\omega_n^2} \right) + 3B_{nnnn} \right)$$

Eq. (22) shows the nearness of the excitation frequency to the  $n$ th natural frequency,

Eq. (23) is substituted into Eq. (19) to obtain the nonlinear natural frequencies [28].

In this section, the excitation frequency  $\Omega$  is very close to the  $n$ th linear frequency  $\omega_n$ . Hence, other modes not being directly or indirectly excited will decay to zero with time due to the presence of damping.

The details of the MMS are omitted for brevity, and interested readers can refer to Emam's thesis [28].

## Results and Discussion

The multi-mode approach (assumed mode method) is applied in the present article, where five modes were retained to obtain the reduced order model. In this section, dynamic behavior and the characteristics of the nonlocal beams considered herein were analyzed by examining the effective nonlinearity of the simply supported beam given in Eq. (23). The value of  $\alpha_{eff}$  as a function of the beam rise  $q_0$  and the scale parameter  $\mu$  was calculated and presented in 3-D surface plots as shown in Figures (1-2). These Figures show that the value of  $\alpha_{eff}$  may increase or decrease depending on the combination of the parameters  $q_0$  and  $\mu$ . It is known that the behavior of the nonlinear beam is either of hardening (the frequency increases with the amplitude) or softening type (the frequency decreases with the amplitude), depending on the value of the parameter  $\alpha_{eff}$ . It is known that for  $\alpha_{eff} > 0$ , the nonlinear beam given in Eq. (11) exhibits a hardening type behavior and a softening type otherwise. Moreover, when the value of  $\alpha_{eff} = 0$ , the effects of the quadratic and cubic nonlinearities cancel each other and consequently the response resonance curve resembles that of the corresponding linear beam, which implies that the frequency of the beam does not depend on the amplitude.

The variation of the fundamental nonlinear frequency with the amplitude of the first mode of a simply supported SS beam with  $q_0 = 0.2$  at different values of the dimensionless nonlocal parameter  $\mu$  is presented in Figure 2. It is observed that the nonlinear frequency decreases by increasing the nonlocal parameter due to the decrease in the stiffness of the beam. In Eringen nonlocal elasticity

theory, it may be viewed that atoms are bonded by elastic springs with finite value, while the classical local model assumes that the stiffness of springs have a value of infinity [2, 10]. Further, as  $\alpha_{eff} > 0$  at  $q_0 = 0.2$ , the frequency increases by increasing the vibration amplitude. Thus, the behavior of the SS beam is of hardening type regardless the value of scale factor  $\mu$ .

The variation of the fundamental nonlinear frequency with the amplitude of the first mode of the SS beam with  $\mu = 0.4$  at different values of the beam rise parameter  $q_0$  is presented in Figure 3. The Figure reveals that the behavior of the beam switches from hardening to softening as the value of the beam rise  $q_0$  increases. It is worthwhile to mention that at a value of the initial rise between 0.4 and 0.6, the frequency is constant and independent of the amplitude (initial conditions). In this case, the beam exhibits a linear behavior. As the beam rise is further increased, the beam has a softening effect as  $\alpha_{eff} < 0$ . It can be seen that at a given value of the scale effect, the beam may have hardening, softening, or linear behavior depending on the value of the initial rise  $q_0$ . This observation may be useful in the design and analysis of industrial applications in which the dynamics of the micro/ nano beams are main part of them.

The frequency response of the primary resonance of the nonlinear system given in Eq. (27), describing the forced vibration of the beam systems, were analyzed and presented for selected values of the beam rise  $q_0$  and the scale parameter  $\mu$ . In Figure 4, the frequency response curves are generated for the simply supported beam with  $c = 0.05$ ,  $f = 0.5$ , and  $q_0 = 0.1$  at different values of the scale parameter  $\mu$ . It is observed that as the scale parameter  $\mu$  increases, the beam's behavior is switched from hardening to softening type. It is clear that the curves are bent to the right (hardening behavior); whereas at  $\mu = 0.8$ , the curve is bent to the left (softening behavior), and the hardening non-linearity at  $\mu = 0.1$  is stronger than that at  $\mu = 0.5$ . Furthermore, as the scale parameter  $\mu$  increases, the steady state amplitude of the first mode of the beam decreases.

In a similar manner, the frequency response curves of primary resonance are generated and presented in Figures 5 and 6 for the simply supported beam at  $c = 0.05$ ,  $f = 0.5$ , and  $\mu = 0.2$  at different values of the beam rise  $q_0$ . It is shown that the beam exhibits the hardening and softening type as the value of  $q_0$  is increased. From Figure 5, it is observed that if the beam exhibits a hardening type, the steady state amplitude of the first mode of the beam increases when the initial rise  $q_0$  increases. On the other hand, Figure 6 shows that if the beam exhibits a softening type, the steady state amplitude of the first mode of the beam decreases when the initial rise  $q_0$  increases. In these curves, the stable and unstable branches can be observed in addition to the jump phenomenon.

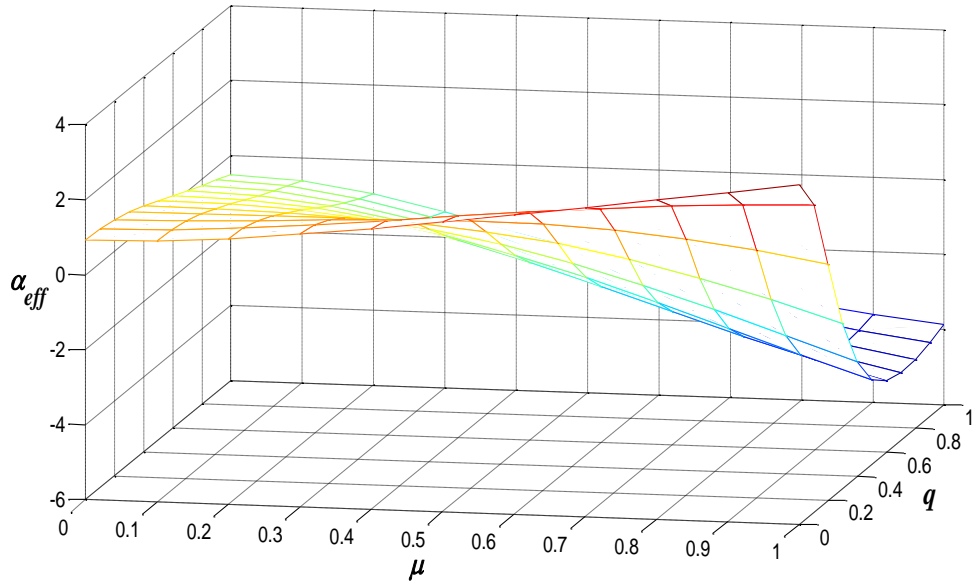


Figure 1: the parameter  $\alpha_{eff}$  of the SS beam versus rise  $q$  and scale  $\mu$

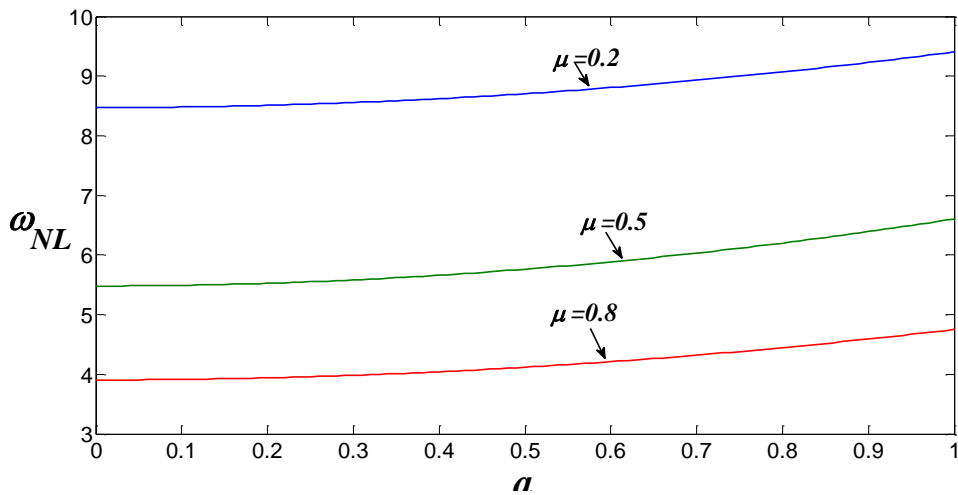


Figure 2: Variation of the fundamental nonlinear frequency of a simply supported beam with amplitude for  $q = 0.2$

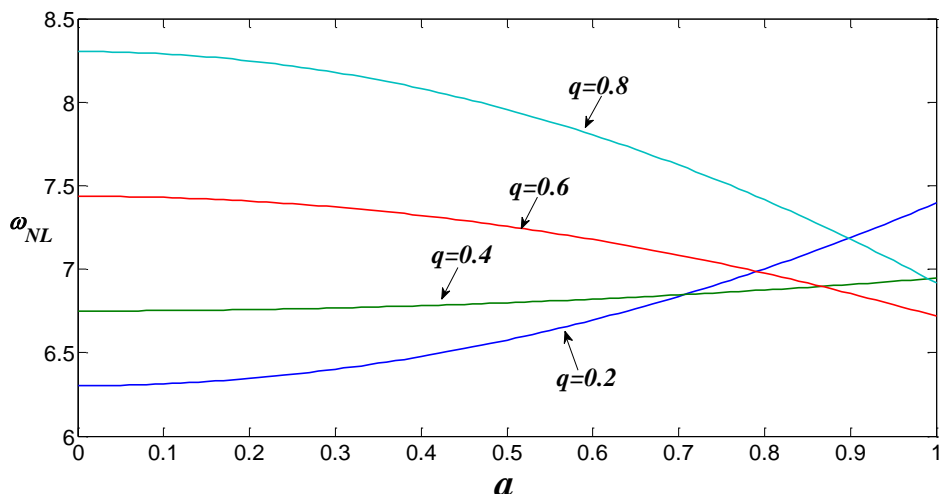
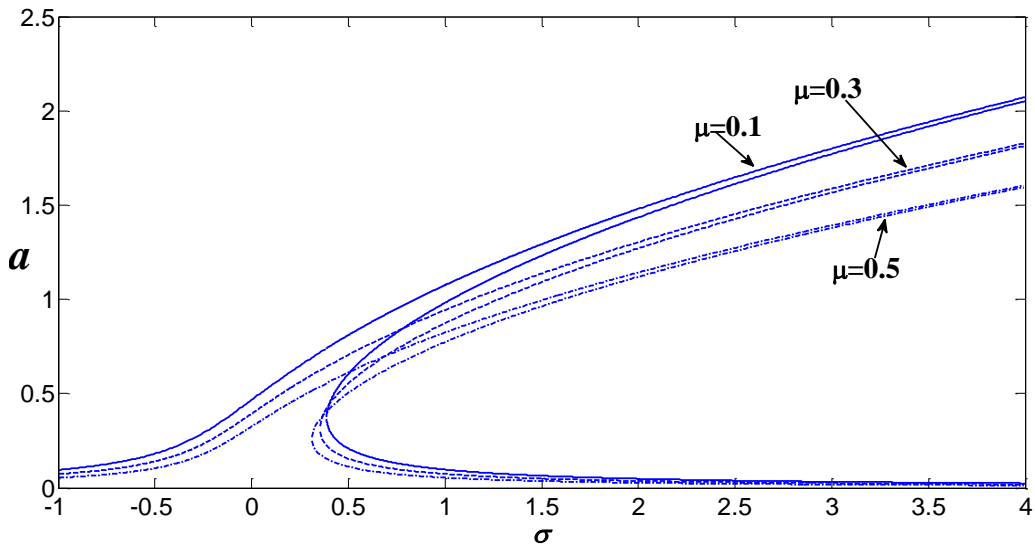
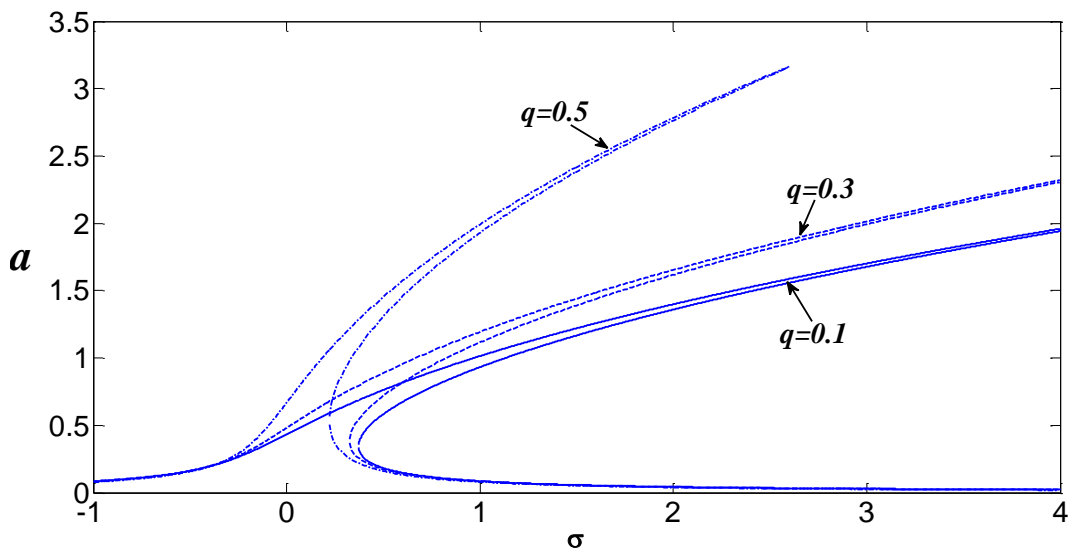


Figure 3: Variation of the fundamental nonlinear frequency of a simply supported beam with amplitude for  $\mu = 0.4$



**Figure 4:** Frequency-response curves in the case of primary resonance of a simply supported beam for  $c = 0.05, f = 0.5, q_0 = 0.1$



**Figure 5:** Frequency-response curves in the case of primary resonance of a simply supported beam for  $c = 0.05, f = 0.5, \mu = 0.2$

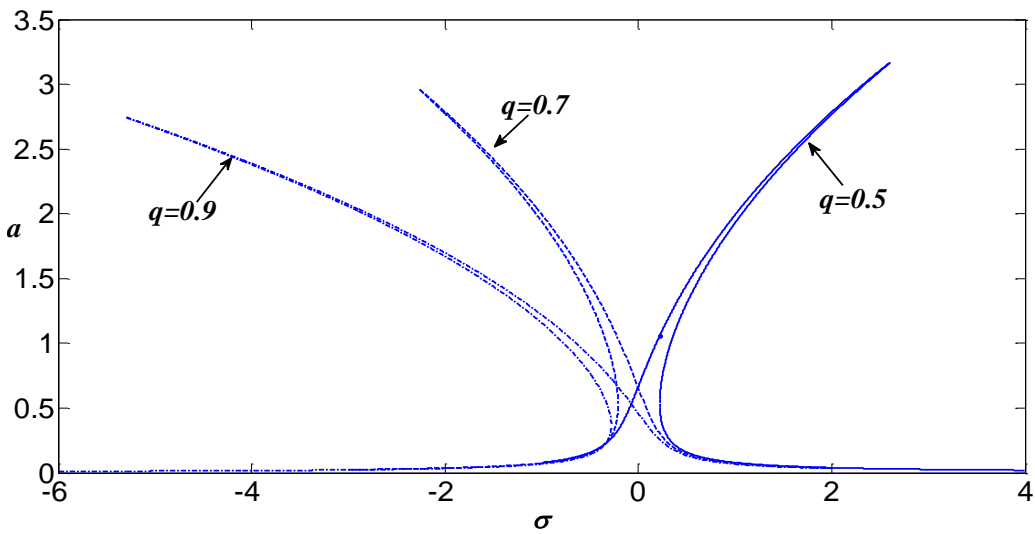


**Figure 6:** Frequency-response curves in the case of primary resonance of a simply supported beam for  $c = 0.05, f = 0.5, \mu = 0.2$

## Conclusions

The primary resonance of a simply supported Euler beam with initial deflection was investigated. Eringen's nonlocal elasticity theory was utilized and the Galerkin approach was applied to convert the partial differential governing equation into a set of nonlinear ordinary differential equations. The method of multiple scales was carried out to determine the frequency response curves of the beam under consideration. It was shown that the scale parameter, beam's initial deflection, and excitation level have significant influence on the behavior of the beam. For the selected values of the scale parameter and the beam rise, it was shown that the simply supported beam switches its behavior from hardening to softening type.

For future work, it is recommended to consider other effects that may influence the behavior of micro and nano dynamical systems, such as temperature changes, electro and magnetic fields effects. Furthermore, analyzing such systems subjected to simultaneous resonances may be of high interest since these systems may exhibit mixed hardening and softening behavior.

## Acknowledgment

Prof. A. AL-Qaisia acknowledges the support of the Deanship of Academic Research at The University of Jordan.

## References

- [1] T. Murmu and S. C. Pradhan, "Vibration analysis of nanoplates under uniaxial prestressed conditions via nonlocal elasticity". *Journal of Applied Physics*, Vol. 106, 2009, 104301.
- [2] C.M. Wang, Y. Y. Zhang, X Q He, "Vibration of nonlocal Timoshenko beams". *Nanotechnology*, Vol. 18, 2007, 105401.
- [3] A.C. Eringen, "On differential equations of nonlocal elasticity and solutions of screw dislocation and surface waves". *Journal of Applied Physics*, Vol. 54, 1983, 4703-4710.
- [4] J.N. Reddy, "Nonlocal theories for bending, buckling and vibration of beams". *International Journal of Engineering Sciences*, Vol. 45, 2007, 288-307.
- [5] T. Murmu, S. Adhikari, "Nonlocal transverse vibration of double-nanobeam systems". *Journal of Applied Physics*, Vol. 108, 2010, 083514.
- [6] Shakouri, T.Y. Ng, R.M. Lin, "Nonlocal plate model for the free vibration analysis of nanoplates with different boundary conditions". *Journal of computational and theoretical nanoscience*, Vol. 8, 2011, 2118-2128.
- [7] T. Murmu, S. Adhikari, "Scale-dependent vibration analysis of prestressed carbon nanotubes undergoing rotation". *Journal of Applied Physics*, Vol. 108, 2010, 123507.
- [8] P. Lu, H. P. Lee, C. Lu, P. Q. Zhang, "Dynamic properties of flexural beams using a nonlocal elasticity model". *Journal of Applied Physics*, Vol. 99, 2006, 073510.
- [9] T. Murmu, S. C. Pradhan, "Vibration analysis of nano-single-layered graphene sheets embedded in elastic medium based on nonlocal elasticity theory". *Journal of Applied Physics*, Vol. 105, 2009, 064319.
- [10] M. Gürses, B. Akgöz, Ö. Civalek, "Mathematical modeling of vibration problem of nano-sized annular sector plates using the nonlocal continuum theory via eight-node discrete singular convolution transformation". *Applied Mathematics and Computation*, Vol. 219, 2012, 3226-3240.
- [11] S.H. Hashemi, M. Bedroud, R. Nazemnezhad, "An exact analytical solution for free vibration of functionally graded circular/annular Mindlin nanoplates via nonlocal elasticity". *Composite Structures*, Vol. 103, 2013, 108-118.
- [12] S.H. Hashemi, M. Zare, R. Nazemnezhad, "An exact analytical approach for free vibration of Mindlin rectangular nano-plates via nonlocal elasticity". *Composite Structures*, Vol. 100, 2013, 290-299.
- [13] R. Ansari, S. Sahmani, B. Arash, "Nonlocal plate model for free vibrations of single-layered graphene sheets". *Physics Letters A*, Vol. 375, 2010, 53-62.
- [14] W. H. Duan, C.M. Wang, "Exact solutions for axisymmetric bending of micro/nanoscale circular plates based on nonlocal plate theory". *Nanotechnology*, Vol. 18, 2007, 385704.
- [15] R. Ansari, M. Hemmatnezhad, H. Ramezannezhad, "Application of HPM to the nonlinear vibrations of multiwalled carbon nanotubes". *Numerical methods for partial differential equations*, Vol. 26, No. 9, 2010, 490-500.
- [16] Y.M. Fu, J.W. Hong, X.Q. Wang, "Analysis of nonlinear vibration for embedded carbon nanotubes". *Journal of Sound and Vibration*, Vol. 296, 2006, 746-756.
- [17] R. Ansari, H. Ramezannezhad, R. Gholami, "Nonlocal beam theory for nonlinear vibrations of embedded multiwalled carbon nanotubes in thermal environment". *Nonlinear Dynamics*, Vol. 67, 2012, 2241-2254.
- [18] A. Al-Qaisia, M. N. Hamdan, "Non-Linear Frequency Veering in a Beam Resting on Elastic Foundation". *Journal of Vibration and Control*, Vol. 15, No. 11, 2009, 1627-1647.
- [19] A. AL-Qaisia, M. N. Hamdan, "Primary Resonance Response of a Beam with a Differential Edge Settlement Attached to an Elastic Foundation". *Journal of Vibration and Control*, Vol. 16, No. 6, 2010, 853-877.
- [20] W. Lacarbonara, H. Arafat, A.H. Nayfeh, "Large non-linear interactions in imperfect beams at veering". *International Journal of Non-Linear mechanics*, Vol. 40, No. 7, 2005, 987-1003.
- [21] H. M. Ouakad, M. I. Younis, "Natural frequencies and mode shapes of initially curved carbon nanotube resonators under electric excitation". *Journal of Sound and Vibration*, Vol. 330, 2011, 3182-3195.
- [22] F.N. Mayoof, M.A.Hawwa, "Chaotic behavior of a curved carbon nano tube under harmonic excitation". *Journal of Chaos, Solitons and Fractals*, Vol. 42, 2009, 1860-1867.
- [23] D. Garcia-Sanchez, A. San Paulo, M.J. Esplandiú, F. Perez-Murano, L. Forro, A. Aguiasca, A. Bachtold, "Mechanical detection of carbon nanotube resonator vibrations". *Physical Review Letters*, Vol. 99, 2007, 1-4.
- [24] H. Üstünel, D. Roundy, "T.A. Arias, Modeling a suspended nanotube oscillator". *Nano Letters*, Vol. 5, 2005, 523-526.
- [25] A. Al-Qaisia, M. N. Hamdan, "On Nonlinear Frequency Veering and Mode Localization of a Beam with Geometric Imperfection Resting on Elastic Foundation". *Journal of Sound and Vibration*, Vol. 332, No. 15, 2013, 4641-4655.
- [26] M. Abu-Alshaikh, A. N. Al-Rabadi, H.S. Alkhalidi, "Dynamic Response of Beam with Multi-Attached Oscillators and Moving Mass, Fractional Calculus Approach". *Jordan Journal of Mechanical and Industrial Engineering*, Vol. 8, No. 5, 2014, 275-288.
- [27] M. Ghadiri, K. Malekzadeh, F.A. Ghasemi, "Free Vibration of an Axially Preloaded Laminated Composite Beam Carrying a Spring-Mass-Damper System with a Non-Ideal Support". *Jordan Journal of Mechanical and Industrial Engineering*, Vol. 9, No. 3, 2015, 195-207.
- [28] S. Emam, A Theoretical and Experimental Study of Nonlinear Dynamics of Buckled Beams. Ph.D. Dissertation, Department of Engineering Science and Mechanics, Virginia Polytechnic Institute and State University, Blacksburg, 2002.



# Parallel Translating Mechanism Process-Oriented Mathematical Model and 3-D Model for Cylindrical Gears with Curvilinear Shaped Teeth

CHANG Qinglin, HOU Li \*

*School of Manufacturing Science and Engineering, Sichuan University, No.24 South Section 1, Yihuan Road, Chengdu 610065, China.*

*Received Received Oct., 5, 2015*

*Accepted March, 15, 2016*

## Abstract

For the main purpose of studying the tooth surface equation and undercutting conditions of the cylindrical gears with curvilinear shaped teeth processed by parallel translating mechanism, the tooth surface equation and meshing condition of the cylindrical gears with curvilinear shaped teeth processed by parallel translating mechanism were deduced by the method of differential geometry and coordinate transformation, based on considering cutting tool shape and installation position error. The undercutting line of the cylindrical gears with curvilinear shaped teeth processed by parallel translating mechanism was also calculated. The manufacturing process of the parallel translating mechanism was simulated in three-dimensional software and then the three dimensional solid model of cylindrical gears with curvilinear shaped teeth was obtained. The studies referred to in the present paper have a certain reference value for research, development and design of the cylindrical gears with curvilinear shaped teeth processed by parallel translating mechanism.

© 2016 Jordan Journal of Mechanical and Industrial Engineering. All rights reserved

**Keywords:** *Cylindrical gears with curvilinear shaped teeth; Tooth surface equation; Undercutting; Envelope; Translational Processing Device..*

## 1. Introduction

Gear is the most important and the most commonly key parts used in industrial production. With the development of productivity, the development of high speed, overloading and compact structure gear pair has a strong demand. The improvement of the gear has two aspects: tooth profile curve and tooth line curve.

For the study of tooth line curve, a lot of valuable studies have been done by the scholars. From the study, the advantages of longer contact line, tooth line symmetry, transmission more stable, higher bearing capacity, good lubrication performance and none axial force in cylindrical gears with curvilinear shaped teeth have been found [1-7]. The two common methods used in the processing of cylindrical gears with curvilinear shaped teeth are the method of rotating knife dish and the method of parallel translating mechanism. The tooth surface equation and characteristics are different by the different method. Di Yutao and professor Chen Ming [1, 2] analyzed the forming principle, meshing performance and bearing capacity of the cylindrical gears with curvilinear shaped teeth processed by the rotating knife dish. Wang Shaojiang and Xiao Huajun [3-6] studied the tooth surface equation, machining process of cylindrical gears with curvilinear shaped teeth processed by the rotating knife dish by the computer simulation. Tseng and his partner [7-9]

established the mathematic model of cylindrical gears with curvilinear shaped teeth processed by the rotating knife dish by vector method and the contact characteristics were studied in the research papers.

In the studied of cylindrical gears with curvilinear shaped teeth processed by parallel translating mechanism, Song Aiping from Yang Zhou University did many interesting work. The tooth surface equation, bending stress and modification methods under ideal parameters were studied and a translational processing device with parallel linkage was put forward by Song Aiping [10-15]. Then, Sun Zhijun [17] from Sichuan University raised the translational processing device by planetary gear train. But there are rare studies on the actual machining process. However, the tooth surface equation, bending stress, modification methods and undercutting in the actual machining process is the most important.

In the present paper, to study the tooth surface equation and undercutting of cylindrical gears with curvilinear shaped teeth processed by parallel translating mechanism, the tooth surface equation and meshing conditions were deduced by the method of coordinate transformation based on the translational processing device referred in literature [16] and [17]. The computer simulation was done in 3-D software and the 3-D model was obtained. The present study has some reference value for the design of the cylindrical gears with curvilinear shaped teeth processed by parallel translating mechanism.

\* Corresponding author e-mail:

## 2. Two Translational Processing Device and Simplified Mechanism

A translational processing device, invented by Song Aiping [16], is shown in Figure 1, and another translational processing device, invented by Sun Zhijun [17], is shown in Figure 2.

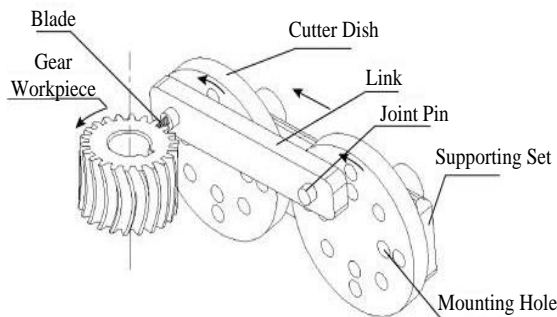


Fig. 1. Translational processing device by parallel linkage

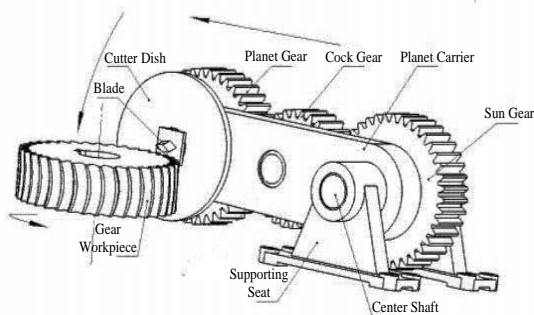


Fig. 2. Translational processing device by planetary gear train

In the processing device 1, the parallel linkage was adopted. The tool was installed on the translational connecting rod. When the rotation connecting rod rotated with the prime motor, the tool moved translational. Then the side of the blade moved with the same radius. With the feed movement of the gear workpiece, the cylindrical gears with curvilinear shaped teeth could be obtained.

In the processing device 2, the planetary gear train was obtained as the knife rest. Through analysis, there are some special points in the planetary gear train shown in Figure 2. With the planetary gear train moved, the tool moved translational too. When the gear workpiece rotated and the planetary gear train does translational movement, the gear was generated. In the same time, the device 2 could avoid the vibration caused by the unbalanced quality in the device 1.

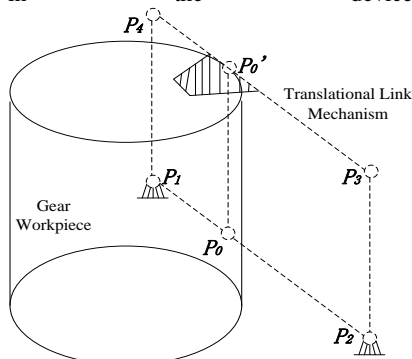


Fig. 3. The mechanism diagram of translational processing device

The mechanism in device 1 and device 2 was simplified just as the parallel translating mechanism shown in Figure 3. In Figure 3, the point  $O$  is the center of the gear workpiece, then  $P_1, P_2, P_3$  and  $P_4$  are the four hinges of the parallel translating mechanism.  $P_1P_2$  is the static link,  $P_3P_4$  is the translational link.  $P_1P_4$  and  $P_2P_3$  are the rotation links. Let the  $P_0P_0'$  as the virtual link and represented by imaginary line, then the point  $P_0$  and  $P_0'$  are the virtual hinges of the virtual link.

## 3. Tooth Surface Equation

### 3.1. The Coordinate Systems

To study the forming process and forming tooth surface of cylindrical gears with curvilinear shaped teeth processed by parallel translating mechanism, a coordinate system was set up in the translational processing system.

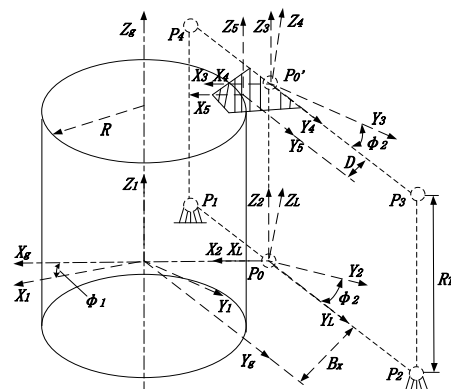


Fig. 4. The coordinate system settings of the translational processing system

Taking the mechanism diagram of translational processing device as the research object shown in Figure 3, the coordinate systems were set up as shown in Figure 4. The static coordinate systems are  $S_g(O_g X_g Y_g Z_g)$  and  $S_l(O_l X_l Y_l Z_l)$ , and the other coordinate systems are moving coordinate systems. The coordinate system  $S_l(O_l X_l Y_l Z_l)$  was connected with the static link rack  $P_1P_2$  of the parallel linkage,  $O_l$  is located on the endpoint  $P_0$  of the virtual link, the axle  $O_l Y_l$  is along the direction of static link rack and the axle  $O_l Z_l$  has the same direction of the gear workpiece. The direction of the three axle of the coordinate system  $S_g(O_g X_g Y_g Z_g)$  has the same direction of the coordinate system  $S_l(O_l X_l Y_l Z_l)$ , but the origin of coordinate  $O_g$  is located at the center of the gear workpiece. When the gear workpiece moves, the coordinate system  $S_g(O_g X_g Y_g Z_g)$  moved parallel, but there is no rotational motion in the system  $S_g(O_g X_g Y_g Z_g)$ .

The coordinate system  $S_1(O_1X_1Y_1Z_1)$  is connected with the gear workpiece, and does the parallel and rotational motion with the gear workpiece at the same time. The axle  $O_gZ_g$  and  $O_1Z_1$  is overlapping and has the same direction, the origin of coordinate is the center of the gear workpiece. The coordinate system  $S_2(O_2X_2Y_2Z_2)$  is connected with the virtual rotation connecting rod  $P_0P_0'$ , the origin of coordinate  $O_2$  is located at point  $P_0$ , then  $O_2X_2$  and  $O_1X_1$  are overlapped to each other. The coordinate system  $S_3(O_3X_3Y_3Z_3)$  is also connected with the virtual rotation connecting rod  $P_0P_0'$  and the directions of the three axles have the same direction with coordinate system  $S_2(O_2X_2Y_2Z_2)$ , but the origin of coordinate  $O_3$  is located at point  $P_0'$  which is the other end of the virtual link. The coordinate system  $S_4(O_4X_4Y_4Z_4)$  is connected with the translational connecting rod of the parallel linkage, the origin of coordinate  $O_4$  is the point  $P_0'$  and the axle  $O_4X_4$  is the same to the axle  $O_3X_3$ . At last, the coordinate system  $S_5(O_5X_5Y_5Z_5)$  is connected on the cutter blade to measure the geometric parameters, the axles of coordinate system  $S_5(O_5X_5Y_5Z_5)$  have the same direction to  $S_4(O_4X_4Y_4Z_4)$ , and the axle  $O_5X_5$  is the same to the axle  $O_4X_4$ , then  $\overline{O_4O_5} = D$ .

The installation position error of cutter is inevitable, in which includes angle deviation and position deviation. There are just position deviation between the rack and the gear workpiece (the position deviation between point  $O_g$  and  $O_l$ ) being considered. The relative projection position between point  $O_g$  and  $O_l$  is shown in Figure 5.

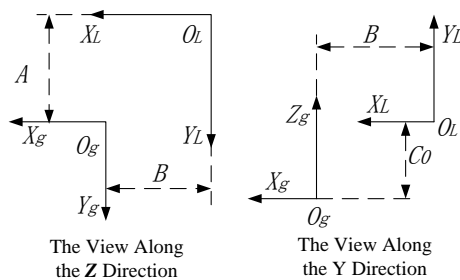


Fig. 5. The relative projection position between point  $O_g$  and  $O_l$

In Figure 5,  $A$ ,  $B$ ,  $C$  is the distance between point  $O_g$  and  $O_l$  at  $Y$ ,  $X$ ,  $Z$  direction, respectively.

$A_0$ ,  $B_0$ ,  $C_0$  were the static initial installation error, and  $B_x$  is the ideal installation size at  $X$  direction. Then:

$$B_x = R + D = R + \overline{O_4O_5} \tag{1a}$$

$$A = A_0 + V_T = A_0 + R\phi_1 \tag{1b}$$

Where,  $\phi_1$  is the rotational angle of the gear workpiece;  $V_T$  is the feed displacement,  $V_T = R\phi_1$ .

### 3.2. The Cross-Section Shape of Cutting Tool

In the gear machining, the tool geometry have big influence for the forming of the gear tooth surface. The tooth surface equation is determined by the tool geometry and relative motion relationship between the cutting tooth and the gear workpiece. In common research, the effective cutting tool section of the cutting tool was taken to study the forming process of the gears.

The cutting tool section was regarded as with sharp points in some studies [3-4] when the geometry parameter of cutting tool was measured as Figure 6 shows, but in other studies [7-8], the cutting tool section was with rounded corners as shown in Figure 7.

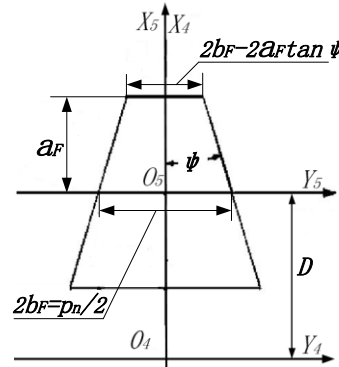


Fig. 6. The shape and parameter of cutting tool with sharp points

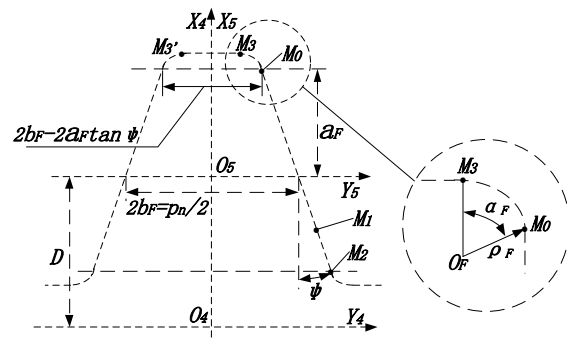


Fig. 7. The shape and parameter of cutting tool with rounded corners

In the actual production process, the cutting tool with sharp points doesn't exist, and the rounded corners always exist due to the factor of design and friction. To close to the actual production, the cutting tool with rounded corners was adopted to study the tooth surface equation and undercutting conditions of the cylindrical gears with curvilinear shaped teeth. The cutting tool geometry parameters are shown in Figure 7.

From Figure 7, the equation of cutting tool blade side could be shown as Eq. (2a) in the coordinate system  $S_5(O_5X_5Y_5Z_5)$ :

$$\begin{cases} \vec{r}_5 = x_5 \vec{i}_5 + y_5 \vec{j}_5 + z_5 \vec{k}_5 \\ x_5 = -l \cos \psi + a_F \\ y_5 = \pm(l \sin \psi + b_F - a_F \tan \psi) \\ z_5 = 0 \end{cases} \quad (2a)$$

The chisel edge of cutting tool could be shown as Eq. (2b) in the coordinate system  $S_5(O_5X_5Y_5Z_5)$ .

$$\begin{cases} \vec{r}_5' = x_5' \vec{i}_5 + y_5' \vec{j}_5 + z_5' \vec{k}_5 \\ x_5' = a_F + \rho_F (1 - \cos \alpha_F) \\ y_5' = l [a_F + \rho_F (1 - \cos \alpha_F)] \\ z_5' = 0 \end{cases} \quad (2b)$$

The rounded corners of cutting tool could be shown as Eq. (2c) in the coordinate system  $S_5(O_5X_5Y_5Z_5)$ .

$$\begin{cases} \vec{r}_5'' = x_5'' \vec{i}_5 + y_5'' \vec{j}_5 + z_5'' \vec{k}_5 \\ x_5'' = a_F + \rho_F \cos \alpha_F + \rho_F \cos \theta'' \\ y_5'' = \pm(b_F - a_F \tan \psi - \rho_F \sin \alpha_F) + \rho_F \sin \theta'' \\ z_5'' = 0 \end{cases} \quad (2c)$$

where, the  $l$ ,  $l'$  and  $\theta''$  are expression parameter in the parameter-vector equation(2a)-(2c). The range of  $l$ ,  $l'$  and  $\theta''$  are  $0 \leq l \leq 2a_F$ ,  $|l'| \leq 1$  and

$$\frac{\pi}{2} - \alpha_F \leq \theta'' \leq \frac{\pi}{2}, \text{ respectively.}$$

### 3.3. Tooth Surface Composition of Cylindrical Gears with Curvilinear Shaped Teeth

From the literature [4, 19], there are three main surface in the production process. The three surfaces are work surface, tooth bottom surface and dedendum surface, respectively. The work surface is processed by the cutting tool blade side  $M_0M_2$ , the tooth bottom surface is processed by the chisel edge of cutting tool  $M_3M_3'$ , and the dedendum surface is processed by the rounded corners  $M_0M_3$  and  $M_0'M_3'$ .

### 3.4. Surface Equation of the Working Tooth Surface

From section 2.3, the work surface of the cylindrical gears with curvilinear shaped teeth was machined by the cutting tool blade side  $M_0M_2$ . When the cutting tool blade side  $M_0M_2$  rotates with the rack as the speed  $\omega_2$ , the cutting tool generatrix  $\Sigma_1$  will be generated. At the same time, the gear workpiece rotates as the speed  $\omega_1$  and moves with feed speed  $v_1 = R\omega_1$ , then the cutting tool generatrix  $\Sigma_1$  will envelope out the work surface  $\Sigma_2$ .

When the cutting tool generatrix  $\Sigma_1$  moves, the surface  $\Sigma_1$  will form a family of surfaces  $\Sigma_{\phi_1}$  in the coordinate system  $S_1(O_1X_1Y_1Z_1)$  by coordinate transformation from coordinate system  $S_l(O_lX_lY_lZ_l)$  to  $S_1(O_1X_1Y_1Z_1)$ . The surface  $\Sigma_2$  is the envelope of the family of surfaces  $\Sigma_{\phi_1}$  due to the work surface  $\Sigma_2$  is tangent to  $\Sigma_{\phi_1}$  everywhere.

#### 3.4.1. The Cutting Tool Generatrix Equation

From the above state, the cutting tool generatrix  $\Sigma_1$  could be obtained by coordinate transformation from  $S_5(O_5X_5Y_5Z_5)$  to  $S_l(O_lX_lY_lZ_l)$ .

$$\vec{r}_l = M_{l5} \vec{r}_5 \quad (3)$$

Where,  $M_{l5}$  is the coordinate transformation matrix from coordinate system  $S_5(O_5X_5Y_5Z_5)$  to  $S_l(O_lX_lY_lZ_l)$ :

$$M_{l2} = \begin{bmatrix} 1 & 0 & 0 & 0 \\ 0 & \cos \phi_2 & -\sin \phi_2 & 0 \\ 0 & \sin \phi_2 & \cos \phi_2 & 0 \\ 0 & 0 & 0 & 1 \end{bmatrix} \quad (4a)$$

$$M_{23} = \begin{bmatrix} 1 & 0 & 0 & 0 \\ 0 & 1 & 0 & 0 \\ 0 & 0 & 1 & R_T \\ 0 & 0 & 0 & 1 \end{bmatrix} \quad (4b)$$

$$M_{34} = \begin{bmatrix} 1 & 0 & 0 & 0 \\ 0 & \cos \phi_2 & \sin \phi_2 & 0 \\ 0 & -\sin \phi_2 & \cos \phi_2 & 0 \\ 0 & 0 & 0 & 1 \end{bmatrix} \quad (4c)$$

$$M_{45} = \begin{bmatrix} 1 & 0 & 0 & D \\ 0 & 1 & 0 & 0 \\ 0 & 0 & 1 & 0 \\ 0 & 0 & 0 & 1 \end{bmatrix} \quad (4d)$$

$$\begin{aligned} M_{l5} &= M_{l2} M_{23} M_{34} M_{45} \\ &= \begin{bmatrix} 1 & 0 & 0 & D \\ 0 & 1 & 0 & -R_T \sin \phi_2 \\ 0 & 0 & 1 & R_T \cos \phi_2 \\ 0 & 0 & 0 & 1 \end{bmatrix} \end{aligned} \quad (4e)$$

Take the formula (2a) and (4e) into (3), and the cutting tool generatrix  $\Sigma_1$  could be got as:

$$\begin{cases} \vec{r}_l = x_l \vec{i}_l + y_l \vec{j}_l + z_l \vec{k}_l \\ x_l = -l \cos \psi + a_F + D \\ y_l = \pm(l \sin \psi + b_F - a_F \tan \psi) - R_T \sin \varphi_2 \\ z_l = R_T \cos \varphi_2 \end{cases} \quad (5)$$

3.4.2. Surface Family Equation

When the gear workpiece moved relative to the rack at parameter  $\varphi_1$ , the cutting tool generatrix  $\Sigma_1$  will generate a family of surfaces  $\Sigma_{\varphi_1}$  in the coordinate system  $S_1(O_1X_1Y_1Z_1)$ . The family of surfaces  $\Sigma_{\varphi_1}$  could be got by the following formula (6):

$$\vec{r}_1 = M_{1l} \vec{r}_l \quad (6)$$

Where,  $M_{1l}$  is the coordinate transformation matrix from the coordinate system  $S_l(O_lX_lY_lZ_l)$  to the coordinate system  $S_1(O_1X_1Y_1Z_1)$ .

$$M_{1g} = \begin{bmatrix} \cos \varphi_1 & -\sin \varphi_1 & 0 & 0 \\ \sin \varphi_1 & \cos \varphi_1 & 0 & 0 \\ 0 & 0 & 1 & 0 \\ 0 & 0 & 0 & 1 \end{bmatrix} \quad (7a)$$

$$M_{gl} = \begin{bmatrix} 1 & 0 & 0 & -(B_0 + R + D) \\ 0 & 1 & 0 & -(A_0 + R\varphi_1) \\ 0 & 0 & 1 & C_0 \\ 0 & 0 & 0 & 1 \end{bmatrix} \quad (7b)$$

Mark  $B = -(B_0 + R + D)$ ,  $A = -(A_0 + R\varphi_1)$  and  $C = C_0$ , where  $B_0$ ,  $A_0$ ,  $C_0$  is the static installation error between the coordinate system  $S_l(O_lX_lY_lZ_l)$  with the coordinate system  $S_g(O_gX_gY_gZ_g)$ .

$$\begin{aligned} M_{1l} &= M_{1g} M_{gl} \\ &= \begin{bmatrix} \cos \varphi_1 & -\sin \varphi_1 & 0 & B \cos \varphi_1 - A \sin \varphi_1 \\ \sin \varphi_1 & \cos \varphi_1 & 0 & B \sin \varphi_1 + A \cos \varphi_1 \\ 0 & 0 & 1 & C \\ 0 & 0 & 0 & 1 \end{bmatrix} \end{aligned} \quad (7d)$$

Take the formula (7d) and (5) into (6), then the equation for family of surfaces  $\Sigma_{\varphi_1}$  could be obtained as formula (8) shows:

$$\begin{cases} \vec{r}_1 = x_1 \vec{i}_1 + y_1 \vec{j}_1 + z_1 \vec{k}_1 \\ x_1 = Q_1 \cos \varphi_1 - Q_2 \sin \varphi_1 + R_T \sin \varphi_1 \sin \varphi_2 \\ y_1 = Q_1 \sin \varphi_1 + Q_2 \cos \varphi_1 - R_T \cos \varphi_1 \sin \varphi_2 \\ z_1 = R_T \cos \varphi_2 + C \end{cases} \quad (8)$$

Where,

$$Q_1 = -l \cos \psi + a_F + D + B \quad (9a)$$

$$Q_2 = A \pm (l \sin \psi + b_F - a_F \tan \psi) \quad (9b)$$

3.4.3. Envelope Condition/Meshing Equation

The family of surfaces  $\Sigma_{\varphi_1}$  is a single parameter curved surface with the movement parameter  $\varphi_1$ , and the surface parameter coordinate of  $\Sigma_1$  are  $l$  and  $\varphi_2$ . So the family of surfaces  $\Sigma_{\varphi_1}$  was expressed as:

$$\vec{r}_1 = \vec{r}_1(l, \varphi_2, \varphi_1) \quad (10)$$

The envelope condition or meshing function could be obtained as the formula (11).

$$\left( \frac{\partial \vec{r}_1}{\partial l}, \frac{\partial \vec{r}_1}{\partial \varphi_2}, \frac{\partial \vec{r}_1}{\partial \varphi_1} \right) = 0 \quad (11)$$

For the differences of the two sides of generatrix, mark the cutting tool generatrix of the right cutting tool blade side in Figure 7 is  $\Sigma_1^{(1)}$ , and the cutting tool generatrix of the left cutting tool blade side is  $\Sigma_1^{(2)}$  to convenience study. Cutting tool generatrix  $\Sigma_1^{(1)}$  forms the family of surfaces  $\Sigma_{\varphi_1}^{(1)}$  in coordinate system  $S_1(O_1X_1Y_1Z_1)$  and  $\Sigma_1^{(2)}$  forms the family of surfaces  $\Sigma_{\varphi_1}^{(2)}$ .

In the present study, just envelope condition for the family of surfaces  $\Sigma_{\varphi_1}^{(1)}$  was deduced. The envelope condition of  $\Sigma_{\varphi_1}^{(2)}$  could be obtained just repeat the derivation process again. For the family of surfaces  $\Sigma_{\varphi_1}^{(1)}$ :

$$\frac{\partial \vec{r}_1^{(1)}}{\partial l} = -\cos(\psi - \varphi_1) \vec{i}_1 + \sin(\psi - \varphi_1) \vec{j}_1 \quad (12a)$$

$$\frac{\partial \vec{r}_1^{(1)}}{\partial \varphi_2} = R_T (\sin \varphi_1 \cos \varphi_2 \vec{i}_1 - \cos \varphi_1 \cos \varphi_2 \vec{j}_1 - \sin \varphi_2 \vec{k}_1) \quad (12b)$$

$$\begin{aligned} \frac{\partial \vec{r}_1^{(1)}}{\partial \varphi_1} &= [(-Q_1 + R) \sin \varphi_1 - Q_2 \cos \varphi_1 + R_T \cos \varphi_1 \sin \varphi_2] \vec{i}_1 \\ &\quad + [(Q_1 - R) \cos \varphi_1 - Q_2 \sin \varphi_1 + R_T \sin \varphi_1 \sin \varphi_2] \vec{j}_1 \end{aligned} \quad (12c)$$

So, the envelope condition or meshing function of the family of surfaces  $\Sigma_{\varphi_1}^{(1)}$  could be expressed as:

$$\begin{aligned} \Phi^{(1)} &= \left( \frac{\partial \vec{r}_1}{\partial l}, \frac{\partial \vec{r}_1}{\partial \varphi_2}, \frac{\partial \vec{r}_1}{\partial \varphi_1} \right) \\ &= R_T \sin \varphi_2 [(R - Q_1) \cos \psi + (Q_2 - R_T \sin \varphi_2) \sin \psi] \\ &= R_T \sin \varphi_2 [(R + l \cos \psi - a_F - D - B) \cos \psi + (-A_0 \\ &\quad - R\varphi_1 + l \sin \psi + b_F - a_F \tan \psi - R_T \sin \varphi_2) \sin \psi] \\ &= 0 \end{aligned} \quad (13)$$

### 3.4.4. The Tooth Surface Equation

From formula (8) and formula (13), the tooth surface equation of the cylindrical gears with curvilinear shaped teeth processed by parallel translating mechanism could be expressed as:

$$\begin{cases} \vec{r}_1 = \vec{r}_1(l, \varphi_2, \varphi_1) \\ \Phi^{(1)} = 0 \end{cases} \quad (14)$$

When the installation error is ignored, take the  $B_0$ ,  $A_0$ ,  $C_0$  as 0 and the tooth surface equation in the ideal installation parameters could be obtained.

### 4. Undercutting Condition of Cylindrical Gears with Curvilinear Shaped Teeth Processed by Parallel Translating Mechanism

From literature [7, 19], there will be the condition of undercutting when the installation position of cutting tool is not correct. And through selecting the installation position, the undercutting of the gear could be avoided.

In the parameters of the tooth surface equation for the cylindrical gears with curvilinear shaped teeth processed by parallel translating mechanism, the parameters  $l, \varphi_2$  are surface parameters of the cutting tool generatrix  $\Sigma_1$ , while the parameter  $\varphi_1$  is the motion envelope parameters in the process processing. From the derivations in [7, 18], there are:

$$-v_l^{(1)} = \frac{\partial \vec{r}_1}{\partial l} \frac{dl}{dt} + \frac{\partial \vec{r}_1}{\partial \varphi_2} \frac{d\varphi_2}{dt} \quad (15)$$

Find the derivative of envelope condition shown in formula (13), we could get:

$$\frac{\partial \Phi}{\partial l} \frac{dl}{dt} + \frac{\partial \Phi}{\partial \varphi_2} \frac{d\varphi_2}{dt} = - \frac{\partial \Phi}{\partial \varphi_1} \frac{d\varphi_1}{dt} \quad (16)$$

The formula (15) and formula (16) could determine a curve  $L$  in the coordinate system  $S_l(O_l X_l Y_l Z_l)$ . Through limiting the position of the cutting tool generatrix  $\Sigma_1$  by the curve  $L$ , the surface  $\Sigma_1$  could avoid to cause singular points on the surface  $\Sigma_2$ , so the undercutting is avoided.

The curve  $L$  could be determined by the formula (17):

$$\begin{cases} \vec{r}_l = \vec{r}_l(l, \varphi_2) \\ \Phi = \Phi(l, \varphi_2, \varphi_1) = 0 \\ F = F(l, \varphi_2, \varphi_1) = 0 \end{cases} \quad (17)$$

Where,  $F(l, \varphi_2, \varphi_1) = \Delta_1^2 + \Delta_2^2 + \Delta_3^2 = 0$  is the necessary and sufficient condition of appearing the undercutting and singular points existing on the surface  $\Sigma_2$ .  $\Delta_1$ ,  $\Delta_2$ ,  $\Delta_3$ ,  $\Delta_4$  could be expressed, respectively, as:

$$\Delta_1 = \begin{vmatrix} \frac{\partial x_l}{\partial l} & \frac{\partial x_l}{\partial \varphi_2} & -v_{xl}^{(1)} \\ \frac{\partial y_l}{\partial l} & \frac{\partial y_l}{\partial \varphi_2} & -v_{yl}^{(1)} \\ \frac{\partial \Phi}{\partial l} & \frac{\partial \Phi}{\partial \varphi_2} & -\frac{\partial \Phi}{\partial \varphi_1} \frac{d\varphi_1}{dt} \end{vmatrix} \quad (18a)$$

$$\Delta_2 = \begin{vmatrix} \frac{\partial x_l}{\partial l} & \frac{\partial x_l}{\partial \varphi_2} & -v_{xl}^{(1)} \\ \frac{\partial z_l}{\partial l} & \frac{\partial z_l}{\partial \varphi_2} & -v_{zl}^{(1)} \\ \frac{\partial \Phi}{\partial l} & \frac{\partial \Phi}{\partial \varphi_2} & -\frac{\partial \Phi}{\partial \varphi_1} \frac{d\varphi_1}{dt} \end{vmatrix} \quad (18b)$$

$$\Delta_3 = \begin{vmatrix} \frac{\partial y_l}{\partial l} & \frac{\partial y_l}{\partial \varphi_2} & -v_{yl}^{(1)} \\ \frac{\partial z_l}{\partial l} & \frac{\partial x_l}{\partial \varphi_2} & -v_{zl}^{(1)} \\ \frac{\partial \Phi}{\partial l} & \frac{\partial \Phi}{\partial \varphi_2} & -\frac{\partial \Phi}{\partial \varphi_1} \frac{d\varphi_1}{dt} \end{vmatrix} \quad (18c)$$

$$\Delta_4 = \begin{vmatrix} \frac{\partial x_l}{\partial l} & \frac{\partial x_l}{\partial \varphi_2} & -v_{xl}^{(1)} \\ \frac{\partial y_l}{\partial l} & \frac{\partial y_l}{\partial \varphi_2} & -v_{yl}^{(1)} \\ \frac{\partial z_l}{\partial l} & \frac{\partial x_l}{\partial \varphi_2} & -v_{zl}^{(1)} \end{vmatrix} \quad (18d)$$

### 5. 3-D Model of Cylindrical Gears with Curvilinear Shaped Teeth

To study the machining process, tooth surface molding method and the tooth surface features of the cylindrical gears with curvilinear shaped teeth processed by parallel translating mechanism, the relevant program was compiled by Open Grip and operated in 3-D software. The parameters were shown in Table 1. Figure 8 is a 3-D model of the gear pair.

**Table 1.** Gear parameters in simulation processing

Parameters	Pinion	Gear
Number of teeth	25	36
Modulus	4	4
Pressure angle	20	20
Tooth width	60	60
Tooth line radius	150	150

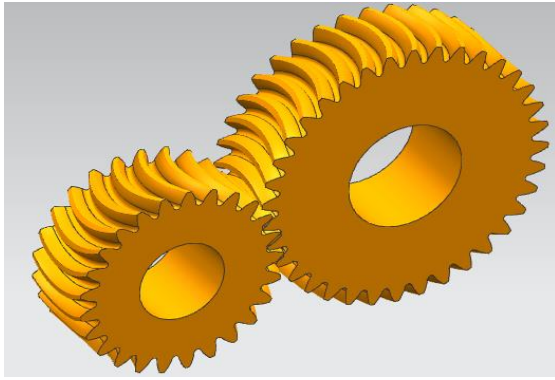


**Fig. 8.** 3-D model of gear pair

From the model in Figure 8, the mathematical model correctness of the cylindrical gears with curvilinear shaped teeth processed by parallel translating mechanism could be verified. Using the interference inspection tool in the software, there is no interference phenomenon in the gear pair shown in Figure 8, and the meshing transmission requirements could be achieved.

## 6. Conclusions

In the present paper, taking the cylindrical gears with curvilinear shaped teeth processed by parallel translating mechanism as the research object, the parallel translating mechanism was taken as a parallel linkage mechanism, then the virtual rotation connecting rod was considered between the static link and the cutting tool.

1. The relevant coordinate systems were established and the tooth surface equation of the cylindrical gears with curvilinear shaped teeth was deduced by differential geometry and the method of matrix transformation.
2. The envelope condition of the tooth surface equation was analyzed. Based on the research in the literature [19], the undercutting condition of the cylindrical gears with curvilinear shaped teeth was revealed.
3. The process of the machining process for the cylindrical gears with curvilinear shaped teeth was simulated by Grip programming language. The 3-D model of cylindrical gears with curvilinear shaped teeth was got.

From the present paper, some theoretical basis could be provided to the processing error analysis of the cylindrical gears with curvilinear shaped teeth.

## Acknowledgments

This project is supported by National Natural Science Foundation of China (Grant No. 51375320).

## References

- [1] Di Yutao, Chen Ming. "The generation principle and mesh characteristic of arcuate tooth trace cylindrical gear". *Mechanical Engineer*, No.9, 2006, 50-52.
- [2] Di Yutao, Hong Xiaohui, Chen Ming. "Generation principle of arcuate tooth trace cylindrical gear". *Journal of Harbin Bearing*, Vol.38, No.3, 2006. 58-61.
- [3] WANG Shaojiang, HOU Li, DONG Lu, XIAO Huajun. "Modeling and Strength Analysis of Cylindrical Gears with Curvilinear Shape Teeth for Manufacture". *JOURNAL OF SICHUAN UNIVERSITY (ENGINEERING SCIENCE EDITION)*, Vol.44, No.3, 2012, 210-215.
- [4] XIAO Huajun, HOU Li, DONG Lu, JIANG Yiqiang, WEI Yongqiao. "Mathematical Modeling of Rotary Cutter Arc Tooth Line of Cylindrical Gear Shaped by Origin Face of Rotary Cutter". *JOURNAL OF SICHUAN UNIVERSITY (ENGINEERING SCIENCE EDITION)*, Vol.45, No.3, 2013, 171-175.
- [5] REN Wenjuan, HOU Li, JIANG Ping, LENG Song. "Machinability model of the arcuate tooth trace cylindrical gear". *Manufacturing Technology & Machine Tool*, No.6, 2012, 76-78.
- [6] JIANG Ping, HOU Li, REN Wen-juan, LENG Song. Molding "Principle and Meshing Analysis of Curvilinear Gear". *Machinery Design & Manufacture*, No.7, 2012, 197-199.
- [7] Tseng R T, Tsay C B. "Mathematical model and undercutting of cylindrical gears with curvilinear shaped teeth". *Mechanism and Machine Theory*, Vol.36, 2001, 1189-1202.
- [8] Tseng R T, Tsay C B. "Contact characteristics of cylindrical gears with curvilinear shaped teeth". *Mechanism and Machine Theory*, No.9, 2004, 905-919.
- [9] Tseng R T, Tsay C B. "Mathematical model and surface deviation of cylindrical gears with curvilinear shaped teeth cut by a hob cutter". *ASME Journal of Mechanical Design*, Vol.4, 2005, 982-987.
- [10] Wu Weiwei, Song Aiping, Wang Zhaolei, Xu Xiangcui. "Stress Analysis of the Involute Arc Cylindrical Gear". *Journal of Mechanical Transmission*, Vol.34, No.11, 2010, 38-44.
- [11] Wang Zhaolei. "Mesh Principle and Drive Strength Analysis of Involute Arc Cylindrical Gear". Yangzhou University, 2009.
- [12] Wu Weiwei, Song Aiping, Wang Zhaolei. "Research on the tooth root stress of the involute arc cylindrical gear". *Machinery Design & Manufacture*, No.11, 2009, 227-229.
- [13] SONG Aiping, WU Weiwei, GAO Shang, GAO Wenjie. "The Ideal Geometry Parameters of Arch Cylindrical Gear and Its Process Method". *JOURNAL OF SHANG HAI JIAO TONG UNIVERSITY*, Vol.44, No.12, 2010, 1735-1740.
- [14] Wu Weiwei. "Research on the Processing Method and Processing Device of Involute Arc Cylindrical Gear". Yangzhou University, 2010.
- [15] Xu Xiangcui. "Mesh Elastic Deformation and Modification Method of Involute Arc Cylindrical Gear". Yangzhou University, 2011.
- [16] Song Aiping. "Processing Method and Processing Device of Arc Cylindrical Gear". China, Patent: ZL200410041297.2, 2005-02-23.
- [17] Sun Zhijun, "A Translational Processing Device for Cylindrical Gears with Curvilinear Shaped Teeth". China, Patent: ZL201310110784.9.
- [18] Tang Qian, Jin Xiaofeng, Fan Qiulei. "Parametric coordination and simulation study on nonstandard spur gears". *Jordan Journal of Mechanical and Industrial Engineering*, Vol 8, No 2, 2014, 50-55.
- [19] Litven. *Gear Geometry and Applied Theory*. Shanghai: Science and Technology Documents Press of Shanghai, 2008.
- [20] Wu Daren, Luo Jiashun. *Theory of Gearing*. Beijing: Science Press, 1985.



# Multimode Input Shaping Control of Flexible Robotic Manipulators Using Frequency-Modulation

Ziyad Masoud <sup>a\*</sup>, Mohammad Nazzal <sup>b,c</sup>, Khaled Alhazza <sup>d</sup>

<sup>a</sup> Department of Mechatronics Engineering, German Jordanian University, Amman 11180, Jordan

<sup>b</sup> Department of Mechanical Engineering, German Jordanian University, Amman 11180, Jordan

<sup>c</sup> Department of Mechanical Engineering, American University of Sharjah, Sharjah, UAE,

<sup>d</sup> Department of Mechanical Engineering, Kuwait University, Kuwait City, Kuwait

Received Dec. 22, 2015

Accepted May, 14, 2016

## Abstract

Robotic manipulators used in heavy industries, such as the automotive industry, are generally bulky. Driving such manipulators requires large actuators. In many cases, manipulators hardly carry any significant load compared to their sizes, such as those used for performing spot welding. However, the manipulators are oversized to avoid vibrations caused by high input command profiles. Lighter flexible manipulators, on the other hand, are superior in terms of cost and energy consumption. However, size reduction comes at a price of slower performance in order to reduce inertia induced vibrations. In the present work, a command shaping strategy is developed to facilitate operating flexible manipulators at higher speeds while eliminating inertia excited vibrations. The strategy is based on input shaping techniques complemented with a multimode frequency modulation control system. The performance of the proposed strategy is demonstrated on a thin beam model of a robotic arm, using numerical and finite element simulations.

© 2016 Jordan Journal of Mechanical and Industrial Engineering. All rights reserved

**Keywords:** Frequency-modulation, input shaping, multimode, flexible manipulator, hanging beam.

## 1. Introduction

In heavy industries, such as the automotive industry, robotic manipulators are generally heavy and bulky. Many of those manipulators perform tasks that do not involve carrying or moving large payloads. As a matter of fact, some manipulators do not carry any load. They just perform assembly tasks, such as robots used for welding, drilling, etc. Industrial robots are made bulky for one main purpose; to guarantee positioning accuracy of their end effectors. Geometrical oversizing of robotic manipulators boosts their stiffness and reduces vibrations that may compromise operations precision. As a result, industrial robots require large powerful actuators that consume excessive amounts of energy.

Although energy efficient, the structural flexibility of light weight manipulator is a major drawback. Light weight manipulators operate at lower speeds, compared to their heavy counterparts, to avoid inertia excited vibrations. Structural flexibility of light manipulators compromises operations precision [1]. Bearing in mind that operations in many heavy industries are continuous all

year long, the amount of energy savings through the use of light manipulators is substantial. The slow operation speed penalty can be elevated by implementing control systems that eliminate vibrations in light manipulators operating at high speeds comparable to those achievable by heavy manipulators.

It is for such reasons that the dynamics and vibration control of beams have received large attention during the past few decades. Ample literature is published on the vibration and control of flexible structures [2, 3]. Many control strategies have been investigated for the control of flexible manipulators including optimal control, adaptive control, fuzzy logic control, neural networks, input shaping, and others [4-10]. Research included the implementation of dominant mode linear and nonlinear vibration control of flexible structures [6], and multimode simultaneous control for more flexible structures when the dominant mode approach is insufficient [7].

Open-loop control systems are ideal for the elimination of inertia excited vibrations. One of the most common and practical open-loop control systems is known as input shaping [11]. Inertia excited vibrations are eliminated by deriving command signals to actuators that mitigate their own excited vibration. Input shaping technique is based on

\* Corresponding author e-mail: ziyad.masoud@gnu.edu.jo.

convolving a sequence of impulses with a general input command. The impulses are precisely timed so that the convolved command eliminates its own excited vibration at the conclusion of the command. Essential concepts of input shaping were published and patented by Gimpel and Calvert in 1952 and by Calvert and Gimpel in 1957 [12, 13]. Because of its sensitivity to modeling uncertainty, input shaping was not widely used until it was made popular by the work of Singer and Seering [14] and Singer *et al.* [15] on robust input shaping methods. Since then, research on input shaping control surged to include different input shaping techniques for single mode and multimode flexible structures such as Zero-Vibration (ZV), Zero-Vibration-Derivative (ZVD), Zero Vibration Derivative (ZVDD), Specified Insensitivity (SI), and Extra-Insensitive (EI) input shapers [11, 16].

As flexible structures, robotic arm are multimode vibrating systems. Controlling these systems commands the use of multimode input shaping schemes. Multimode input shapers can be classified into two main groups; convolved shapers and simultaneous shapers. Convolved shapers involve convolving multiple sequences of impulses, each sequence targeting one vibration mode of a multimode system [17-20]. However, in some cases, the frequencies involved may be so high that convolved input shapers become practically inapplicable due to bandwidth limitations [18]. Simultaneous shapers may produce faster response, however, they generally exhibit lower robustness compared to convolved shapers [21-23]. Shapers may involve positive and negative impulses [24, 25]. Input shapers containing negative impulses have several advantages [26, 27].

Input shaping can be implemented as a standalone control strategy, or as a hybrid combination with other control strategies for improved robustness [4, 28]. Standalone multimode input shapers suffer an implementation drawback due to the large number of impulses involved in their designs. Depending on the control hardware used, mismatch between impulses and sampling rates may result in performance degradation [17, 21, 22]. To overcome this drawback, hybrid combinations of single-mode input shaping with other control strategies are utilized including combining single-mode shapers with different types of filters, such as notch, low-pass, band-stop, and time-delay filters [29-34]. An optimization technique taking into consideration hardware sampling rates was derived by Alghanim *et al.* [35] in an attempt to overcome this problem.

Pre-shaped command techniques are used to overcome excessive impulses in an input command. Continuous smooth commands may reduce or eliminate impulses in shaped commands. Erkorkmaz and Altintas [36] used quintic spline trajectory generation algorithm to generate continuous position, velocity, and acceleration profiles for high speed CNC systems. Xie *et al.* [37] introduced a method to reduce vibration in flexible systems by smoothing the original command. Wave-form commands

were also used to reduce the number of impulses and jerks in shaped input commands [38-41].

To reduce the number of impulses in multimode input shapers, Singh and Heppler [18] showed that a single-mode shaper can eliminate vibrations at all frequencies that are odd-multiples of the design frequency of the single-mode shaper used. Their trials were based on finding a common frequency such that all modes of a multimode system are odd-multiples of this frequency. However, there were no guarantees that such a frequency existed in a multimode system. Later, single-mode pre-shaped commands were implemented on an approximate model of a two-mode system for which such a common frequency exists [28]. Virtual feedback system was used to match the response of the exact model of the system to the approximate model. Another attempt, known as frequency-modulation input shaping, was based on modifying the frequencies of a multimode system using model-based feedback to the point where such a common frequency exists [42, 43].

In the present study, a flexible Euler-Bernoulli hanging beam is used to model a robotic arm. Flexible beams exhibit broad spectrum of resonant frequencies. This wide spectrum makes the use of multimode impulse shapers impractical. This paper describes a multimode frequency-modulation input shaping strategy used to shape acceleration commands to the base of the robot arm model. Model-based feedback is used to modulate the frequencies of the beam so that all higher mode frequencies become odd-integer multiples of the fundamental frequency of the feedback model. Single-mode input shaping techniques are implemented to eliminate vibrations in all modes of the model simultaneously. Input commands to the plant of the feedback system are used as inputs to the base of the physical model. The main advantage of the frequency-modulation input shaping strategy is that only one single-mode input shaper is needed to eliminate vibrations in all modes of the system. Numerical simulations and finite element simulations, using Abaqus-v6.12 FEA package, demonstrate the effectiveness of the proposed strategy.

## 2. Single-Mode Input Shaping

Input shaping is a technique used to eliminate inertia excited vibrations in dynamic systems. A general command signal is convoluted with a sequence of impulses to produce a shaped command that results in zero residual vibrations. Although input shapers have been developed earlier for multimode systems, they are hard to implement due to the large number of fast input impulses involved. Single mode input shapers are easier to implement. Several single input shaping techniques have been developed over the past two decades. The most practical input shapers in the literature are the *Zero-Vibration (ZV)* input shaping, Fig. 1(a), and the robust *Zero-Vibration-Derivative (ZVD)* input shaping [16], Fig. 1(b). This is due to the reduced number of impulses involved.

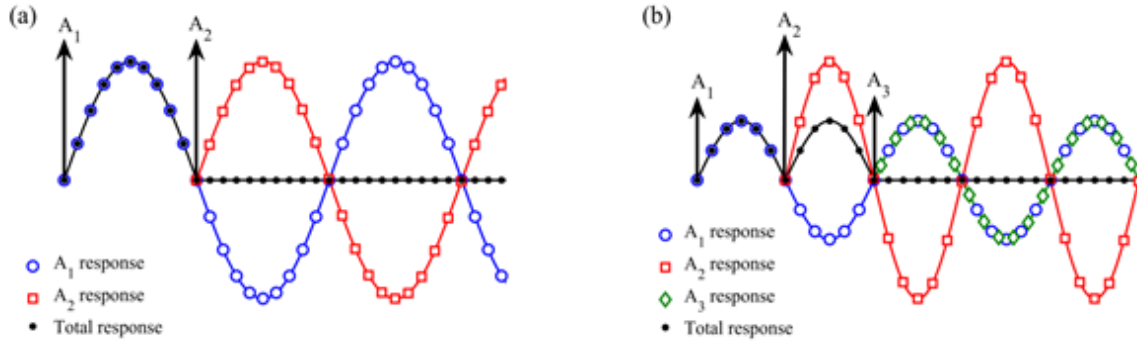


**Figure 1.** (a) Zero-Vibration (ZV) input shaping and (b) Zero-Vibration-Derivative (ZVD) input shaping.

Zero-Vibration input shaping is based on convoluting a general input command with a sequence of two impulses, where the response to the second impulse mitigates the vibration excited by the first impulse. The impulses are separated by half the vibration period of the system. The ZV input shaping matrix is

$$ZV = \begin{bmatrix} A_i \\ t_i \end{bmatrix} = \begin{bmatrix} \frac{1}{K+1} & \frac{K}{K+1} \\ 0 & \frac{\tau_d}{2} \end{bmatrix} \quad (1)$$

where  $A_i$  and  $t_i$  are the  $i^{th}$  impulse amplitude and impulse time, respectively,  $\tau_d$  is the damped period of the system, and

$$K = e^{-\zeta\pi/\sqrt{1-\zeta^2}} \quad (2)$$

where  $\zeta$  is the damping ratio.

The ZVD input shaper includes three timed impulses separated by half the vibration period of the system. The ZVD matrix is

$$ZVD = \begin{bmatrix} A_i \\ t_i \end{bmatrix} = \begin{bmatrix} \frac{1}{1+2K+K^2} & \frac{2K}{1+2K+K^2} & \frac{K^2}{1+2K+K^2} \\ 0 & \frac{\tau_d}{2} & \tau_d \end{bmatrix} \quad (3)$$

The ZV input shaper is a non-robust shaper, but it is the shortest in terms of its time duration. The ZVD input shaper is a robust shaper. The robustness of the ZVD shaper comes at a price of longer shaper duration. It is important here to emphasize that the aim of the proposed FM input shaping strategy is to be able to eliminate all modes of vibration of the system using one single-mode shaper. It is not a goal of the proposed FM input shaping strategy to enhance robustness nor is it a goal to increase the speed of the shaping technique used.

### 3. Multimode Frequency-Modulation Input Shaping

In multimode systems, a shaped command signal that eliminates vibrations of the first mode can eliminate vibrations in other modes provided that the frequencies of those modes are odd-integer multiples of the frequency of the first mode. Frequency-modulation [42, 43] can be used to modulate the frequencies of the system model to the point where the above odd-integer multiples condition is satisfied. In the present work, this task will be performed using model-based feedback strategy. Once the odd-integer multiple frequency condition is satisfied, virtually, any single-mode input shaping technique can be used to produce a shaped motion command for the multimode

system. The command signal to the plant of the feedback system is used to drive the multimode system, Fig. 2.

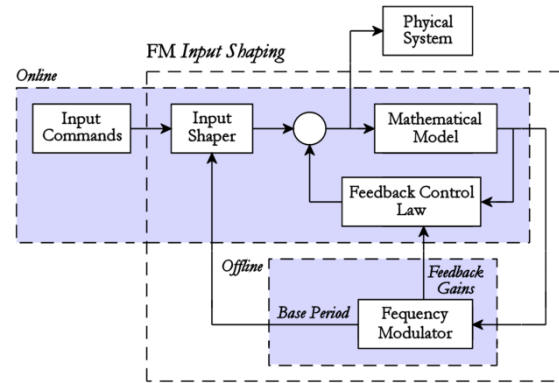


**Figure 2.** Schematic block diagram of frequency-modulation input shaping.

The FM input shaper, consists of two sequential stages; frequency-modulation, then input shaping. In the frequency-modulation stage, model-based feedback is used to satisfy the odd-multiple frequencies condition. The resonant frequencies of model-based feedback system are modulated to the point where all higher modes frequencies become odd-multiples of the first mode frequency. The single-mode input shaper used will be designed using the primary resonant frequency of the feedback model.

The main advantage of the Frequency-Modulation (FM) input shaping strategy is that only one single-mode input shaper is needed to eliminate vibrations in all modes of the system. This reduces the number of impulses involved in shaping process.

### 4. Illustrative Example

The performance of the FM input shaper is demonstrated on a thin hanging beam model of a robotic manipulator, Fig. 3. This type of manipulators is commonly used for pick and place maneuvers. A thin rectangular cross-section is used to magnify the vibration problem. The material of the beam is stainless steel. The material properties and geometric dimensions of the beam are; material density  $\rho = 8030 \text{ kg/m}^3$ , Young's modulus of elasticity  $E = 193 \text{ GPa}$ , beam length  $l = 1 \text{ m}$ , thickness  $h = 0.65 \text{ mm}$ , and width  $w = 26 \text{ mm}$ . The slenderness ratio is  $s = 5330$ . Both numerical and finite-element simulations are used.

#### 4.1. Mathematical Model

Consider a uniform flexible hanging beam, mounted on a horizontally sliding base. To derive the equation of motion for the lateral vibrations of the beam, the kinetic energy is assumed to be entirely due to translation. The governing partial differential equation of motion is [44-46].

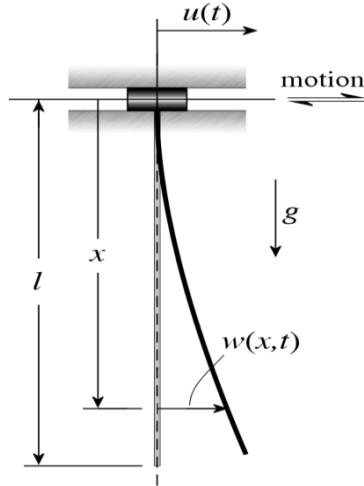


Figure 3. Hanging beam model.

$$EI \frac{\partial^4 w(x,t)}{\partial x^4} + m \frac{\partial^2 w(x,t)}{\partial t^2} - mg \frac{\partial}{\partial x} \left[ (l-x) \frac{\partial w(x,t)}{\partial x} \right] = -m \frac{d^2 u(t)}{dt^2} \quad (4)$$

where  $E$  is the Young's modulus of elasticity,  $I$  is the area moment of inertia of the beam's cross-section,  $m$  is the mass per unit length,  $l$  is the beam length, and  $g$  is the gravitational acceleration. The boundary conditions associated with the given beam support are [47]

$$\left. \begin{aligned} w(x,t) &= 0 \\ \frac{\partial w(x,t)}{\partial x} &= 0 \end{aligned} \right\} x = 0 \quad (5)$$

$$\left. \begin{aligned} \frac{\partial^2 w(x,t)}{\partial x^2} &= 0 \\ \frac{\partial^3 w(x,t)}{\partial x^3} &= 0 \end{aligned} \right\} x = l \quad (6)$$

There is no closed-form solution to the differential equation of motion, Eqs. (4) – (6). However, the given system is a conservation self-adjoint system. We propose to derive an approximate solution in conjunction with Rayleigh-Ritz method. To this end, we assume a separable solution in  $x$  and  $t$  as

$$w(x,t) = \sum_{i=1}^n \phi_i(x) q_i(t) = \Phi^T(x) \mathbf{q}(t) \quad (7)$$

in which  $\Phi(x) = [\phi_1(x), \phi_2(x), \dots, \phi_n(x)]$  is an  $n$ -vector of comparison functions of a complete set and  $\mathbf{q}(t) = [q_1(t), q_2(t), \dots, q_n(t)]$  is an  $n$ -vector of generalized coordinates. We propose to use the eigenfunctions of a cantilever beam in free vibration as comparison functions in this analysis since they satisfy all

the boundary conditions in Eqs. (5) and (6). Those eigenfunctions are

$$\begin{aligned} \phi_i(x) &= \cosh(\beta_i x) - \cos(\beta_i x) \\ &\quad - \frac{\cosh(\beta_i l) + \cos(\beta_i l)}{\sinh(\beta_i l) + \sin(\beta_i l)} [\sinh(\beta_i x) \\ &\quad - \sin(\beta_i x)] \end{aligned} \quad (8)$$

The values of  $\beta_i$  are determined by the characteristic equation

$$\cos(\beta_i l) \cosh(\beta_i l) = -1 \quad (9)$$

Substituting Eq. (7) into the equation of motion Eq. (4), pre-multiplying by  $\Phi(x)$ , and integrating over the whole length of the beam, we obtain the spatially discretized equations of motion

$$M \ddot{\mathbf{q}}(t) + K \mathbf{q}(t) = \mathbf{f} \ddot{u}(t) \quad (10)$$

where

$$\begin{aligned} M &= \int_0^l m \Phi \Phi^T dx \\ K &= \int_0^l \Phi L \Phi^T dx \\ \mathbf{f} &= - \int_0^l m \Phi dx \end{aligned} \quad (11)$$

are the mass and stiffness matrices,  $L$  is the stiffness operator, and  $\mathbf{f}$  is the generalized force vector.

$$L = EI \frac{d^4}{dx^4} - mg \frac{d}{dx} \left[ (l-x) \frac{d}{dx} \right] \quad (12)$$

The natural frequencies can be obtained by solving the eigenvalue problem

$$K \mathbf{p}_i = \lambda_i M \mathbf{p}_i \quad (13)$$

where  $\lambda_i = \omega_i^2$  and  $\mathbf{p}_i$  are the eigenvectors ( $i = 1, 2, \dots, n$ ). The eigenvectors are orthogonal with respect to  $M$  and  $K$  and are normalized to satisfy

$$\begin{aligned} \mathbf{p}_j^T M \mathbf{p}_i &= \delta_{ij}, \quad \mathbf{p}_j^T K \mathbf{p}_i = \lambda_i \delta_{ij}, \\ i, j &= 1, 2, \dots, n \end{aligned} \quad (14)$$

The discretized system of equations of motion Eq. (10) can further be decoupled. We consider a solution in the form

$$\mathbf{q}(t) = P \boldsymbol{\eta}(t) \quad (15)$$

in which  $P = [\mathbf{p}_1, \mathbf{p}_2, \dots, \mathbf{p}_n]$  is a eigenvectors matrix and  $\boldsymbol{\eta}(t)$  is a vector of modal coordinates. Introducing Eq. (15), pre-multiplying by  $P^T$  and using the orthonormality relations, Eq. (14), we obtain the modal equation

$$\ddot{\boldsymbol{\eta}}(t) + \Lambda \boldsymbol{\eta}(t) = \mathbf{b} \ddot{u}(t) \quad (16)$$

where  $\Lambda = \text{diag}(\lambda_1, \lambda_2, \dots, \lambda_n)$  and

$$\mathbf{b} = P^T \mathbf{f} \quad (17)$$

is the modal force vector. Equation (16) represents a system of  $n$ -number of independent equations of motion.

#### 4.2. Frequency Modulation

The resonant frequencies of the model-based feedback system in Fig.2 are modulated to the point where all higher modes frequencies become odd-multiples of the first mode frequency as

$$\tilde{\omega}_i = r_i \omega_1 \quad r_i = 2, 3, \dots, n \quad r_i \in (2N + 1) \quad (18)$$

Either one of the discretized models of the hanging beam in Eqs. (10) and (16) can be used as a model in the feedback system. However, The model in Eq. (10) requires a feedback of the generalized coordinates  $\mathbf{q}(t)$ . The response of any generalized coordinate may include components in all resonant frequencies of the hanging beam. Using such feedback may be undesirable due to its wideband of frequency content. Therefore, we will choose to work with the decoupled discretized model in Eq. (16) since this model gives us control over the frequency content in the feedback signal. Based on the hanging beam model in Eq. (16), a feedback law in the following form is used:

$$\ddot{\mathbf{u}}(t) = \sum_{i=1}^n a_i \ddot{\eta}_i(t) = \mathbf{a}^T \ddot{\boldsymbol{\eta}}(t) \quad (19)$$

where  $\mathbf{a} = [a_1, a_2, \dots, a_{n-1}, 0]^T$  is the feedback gains vector. Note that the highest frequency mode is not included to minimize high frequency content in the feedback signal. Substituting Eq. (19) into Eq. (16) as

$$\ddot{\boldsymbol{\eta}}(t) + \Lambda \boldsymbol{\eta}(t) = \mathbf{b} \mathbf{a}^T \ddot{\boldsymbol{\eta}}(t) \quad (20)$$

the eigenvalue problem becomes

$$|\Lambda - \lambda(I - \mathbf{b} \mathbf{a}^T)| = 0 \quad (21)$$

where  $I$  is the  $(n \times n)$  identity matrix. The modulated frequencies  $\tilde{\omega}_i$  must satisfy the characteristic equation

$$(\lambda - \tilde{\omega}_1^2) \prod_{i=2}^n (\lambda - r_i^2 \tilde{\omega}_1^2) = 0 \quad (22)$$

where  $r_i$  are the odd-integer frequency ratios. Initial selection of the targeted frequency ratios are determined by rounding the exact frequency ratios of the hanging beam model to the nearest odd-integers as

$$r_i = 2 \text{ round} \left[ \frac{1}{2} \left( \frac{\omega_i}{\omega_1} - 1 \right) \right] + 1 \quad (23)$$

$$i = 2, 3, \dots, n \quad \text{where } r_1 = 1.$$

#### 4.3. Numerical Simulations

To validate the performance of the FM input shaping strategy, simulations are performed using a 0.6 m maneuver with the maximum velocity set to 0.3 m/s and a maximum unshaped acceleration of 0.9 m/s<sup>2</sup>. Time-Optimal Rigid-Body (TORB) acceleration command is used as a basic unshaped input command to the FM input shaper. Simulations are performed using both; ZV and ZVD primary input shapers.

Since the energy and mode participation of higher modes is minimal, a three-mode discretized model of the

beam is used, which is a common practice in simulating transverse vibrations of beams. Given the beam properties described above, the inertia and stiffness matrices,  $M$  and  $K$  are

$$M = \begin{bmatrix} 0.1357 & 0 & 0 \\ 0 & 0.1357 & 0 \\ 0 & 0 & 0.1357 \end{bmatrix}$$

$$K = \begin{bmatrix} 3.510 & -0.5620 & -1.427 \\ -0.5620 & 67.26 & 2.515 \\ -1.427 & 2.515 & 470.3 \end{bmatrix}$$

The natural frequencies of the first three modes of the hanging beam, using Eq. (13) are

$$\begin{aligned} \omega_1 &= 5.079 \text{ rad/s} \\ \omega_2 &= 22.26 \text{ rad/s} \\ \omega_3 &= 58.87 \text{ rad/s} \end{aligned} \quad (24)$$

The associated modal matrix is

$$P = \begin{bmatrix} 1.000 & -0.008677 & -0.003064 \\ 0.008696 & 1.000 & 0.006244 \\ 0.003009 & -0.006271 & 1.000 \end{bmatrix} \quad (25)$$

According to Eq. (16), the three decoupled modal equations of motion of the beam are

$$\begin{aligned} \ddot{\boldsymbol{\eta}} + \begin{bmatrix} 25.80 & 0 & 0 \\ 0 & 495.6 & 0 \\ 0 & 0 & 3466 \end{bmatrix} \boldsymbol{\eta} \\ = \begin{bmatrix} -0.7875 \\ -0.4255 \\ -0.2546 \end{bmatrix} \ddot{\mathbf{u}}(t) \end{aligned} \quad (26)$$

Based on the feedback control law of the frequency-modulation stage, Eq. (19), the feedback control law for the three-modes discrete model of the beam is

$$\ddot{\mathbf{u}}(t) = a_1 \ddot{\eta}_1 + a_2 \ddot{\eta}_2 \quad (27)$$

Given the model frequencies Eq. (24), the frequency ratios are  $\omega_2/\omega_1 = 4.383$  and  $\omega_3/\omega_1 = 11.59$ . According to the rounding scheme in Eq. (23), the target modulated frequency ratios are  $r_2 = 5$  and  $r_3 = 11$ . Substituting the control law, Eq. (27), into the characteristic equation (21), and substituting the frequency ratios  $r_i$  into the characteristic equation of the modulated system Eq. (22), and solving both equations simultaneously, the first mode modulated frequency and the feedback gains are

$$\begin{aligned} \tilde{\omega}_1 &= 5.352 \text{ rad/s} \\ a_1 &= -0.1283 \\ a_2 &= -0.6479 \end{aligned} \quad (28)$$

Input shapers are designed for the first mode of the modulated feedback system  $\tilde{\omega}_1$ . Assuming undamped dynamic response, the ZV and ZVD input shapers, Eqs. (1) and (3) are

$$ZV = \begin{bmatrix} 0.5 & 0.5 \\ 0 & 0.5870 \end{bmatrix} \quad (29)$$

$$ZVD = \begin{bmatrix} 0.25 & 0.5 & 0.25 \\ 0 & 0.5870 & 1.174 \end{bmatrix} \quad (30)$$

Modal response of the discrete model in Figs. 4(b) and 5(b) demonstrate successful elimination of vibrations in all

modes of the discrete model using both ZV and ZVD primary input shapers. However, due to the fact that the modulated second-mode frequency is five-times faster than the first-mode, high frequency content is included in the command signal of Eq. (27). This is reflected on the acceleration commands in the form of high command fluctuations in Figs. 4(a) and 5(a).

To overcome this problem, the modulated second mode frequency is brought closer to the modulated first mode frequency by setting the second-mode frequency ratio to  $r_2 = 3$ . The first mode modulated frequency and the control law gains become

$$\begin{aligned} \tilde{\omega}_1 &= 5.352 \text{ rad/s} \\ a_1 &= -0.1198 \\ a_2 &= 1.940 \end{aligned} \tag{31}$$

As expected, maintaining a fixed frequency ratio between the highest and the lowest modes of the system, in this case  $r_3 = 11$ , regardless of the intermediate frequency ratio,  $r_2$ , the modulated first mode frequency remains the same. Only the feedback gains of the control law change. Therefore, input shapers Eqs. (29) and (30) are applicable.

The frequency content and fluctuations in the acceleration commands in Figs. 6(a) and 7(a) dropdown significantly as a result of the lower frequency feedback

command signal. To investigate further possible improvement in the command profile, the second mode frequency is set equal to the first mode frequency by setting the second-mode frequency ratio to  $r_2 = 1$ . The first mode modulated frequency and the control law gains become.

$$\begin{aligned} \tilde{\omega}_1 &= 5.352 \text{ rad/s} \\ a_1 &= -0.01323 \\ a_2 &= 34.29 \end{aligned} \tag{32}$$

Setting the second-mode frequency ratio to  $r_2 = 1$  means that the feedback will have single frequency content, which is the lowest frequency of the modulated system. The effect of this frequency reduction is observed clearly in the much smoother acceleration commands in Figs. 8(a) and 9(a). However, this also means that the modulated system exhibits a double-root at the lowest frequency. The ZV input shaping technique fails in this case, Fig. 8. However, the ZVD input shaping technique continues to perform successfully due to its reduced sensitivity to double-roots in the system, Fig. 9.

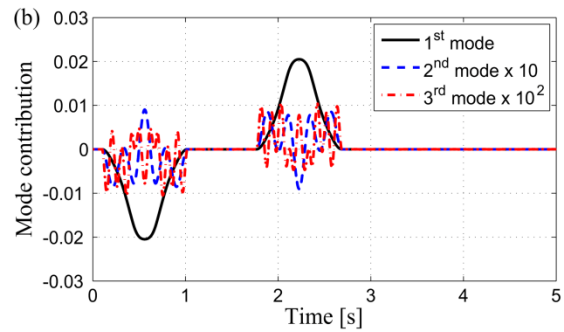
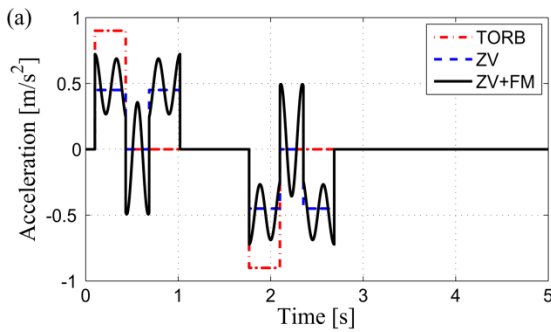


Figure 4. (a) Shaped acceleration and (b) modal response using a ZV primary shaper and a modulated second mode ratio of  $r_2 = 5$ .

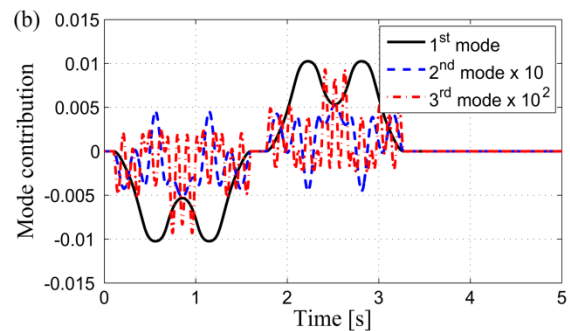
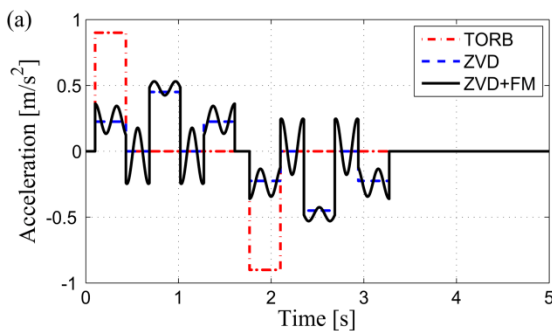
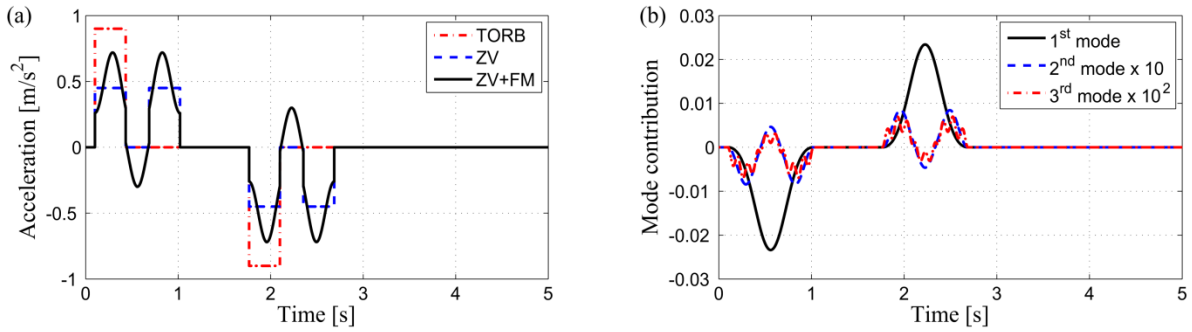
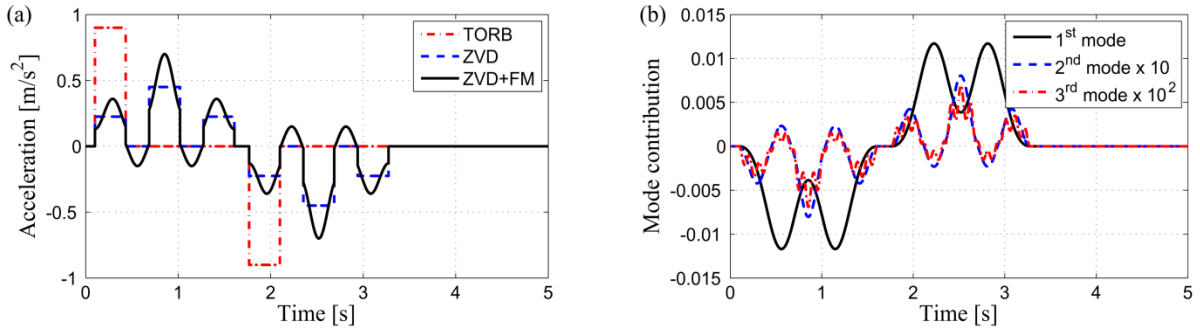


Figure 5. (a) Shaped acceleration and (b) modal response using a ZVD primary shaper and a modulated second mode ratio of  $r_2 = 5$ .



**Figure 6.** (a) Shaped acceleration and (b) modal response using a ZV primary shaper and a modulated second mode ratio of  $r_2 = 3$ .



**Figure 7.** (a) Shaped acceleration and (b) modal response using a ZVD primary shaper and a modulated second mode ratio of  $r_2 = 3$ .

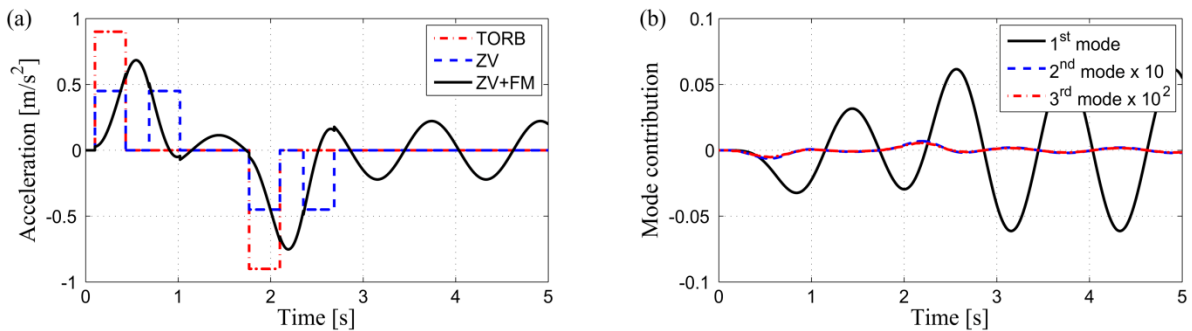


**Figure 8.** (a) Shaped acceleration and (b) modal response using a ZV primary shaper and a modulated second mode ratio of  $r_2 = 1$

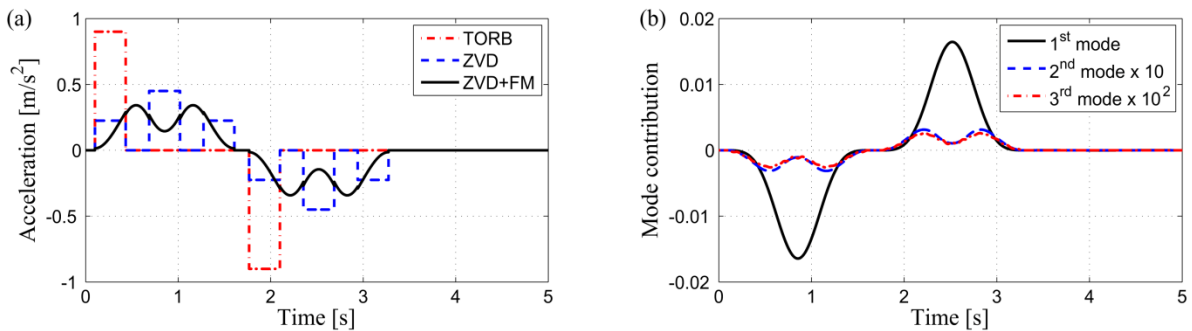


**Figure 9.** (a) Shaped acceleration and (b) modal response using a ZVD primary shaper and a modulated second mode ratio of  $r_2 = 1$ .

#### 4.4. Finite Element Simulations

The finite element analysis simulations are performed using the commercial FEA software Abaqus, version 6.12. The analysis consists of two steps. In the first step, a linear perturbation procedure is performed to calculate the natural frequencies and corresponding mode shapes. In the

second step, a transient modal dynamic linear perturbation analysis that utilizes modal superposition is conducted. Abaqus/Standard implicit integration technique is used in this work. The reason for choosing Abaqus/Standard instead of Abaqus/Explicit is due to its ability to model low speed dynamic events with high accuracy at reasonable computational cost. On the other hand,

Abaqus/Explicit is particularly suitable for high speed dynamic events and applications where severe contact exists such as crash tests.

Two node planar beam elements that use linear interpolation with lumped mass formulation are utilized. The first three modes obtained are in Fig. 10. These elements use Timoshenko beam theory that allows for transverse shear deformation. A mesh convergence study is performed to ensure accurate results with a mesh that is sufficiently dense yet not overly computational expensive. As a result, the beam is modeled using 200 two node planar beam elements.

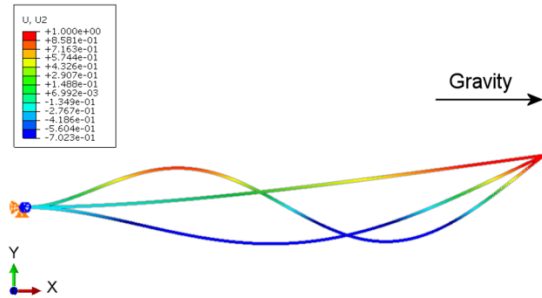


Figure 10. First three modes of the finite element model of a hanging beam

The default eigenvalue extraction method used in Abaqus is the Lanczos method. In this method, a set of Lanczos runs are performed. Each run consists of a number of iterations called steps. In each run, the spectral transformation, which allows rapid convergence to the desired eigenvalues, is applied. Further details about the Lanczos algorithm are available in [48].

The first three frequencies of the FEA model are  $\omega_1 = 5.078$  rad/s,  $\omega_2 = 22.25$  rad/s, and  $\omega_3 = 58.85$  rad/s. These values are in excellent agreement with those obtained using the discretized model Eq. (13).

The simulation cases, performed using the discrete model of the hanging beam, are repeated using the finite element model of the beam. The beam-tip deflection in all cases is shown in Fig. 11. Results in Fig. 11 demonstrate excellent match between the discrete model and the finite element model simulations. The fact that the FM input shaper designed using a three-mode linear approximation of an Euler-Bernoulli beam retains its successful performance on a finite element Timoshenko model of the hanging beam demonstrates a strong robustness of the FM input shaping technique to modeling uncertainties.

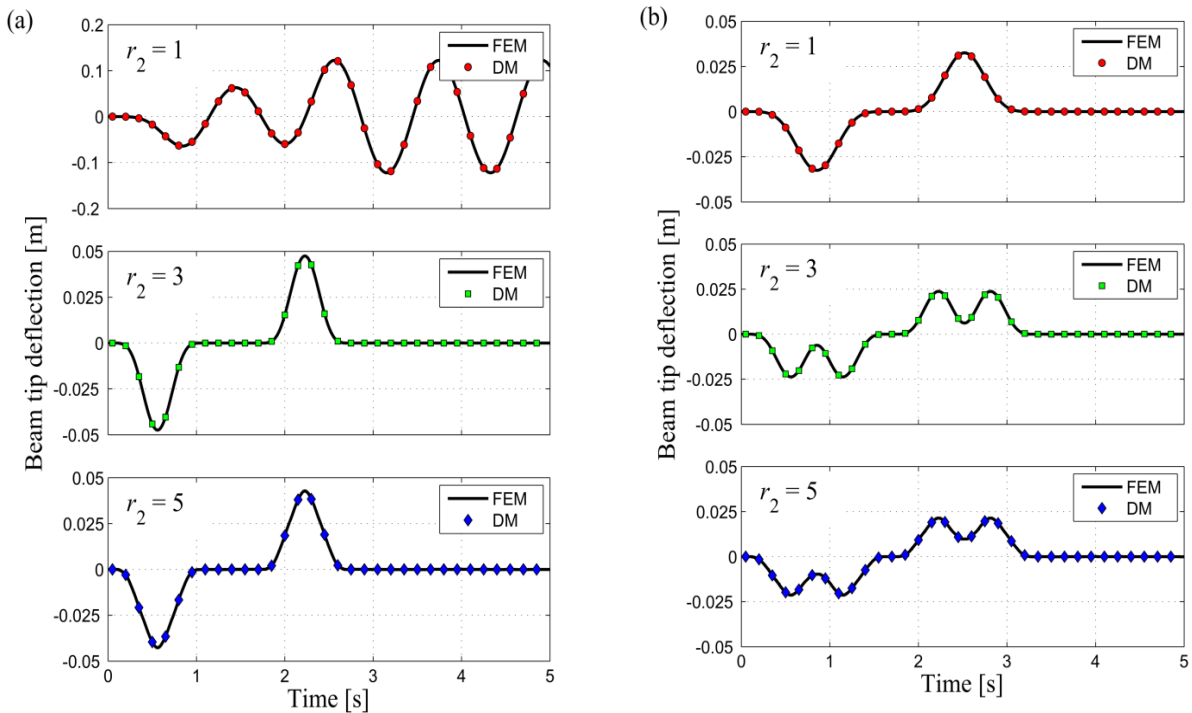


Figure 11. (a) Beam tip deflection of the finite element model (FEM) and the discrete model (DM) using frequency-modulation with (a) a primary ZV shaper and (b) a primary ZVD shaper for different modulated second mode frequency ratios.

## 5. Discussion and Conclusions

Multimode frequency-modulation input shaping is a control strategy developed to overcome one major drawback of multimode input shaping techniques. Multimode convolved input shaping techniques are derived from the convolution of several single-mode input shapers, each targeting a specific frequency. Convolved input shapers intended for high frequencies tend to be impractical due to the high rate of impulses required and the bandwidth limitations on systems' actuators. Inherent time delays in most multimode systems further compromise the performance of those high-frequency input shapers. Simultaneous multimode input shapers tend to be slower, and require high number of shaping impulses depending on the order of the system. These impulses result in practically undesirable jerky input commands.

Multimode FM input shaping strategy uses only one single-mode input shaper designed for the slower first mode frequency of the system. Using a single mode input shaper minimizes the number of impulses involved in the shaping process. Frequency-modulation facilitates eliminating all modes of vibrations of a multimode system simultaneously.

In this frequency-modulation strategy, the selection of the design set of frequency ratios that satisfy the odd-multiple frequencies condition is flexible. The ratios can be selected to meet certain design performance. In the case of the flexible manipulator presented, the design requirement was to reduce shaped input fluctuations, which is a desirable feature in most systems since smoother commands are easier to produce and follow. Smooth commands with minimum fluctuations can be achieved by imposing a double-root condition at the lowest frequency of the modulated system. However, it is imperative that a robust primary input shaping technique is used in conjunction with frequency-modulation.

It is important here to emphasize that the multimode FM input shaping may be implemented using different primary input shapers, and is not limited to the ZV and ZVD input shaping techniques. The proposed strategy is not intended for enhancing performance of input shaping techniques, rather it is intended to reduce the number of input shapers required to eliminate all modes of vibration of the system.

Simulation results show that the performance of the proposed strategy is as effective and as stable as the primary input shaping technique used in conjunction with the FM stage. Results show that the proposed multimode FM input shaping is not vulnerable to modeling uncertainties and omitted nonlinearities. This can be concluded by the excellent match between the simulation results using a linear Euler-Bernoulli model and the results obtained using a Timoshenko finite element model of a hanging beam.

## References

- [1] R.R. Orszulik, J. Shan, "Vibration control using input shaping and adaptive positive position feedback". *J Guidance Control Dyn*, Vol. 34, 2011, 1031-1044.
- [2] Alhazza KA and Alhazza AA, "A review of the vibrations of plates and shells". *The Shock and Vibration Digest*, Vol. 36, 2004, 377-395.
- [3] Benosman M and Vey L, "Control of flexible manipulators: A survey". *Robotica*, Vol. 22, 2004, 535-545.
- [4] Luo B, Huang H, Shan J and Nishimura H, "Active vibration control of flexible manipulator using auto disturbance rejection and input shaping". *Proceedings of the Institution of Mechanical Engineers, Part G: Journal of Aerospace Engineering* Vol. 228, 2014, 1909--1922.
- [5] Lin J and Chao WS, "Vibration Suppression control of beam-cart system with piezoelectric transducers by decomposed parallel adaptive neuro-fuzzy control". *Journal of Vibration and Control*, Vol. 15, No. 12, 2009, 1885-1906.
- [6] Chen KS and Ou KS, "Simulations and experimental investigations on residual vibration suppression of electromagnetically actuated structures using command shaping methods". *Journal of Vibration and Control* 16(11):2010, 1713--1734.
- [7] Sethi V, Franchek MA and Song G, "Active multimodal vibration suppression of a flexible structure with piezoceramic sensor and actuator by using loop shaping". *Journal of Vibration and Control*, 17(13):2011--1994--2006.
- [8] Sasiadek JZ and Srinivasan R, "Dynamic modeling and adaptive control of a single-link flexible manipulator". *Guidance Control Dyn* 12:1989--838--844.
- [9] Jain, S, Peng PY, Tzes A and Khorrami F, "Neural network design with genetic learning for control of a single link flexible manipulator". *Journal of Intelligent and Robotic Systems* 15(2):1996--135--151.
- [10] Hu Q, Shi P and Gao H, "Adaptive variable structure and commanding shaped vibration control of flexible spacecraft". *J Guidance Control Dyn* 30:2007--804--815.
- [11] Singhose W, "Command shaping for flexible systems: A review of the first 50 years". *International Journal of Precision Engineering and Manufacturing* 10(4):2009--153--168.
- [12] Gimpel DJ and Calvert JF, "Signal component control". *Transactions of the American Institute of Electrical Engineers, Part II: Applications and Industry* 71(5):1952--339--343.
- [13] Calvert JF and Gimpel DJ, "Method and apparatus for control of system output response to system input". U.S. Patent no.-2,801,351, 1957.
- [14] Singer NC and Seering WP, "Preshaping command inputs to reduce system vibration". *Journal of Dynamic Systems, Measurement, and Control* 112(1):1990--76--82.
- [15] Singer NC, Seering WP and Pasch KA, "Shaping command inputs to minimize unwanted dynamics". U.S. Patent no.-4,916,635, 1990.
- [16] Vaughan J, Yano A, and Singhose W, "Comparison of robust input shapers". *Journal of Sound and Vibration*, 315(4):~797--815.2008
- [17] Murphy BR and Watanabe I, "Digital shaping filters for reducing machine vibration". *IEEE Transactions on Robotics and Automation* 8(2):~285--289.1992
- [18] Singh T and Heppler GR, "Shaped input control of a system with multiple modes". *Journal of Dynamic Systems, Measurements, and Control*, 115(3):~341--347.1993
- [19] Tuttle T and Seering W, "A zero-placement technique for designing shaped inputs to suppress multiple-mode vibration". *American Control Conference* 3:~2533--2537.1994
- [20] Alam MS and Tokhi MO, "Designing feedforward command shapers with multi-objective genetic optimisation for vibration control of a single-link flexible manipulator". *Engineering Applications of Artificial Intelligence* 21:~229--246.2008
- [21] Hyde M and Seering W, "Using input command pre-shaping to suppress multiple mode vibration". *IEEE International Conference on Robotics and Automation* pp.~2604--2609.1991

- [22] Hyde M and Seering W, "Inhibiting multiple mode vibration in controlled flexible systems". American Control Conference} pp.-2449--2454.1991
- [23] Singhose W, Crain E and Seering W, "Convolved and simultaneous two-mode input shapers". Control Theory and Applications, IEE Proceedings-} 144(6):~515--520.1997
- [24] Singhose WE, Pao LY and Seering WP, "Time-optimal rest-to-rest slewing of multi-mode flexible spacecraft using ZVD robustness constraints". AIAA Guidance, Navigation, and Control Conference}. San Diego, CA, July 1996, Paper no.~96-3845.1996
- [25] Singhose W and Sung Y, "Limited-state commands for systems with two flexible modes". Mechatronics} 19(5):~780--787.2009
- [26] Singhose W, Singer N and Seering W, "Time-optimal negative input shapers". Journal of Dynamic Systems Measurement, and Control} 119(2):~198--205.1997
- [27] Gurleyuk SS, "Optimal unity-magnitude input shaper duration analysis". Archive of Applied Mechanics} 77(1):~63--71.2007
- [28] Masoud ZN, Alhazza KA, Abu-Nada EA and Majeed M, "A hybrid command-shaper for double-pendulum overhead cranes". Journal of Vibration and Control} 20(1):~24--37.2014
- [29] Tokhi M and Poerwanto H, "Control of vibration of flexible manipulators using filtered command inputs". Proceedings of the international congress on sound and vibration} pp.~1019--1026.1996
- [30] Shaheed MH, Tokhi MO, Chipperfield AJ and Azad AKM, "Modelling and open-loop control of a single-link flexible manipulator with genetic algorithms". Journal of Low Frequency Noise, Vibration and Active Control} 20(1):~39--55.2001
- [31] Ahmad SM, Chipperfield AJ and Tokhi MO, "Dynamic modelling and open-loop control of a twin rotor multi-input multi-output system". Proceedings of the Institution of Mechanical Engineers, Part I: Journal of Systems and Control Engineering} 216(6):~477--496.2002
- [32] Ahmad SM, Chipperfield AJ and Tokhi MO, "Dynamic modelling and open-loop control of a two-degree-of-freedom twin-rotor multi-input multi-output system". Proceedings of the Institution of Mechanical Engineers, Part I: Journal of Systems and Control Engineering} 218(6):~451--463.2004
- [33] Mohamed Z and Tokhi MO, "Command shaping techniques for vibration control of a flexible robot manipulator". Mechatronics} 14(1):~69--90.2004
- [34] Rhim S and Book WJ, "Adaptive time-delay command shaping filter for flexible manipulator control". IEEE/ASME Transactions on Mechatronics} 9(4):~619--626.2004
- [35] Alghanim K, Alhazza K and Masoud Z, "Discrete-time command profiles for simultaneous travel and hoist maneuvers of overhead cranes". Journal of Sound and Vibration} 345:~47--57.2015
- [36] Erkorkmaz K and Altintas Y, "High speed CNC system design. Part I: Jerk limited trajectory generation and quintic spline interpolation". International Journal of Machine Tools and Manufacture} 41(9):~1323--1345.2001
- [37] Xie X, Huang J and Liang Z, "Vibration reduction for flexible systems by command smoothing". Mechanical Systems and Signal Processing} 39:~461--470.2013
- [38] Alhazza K and Masoud Z, "A novel wave-form command-shaper for overhead cranes". Journal of Engineering Research } 1(3):~181--209.2013
- [39] Alhazza K, Masoud Z and Alotaibi N, "A smooth wave-form shaped command with flexible maneuvering time: Analysis and experiments". Asian Journal of Control} 18(4):~1--9.2015
- [40] Alhazza K, Masoud Z and Alhazza A, "A multimode wave-form command shaping control applied on a double pendulum". ASME 2015 International Design Engineering Technical Conferences \& Computers and Information in Engineering Conference}, Boston, Massachusetts, 2--5 August 2015, Paper no.~DETC2015-46757.2015
- [41] Alhazza K and Masoud Z, "A multi-mode smooth command shaper with an adjustable maneuver time". ASME 2015 Dynamic Systems and Control Conference}, Columbus, Ohio, 28--30 October 2015, Paper no.~DSCC2015-9700.2015
- [42] Masoud ZN and Alhazza KA, "Frequency-modulation input shaping control of double-pendulum overhead cranes". ASME Journal of Dynamic Systems, Measurement and Control} 136(2):~021005.2014
- [43] Masoud ZN and Alhazza KA, "Frequency-modulation input shaping for multimode systems". Journal of Vibration and Control}~doi:10.1177/1077546314560389.2014
- [44] Li XF, Tang AY and Xi LY, "Vibration of a Rayleigh cantilever beam with axial force and tip mass". Journal of Constructional Steel Research} 80:~15--22.2013
- [45] Hijmissen JW and van Horsen WT, "On transverse vibrations of a vertical Timoshenko beam". Journal of Sound and Vibration} 314(1):~161--179.2003
- [46] Xi L-Y, Li X-F and Tang G-J, "Free vibration of standing and hanging gravity-loaded Rayleigh cantilevers". International Journal of Mechanical Sciences} 66:~233--238.2013
- [47] Meirovitch L, "Principles and techniques of vibrations". Printice Hall} New Jersey.1997
- [48] Grimes RG, Lewis JG and Simon HD, "A shifted block Lanczos algorithm for solving sparse symmetric generalized eigenproblems". SIAM Journal on Matrix Analysis and Applications} 15(1):~228--272.1994

# OPTIMIZATION OF VOLUMETRIC WEAR RATE OF AA7075-TiC METAL MATRIX COMPOSITE BY USING TAGUCHI TECHNIQUE

V.RamakoteswaraRao <sup>\*a</sup>, N.Ramanaiah <sup>b</sup>, M.M.M.Sarcar <sup>c</sup>

<sup>a</sup> Assistant Prof., Mechanical Engineering Dept., R.V.R & J.C College of Engineering (A), Guntur, 522019, India

<sup>b</sup> Professor, Mechanical Engineering Dept., Andhra University College of Engineering, Visakhapatnam, 530003, India

<sup>c</sup> Vice chancellor, JNTUA, Anantapur, 520002, India

Received July, 7, 2016

Accepted August, 23, 2016

## Abstract

Aluminum Metal Matrix Composites (AMMCs), reinforced with particulates, have marked their importance in many engineering applications because of low wear rate and a significant hardness. In the present work, AA7075 metal matrix composite materials, varying in the particle percentage of TiC reinforcement, were prepared by stir casting procedure and optimized volumetric wear at different parameters such as particle percentage of TiC, sliding speed and sliding distance. The specimens were examined Scanning Electron Microscope (SEM). Through Taguchi's technique, a plan of experiment generated and it is used to conduct experiments based on L<sub>27</sub> orthogonal array. The developed ANOVA used to find the optimum wear under the influence of percentage of TiC, sliding speed, sliding distance. In all the cases, matrix material shows a higher volumetric wear rate than composites. 8 wt % of TiC composites show a lower volumetric wear rate (535.58 mm<sup>3</sup>/sec) at minimum sliding distance and maximum sliding velocity of 1Km 2.61m/s, respectively.

© 2016 Jordan Journal of Mechanical and Industrial Engineering. All rights reserved

**Keywords:** AA7075- TiC, Taguchi optimization, metal matrix composites, stir casting, wear.

## 1. Introduction

The permanent and rising demand for lightweight materials in automotive, aerospace, and defense applications has drawn the attention of researchers for improved fuel economy and cleaner emissions. Metal Matrix Composites (MMCs) are suitable for such applications provide good damping properties along with strength, thermal conductivity, and low coefficient of thermal expansion [1-3]. In the field of automobile, MMCs are used for cylinder block, brake drum, and pistons because of improved corrosion resistance and wear resistance [4-5]. MMCs have a stupendous benefit in producing materials with different combinations of stiffness and strength; where in particular, composites are extensively used due to easy fabrication and low cost. Among all, aluminum composites are utilized in many engineering fields because they possess a number of mechanical and physical properties that make them outstanding for automotive applications [6].

Even though MMCs offer superior properties than monolithic materials, they have not been widely applied in structural applications due to the difficulty of fabrication [7]. Fabrication of MMCs has several challenges, such as porosity formation, poor wettability and improper distribution of reinforcement. This can overcome by an attractive processing method for fabrication that is conventional stir casting, as it is moderately inexpensive and offers wide range of materials and processing circumstances. Due to stirring accomplishment of particles into melts, stir casting offers better matrix particle bonding [8]. Bhargavi et al. [9] successfully fabricated composite material through stir casting technique and identified the improved mechanical properties with uniform distribution of reinforced particles.

The quantity, a desired kind and distribution of the reinforcement components, depends on the selection of a suitable process engineering that is the matrix alloy and its application [10]. Thus, reinforcing aluminium with hard ceramic particulates, fibers, or whiskers for the development of Aluminium Metal Matrix Composites (AMMCs) has a series of excellent properties, i.e., high hardness, stability and low density [11]. Among the variety

\* Corresponding author e-mail: vrkrao112880@gmail.com.

of aluminium alloys, Al7075 is quite an accepted choice as a matrix material to prepare metal matrix composites owing to its enhanced formability characteristics and the option of change of the strength of composites through heat treatment [12-14]. A modified stir casting method was engaged to manufacture Al7075 alloy with  $TiB_2$  particles. The molten material, which is in semisolid state at near liquidus was stirred to disperse the particles that were added. It includes three-stage process where finally, the dissolution rate and the growth rate of  $\alpha$ -Al reached equilibrium [15]. A Transmission Electron Microscopy (TEM) study of the electrochemical interactions between constituent particles and the alloy matrix was conducted on 2024-T<sub>3</sub> and 7075-T<sub>6</sub> aluminum alloys to improve understanding particle-induced pitting corrosion in these alloys. By using the stir casting method, Al7075-flyash composite was effectively made-up by adding Mg to improve the wettability of a flyash particle so that these composites could be used in those sectors where low weight and superior mechanical properties are necessary as such as in automobile and space industries [16]. The use of ceramic materials as reinforcement for the matrix Al7075 in various properties can lead to more efficient MMCs, which enhanced mechanical and tribological properties [17]. Al7075 alloy and their composites have been effectively developed through the stir casting based liquid processing route with dispersion of basalt fiber, it significantly improves the hardness, yield strength and the ultimate tensile strength of Al7075 [18]. Aluminium metal matrix composites reinforced with graphite (Gr) and SiC particles fabricated by liquid metallurgy method. It shows that graphite particles are efficient agents in escalating dry sliding wear resistance of Al/SiCp composite [19]. MMCs are having more advantages because of better mechanical properties. The heat treatment specimens were generated hard and unbrittle phases in topcoat due to which an increase in hardness and wear resistance was observed and mass loss has been decreased when compared to untreated substrate [20]. The wear rate of quenched specimen is very low due to the existence of shielding oxide coating layer formed during heat treatment and due to the existence of acicular martensitic structure (retained beta) in its microstructure [21]. Dry Sliding Wear Behavior of Al7075 Reinforced with Titanium Carbide (TiC) was studied in a previous article [22].

Wear is frequently appearing industrial problems, which leads to common replacement of components, mainly abrasion. Abrasive wear occurs when hard particles or asperities penetrate a softer surface, displaces material in the form of elongated chips, and slivers [23]. Wide range of studies on the tribological characteristics of aluminum MMCs containing different reinforcements such as short steel fiber, silicon carbide and alumina are already finished by many researchers [24-26]. The variables, such as interface between the particles and the matrix, composition of the matrix and particle distribution, affect the tribological behavior of metal matrix composites. These conditions consist of the type of environment, contact area, counter surface, applied load, sliding speed, and geometry [27]. The principle tribological parameters, such as applied load [28-30], sliding speed [31-32], and percentage of reinforce particles, control the friction and

wear performance. The greatest development in tribological properties of composite is usually obtained by means of particle reinforcement of silicon carbide and boron carbide. The primary sliding distance require accomplishing mild wear decreased with increasing volume fraction and also wear rate decrease linearly with fraction of volume [33]. Daoud et al. [34] found that adding magnesium alloy to composite during production ensures fine bonding between the matrix and the reinforcement.

Taguchi method is the most useful tool for improving the performance of the product, process, design and system with a significant reduction in experimental time and cost [35]. Abbas et al. [36] established taguchi technique as a valuable technique to deal with responses influenced by multi-variables. It is meant for process optimization and finding of optimal combination of the parameters for a given response. This method significantly reduces the number of experiments that are necessary to model the response function compared with the full factorial design of experiments. This method defines at the lower-the-better, the larger-the-better and the nominal-the-better categories of eminence characteristics in the analysis of Signal/Noise ratio. The most significant advantage of this method is to find out the probable interaction between the factors. AA 6351-T<sub>6</sub> and AA 2024-T<sub>6</sub> alloys were fabricated by using friction stir welding process and applying ANOVA on the experimental investigations.

The influence of parameters, such as weight percentage of reinforcements, normal load, sliding distance and sliding speed on dry sliding wear, was discussed by incorporating an orthogonal array and Analysis of Variance (ANOVA) technique [37]. The percentage of contribution of FSW process levels was used and predicted tensile strength maximum at optimum parameters [38]. Chandrasekhar Rao et al. [39] studied the influence of grain refiners, modifier and refiner on wear - friction behavior of hypereutectic Al-15Si-4Cu cast alloy and reported that it depends on the size, shape and size distribution of  $\alpha$ - aluminum grains and secondary phase particles in the matrix. Uthayakumar et al. [40] employed ANOVA to examine which design parameters considerably affect the wear behavior of the composite.

The present study is intended to look into the effects of sliding distance, sliding velocity and wt. % of reinforcement on volumetric wear rate of AMMCs (AA7075 as matrix material and Titanium Carbide (TiC) particulates as reinforced material on Pin on Disc apparatus and identify the most effective control parameter on reference variable by using Taguchi method. ANOVA was employed to investigate which design parameters significantly affect the wear behavior of the composite.

## Experimental Set-Up

### Materials and Methods

In the present investigation, dry sliding wear tests were performed on TiC particles of size 2 $\mu$ m reinforced Al-7075 alloy matrix composite. The reinforcement percentage varied from 2 to 10 wt. % in steps of 2%. The chemical composition of AA7075 Alloy is shown in Table1.

**Table 1.** Chemical composition of AA7075 matrix material (wt. %)

Si	Fe	Cu	Mn	Mg	Cr	Zn	Ti	Al
0.08	0.24	1.5	0.06	2.4	0.20	5.8	0.07	Balance

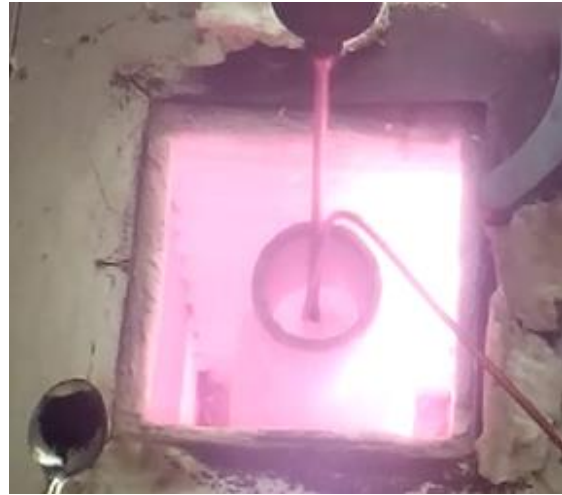
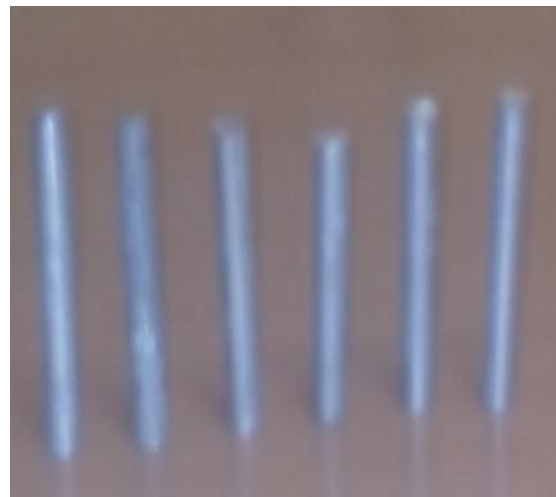
### Fabrication of Composites

In manufacturing MMCs, stir casting technique is one of the popular liquid metallurgy process and is known as a very promising process for manufacturing at a normal cost and this is one of the vortex methods to create a good distribution of the reinforcement material in the matrix. Hence, for the present work, stir casting technique is used to fabricate Al 7075 alloys with varying weight percentages of TiC (2%, 4%, 6%, 8% and 10%) reinforcement. In order to achieve a good binding between the matrix and particulates, magnesium ribbons were added to increase the wettability of melted AA7075 matrix material. The experimental set up is as shown in Fig. 1.

In stir casting, furnace is mounted on the floor and the temperature of the furnace is precisely measured and controlled to achieve a good quality of composite. Two thermocouples and one PID controller are used for this purpose. Mild steel materials preferred as stirrer rod and impeller since they have high temperature stability. The stirrer is coupled to 1 HP DC Motor through flexible link and is used to stir the molten metal in semi-solid state. To bring the stirrer in contact with the composite material screw operator lift is used. The melt is maintained at the temperature of 800°C for one hour and it is stirred thoroughly at a constant speed of 300 rpm for a period of 15 min and the vortex is produced by using a mechanical stirrer. TiC of 2,4,6,8 and 10 wt% with particulates size in range of 2  $\mu\text{m}$ . The molten composite (AA7075/TiC) is poured in the materiallic molds which were preheated to 400°C and then cooled to room temperature and the castings were separated from the materiallic molds as shown in Figure 2. The same procedure followed to get the AMMCs of different weight percentages-4%, 6%, 8% and 10% [41].

### Heat Treatment ( $T_6$ )

The composite gets solidified in a die in the form of a cylindrical bar of diameter 8 mm and length of 30 mm. The solidified composite test sample is removed from the die and machined for required dimensions. The test AA7075 matrix material and AA7075/TiC composites were homogenized at 450°C for 2 hours and then aged at 121°C for 24 hours to  $T_6$  condition. The wear specimens of 30mm length and  $\varnothing$ 8mm were retrieved through wire cut EDM process from the thoroughly homogenized ingots of matrix alloy and composites as shown in Fig. 3 [41].

**Figure 1.** Electric furnace**Figure 2.** Casting specimens**Figure 3.** Wear specimens

## Testing Procedure

Cylindrical samples ( $\varnothing 8\text{mm} \times 30\text{mm}$ ), having flat surface in contact region and rounded corner, were used to conduct wear tests under fixed normal load 20 N, at three sliding velocities (1.57 m/s, 2.09 m/s and 2.61 m/s) and at three sliding distances (1 Km, 2Km and 3Km) on pin-on-disc machine (Model TR-19.62LE supplied by M/s Ducom) in dry condition as per ASTM standards. The pin is detached from the holder and disk was cleaned with acetone to remove wear debris after each test run. The post mechanical tests (Microstructure and SEM analysis) were carried out to study the worn out surfaces under different velocities and distances.

## Calculation

The volumetric wear rate  $W_v$  of the composite was calculated using relate to density ( $\rho$ ), mass loss of the specimen after wear test ( $\Delta m$ ) and the abrading time ( $t$ ) by the following Eq.(1):

$$W_v = \Delta m / \rho t \text{ mm}^3/\text{sec} \quad (1)$$

## Experimental Design

Design-of-Experiments (DoE) requires attentive planning, careful layout of the experiment, and professional analysis of results. Taguchi has standardized methods for each of these DoE application steps. The experiment specifies three principle wear testing conditions including percentage of TiC Particles, sliding distance and sliding velocity as the process parameters. The experiments were carried out to analyze the influence of volumetric sliding wear, specific wear rate and friction coefficient on the MMCs. Control factors and their levels are shown in Table 2. This Table shows that the experimental plan had three levels.

**Table 2.** Levels of the control parameters used in the experiments technique

Control parameters	levels			units
	I	II	III	
Reinforcement	0	8	10	Wt.%
Sliding distance	1	2	3	Km
Sliding velocity	1.57	2.09	2.61	m/s

Total 27 experiments ( $L_{27}$ ) were conducted and the experimental combinations are determined using minitab15 software. The experimental result of volumetric wear rate is collected for each experiment and the same is analyzed to understand the influence of parameters [42].

## Results and Discussion

### Mechanical Properties

Table 3 shows the mechanical properties of AA7075 matrix material and composites at different wt. % of TiC. Previously, an attempt was made for the investigation on the properties of TiC reinforced AA7075 metal matrix composites [41]. It can be observed that hardness and measured density ( $\rho_{MMC} = (m) / ((m-m1) \times \rho_{H_2O})$ ) show an increasing trend with increasing percentage of TiC

particulates. The increase of hardness was observed from 181 VHN for matrix material to 202 VHN at 8 wt% TiC reinforced composite at T6 condition. However, declining of hardness was observed at 10 wt. % TiC composite due to the agglomeration and casting defect. The same trend was observed for tensile strength but significant decrement in percentage of the elongation from 8.341 to 7.14. From these results, it is observed that at wt. % 8 TiC composite shows better mechanical properties than the matrix material and all other composites.

**Table 3.** Mechanical properties of AA7075 matrix and AA7075/TiC composites [41]

Wt. % of Reinforcement	Hardness, VHN	Density, g/cc	Tensile strength, N/mm <sup>2</sup>	% of elongation
AA7075	181.0	2.810	471.3	8.34
AA7075/2 wt.% TiC	188.7	2.820	557.7	8.14
AA7075/4 wt.% TiC	193.0	2.830	563.9	7.86
AA7075/6 wt.% TiC	196.4	2.845	571.2	7.57
AA7075/8 wt.% TiC	202.1	2.853	602.0	7.14
AA7075/10 wt.% TiC	195.1	2.862	587.9	7.37

### Effect of Control Parameters on Volumetric Wear Rate

In Taguchi design, S/N ratio is a measure of robustness used to identify the control factors. The design matrix for three control factors, each at three levels, along with the results of the volumetric wear rates and S/N ratio are presented in Table 4. The effect of each control parameter on the volumetric wear rate can be analyzed with the main effects plot and interaction plot. The S/N ratio is calculated for each level of each parameter and then a plot is generated as show in Fig. 4. The level at which the S/N ratio is higher will give the higher signal for the required response, volumetric wear rate in this case. That particular level of each parameter is taken as the optimal parameter for volumetric wear rate, as per Taguchi optimization. It can be seen from the Fig. 4, that (i) as the wt. % of reinforcement increase, the volumetric wear rate decreases up to level 2(8 wt. %) and then increases slightly to level 3, (ii) as the sliding velocity increases, volumetric wear rate decreases and (iii) as the sliding distance increases, volumetric wear rate increases. It can be observed that the sliding velocity and sliding distance have a significant effect on the volumetric wear rate. The main effects plot (Figure 4) indicates that optimal values of the parameters for minimizing the volumetric wear rate occurred when the wt. % of reinforcement at level 2(8 wt. %), sliding velocity at level 3(2.61 m/s) and Sliding distance at level1 (1 Km). The interaction plot for volumetric wear rate is illustrated in Fig. 5. It is well understood that interactions do not occur when the lines on the interaction plots are parallel and strong interactions occur when the lines cross [43]. An observation of Fig. 5 reveals a small interaction between the test parameters.

**Table 4.** Experimental conditions and machining response

Test number	Wt.% of Reinforcement	Sliding distance, Km	Sliding velocity, m/s	Volumetric wear rate, mm <sup>3</sup> /sec	S/N ratio
	0	1	1.57	1584.34	-63.997
	0	1	2.09	1071.67	-60.6012
	0	1	2.61	815.66	-58.2302
	0	2	1.57	4986.72	-73.9563
	0	2	2.09	3405.69	-70.6441
	0	2	2.61	2446.98	-67.7726
	0	3	1.57	9520	-79.5727
	0	3	2.09	6986.51	-76.8852
	0	3	2.61	4486.12	-73.0374
	8	1	1.57	1070.03	-60.5879
	8	1	2.09	720.43	-57.1519
	<b>8</b>	<b>1</b>	<b>2.61</b>	<b>535.58</b>	<b>-54.5764</b>
	8	2	1.57	3572.04	-71.0583
	8	2	2.09	2348.05	-67.4142
	8	2	2.61	1606.73	-64.1189
	8	3	1.57	6764.49	-76.6047
	8	3	2.09	4018.23	-72.0807
	8	3	2.61	2811.78	-68.9796
	10	1	1.57	1111.11	-60.9151
	10	1	2.09	801.68	-58.08
	10	1	2.61	560.59	-54.9729
	10	2	1.57	3649.83	-71.2455
	10	2	2.09	2608.18	-68.3267
	10	2	2.61	1788.54	-65.05
	10	3	1.57	7077.04	-76.997
	10	3	2.09	4406.15	-72.8812
	10	3	2.61	3163.31	-70.0028

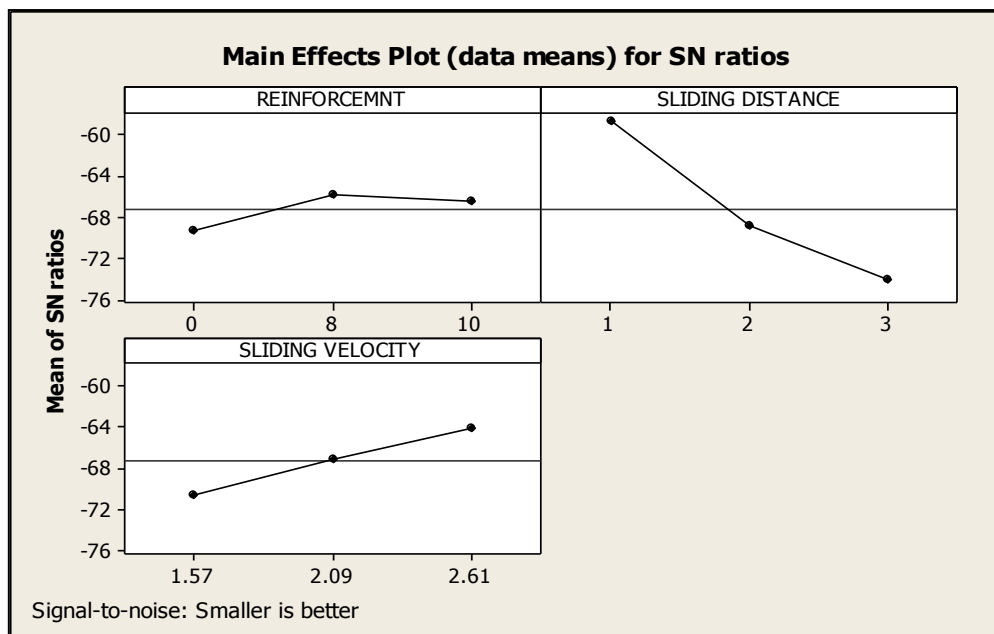


**Figure 4.** Main effects plot for volumetric wear rate of AA7075/TiC composites

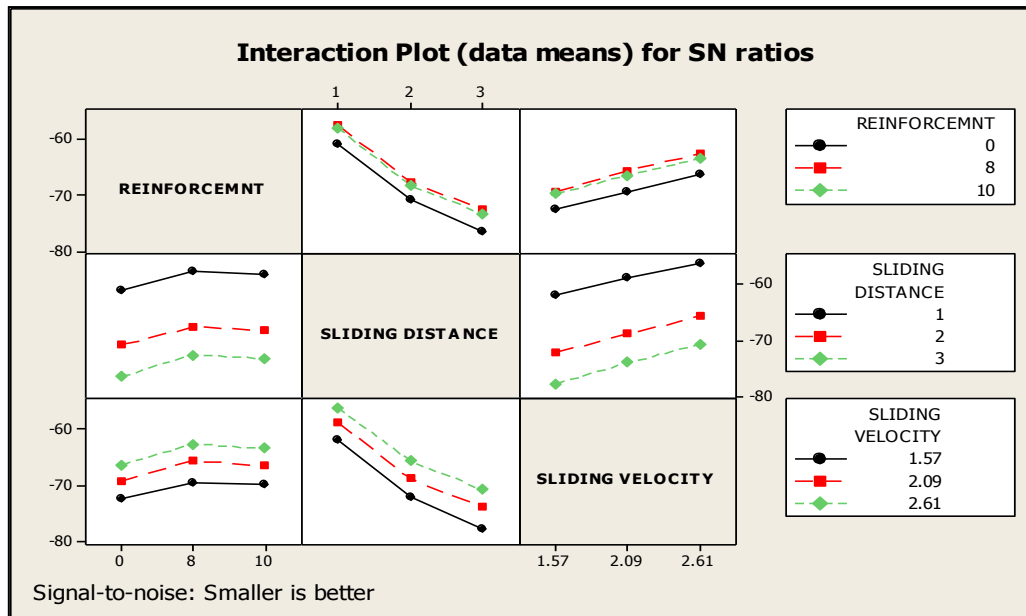


Figure 5. Interaction plot for volumetric wear rate of AA7075/TiC composites

**Statistical Analysis of Variance (ANOVA)**

ANOVA is a statistical technique which can infer some important conclusions based on the analysis of the experimental data. This method is rather useful for revealing the level of the significance of the parameters or their interaction on a particular response [44]. The ANOVA results for means of volumetric wear rate are given in Table 5. It can be observed that the percentage contribution on volumetric wear rate was sliding distance (80.99%) followed by sliding velocity (13.97%) and wt. % of reinforcement (4.82%). From the present analysis, it is also observed that sliding distance is the most influencing parameter for volumetric wear rate of AA7075-TiC particulate composites followed by sliding velocity and wt. % of reinforcement, respectively. The interaction between the sliding velocity and sliding distance (0.076) and wt. % of reinforcement and sliding velocity (0.041) are the significant interaction model terms. The interaction effect between wt. % of reinforcement and sliding distance (0.033) is only nominal.

Table 5. ANOVA table for volumetric wear rate

Source	DOF	Seq SS	Adj SS	Adj MS	F	% C
reinforcement	2	64.98	64.98	32.491	300.53	4.82
Sliding velocity	2	188.37	188.37	94.186	871.18	13.97
Sliding distance	2	1091.18	1091.18	545.590	5046.4	80.982
Wt.% of reinforcement * Sliding velocity	4	0.56	0.56	0.140	1.29	0.041
Wt.% of reinforcement * Sliding distance	4	0.45	0.45	0.113	1.05	0.033
Sliding velocity * Sliding distance	4	1.03	1.03	0.258	2.39	0.076
Error	8	0.86	0.86	0.108		0.063
Total	26	1347.44				100

**Wear Analysis**

Based on the results for AA7075 matrix material, 8 and 10 wt. % of TiC composites under constant load (20 N) conditions, various graphs are plotted and presented in Fig. [6-8]. Fig. 6 shows the variation of volumetric wear rate with wt. % of reinforcement for varying sliding distances (1, 2 and 3Km) at sliding velocity 2.09m/s. It indicates an increasing trend of volumetric wear rate with increasing sliding distance. The volumetric wear rate is higher for AA7075 matrix material than composites due to the increase in the hardness in the composites. During the running period, the volumetric wear rate increased very rapidly with the increasing sliding distance. It is obvious from the Figure that the nature of variation in volumetric wear rate for both the AA7075 matrix material and AMMCs with lead dispersion is similar, irrespective of their compositions. The 8 wt. % of TiC composite enchanting the highest tensile strengths showed the highest wear resistance amongst all. This is in agreement with the laws of adhesive wear and Archard's Equation [44]. It is known that as the tensile strengths of the alloys increase, their volumetric wear rate decreases [45]. In view of the above, the AA7075/8 wt. % would be expected to exhibit the lowest volumetric wear rate.

Figure 7 shows the variation in the volumetric wear rate with respect to the wt. % of reinforcement for varying sliding velocities (1.57 , 2.09 and 2.61 m/s) at sliding distance 1 Km. The result clearly indicates that an increase in the wt. % of reinforcement decreases the volumetric wear rate. The maximum volumetric wear rate is also observed for the unreinforced alloy. It is observed that the volumetric wear rate is low at higher value of sliding velocity due to of at higher velocities the contact plateaus and coefficient of friction are low. So at lower velocities, increased volumetric wear rate is observed.

Figure 8 shows the variation of volumetric wear rate for 8 wt. % TiC composite, having different sliding velocities (1.57, 2.09 and 2.61 m/s) with sliding distances (1, 2 and 3Km). The volumetric wear rate increases with

increasing sliding distance, and it reaches a maximum value at a maximum sliding distance. It depicts clearly that the composite has a lower volumetric wear rate at higher

sliding velocity(2.61 m/s) compared to lower sliding velocity(1.57 m/s).

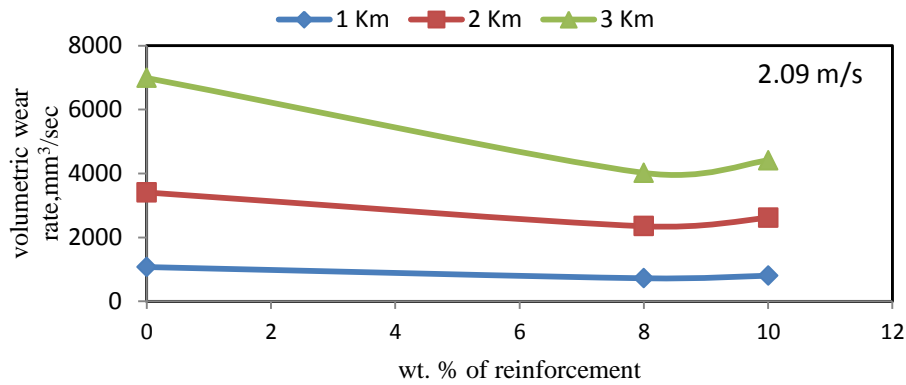


Figure 6. Variation of Vol. wear rate with wt. % of reinforcement at sliding velocity 2.09 m/s

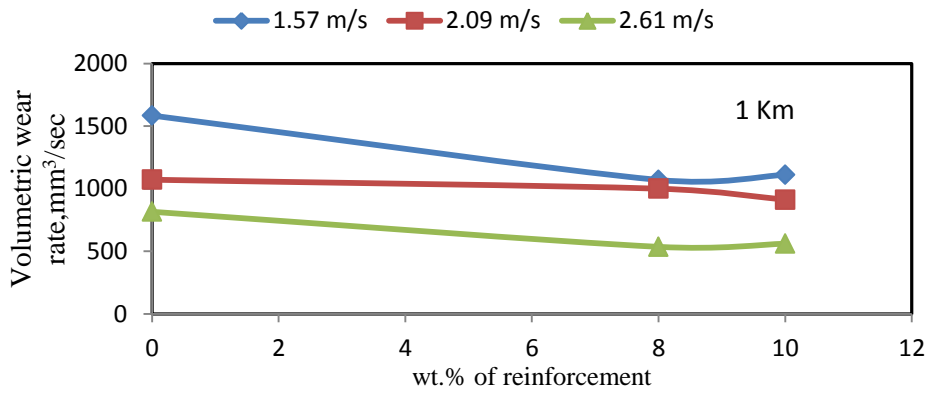


Figure 7. Variation of Vol. wear rate with wt. % of reinforcement at the sliding distance 1Km

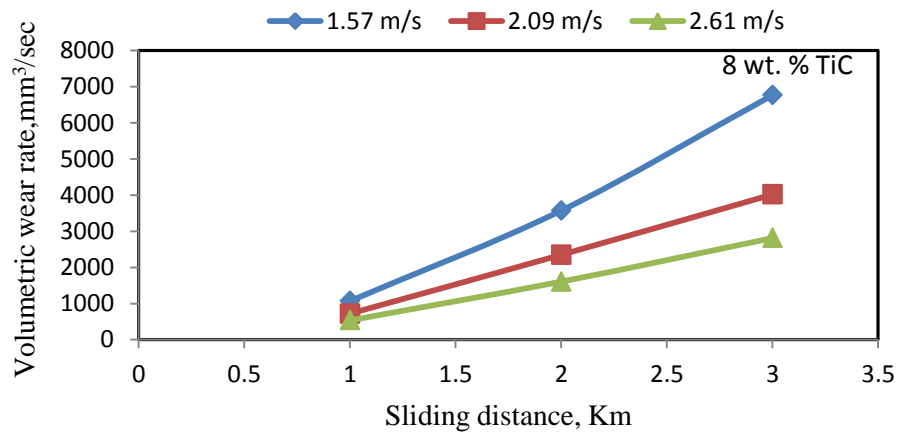
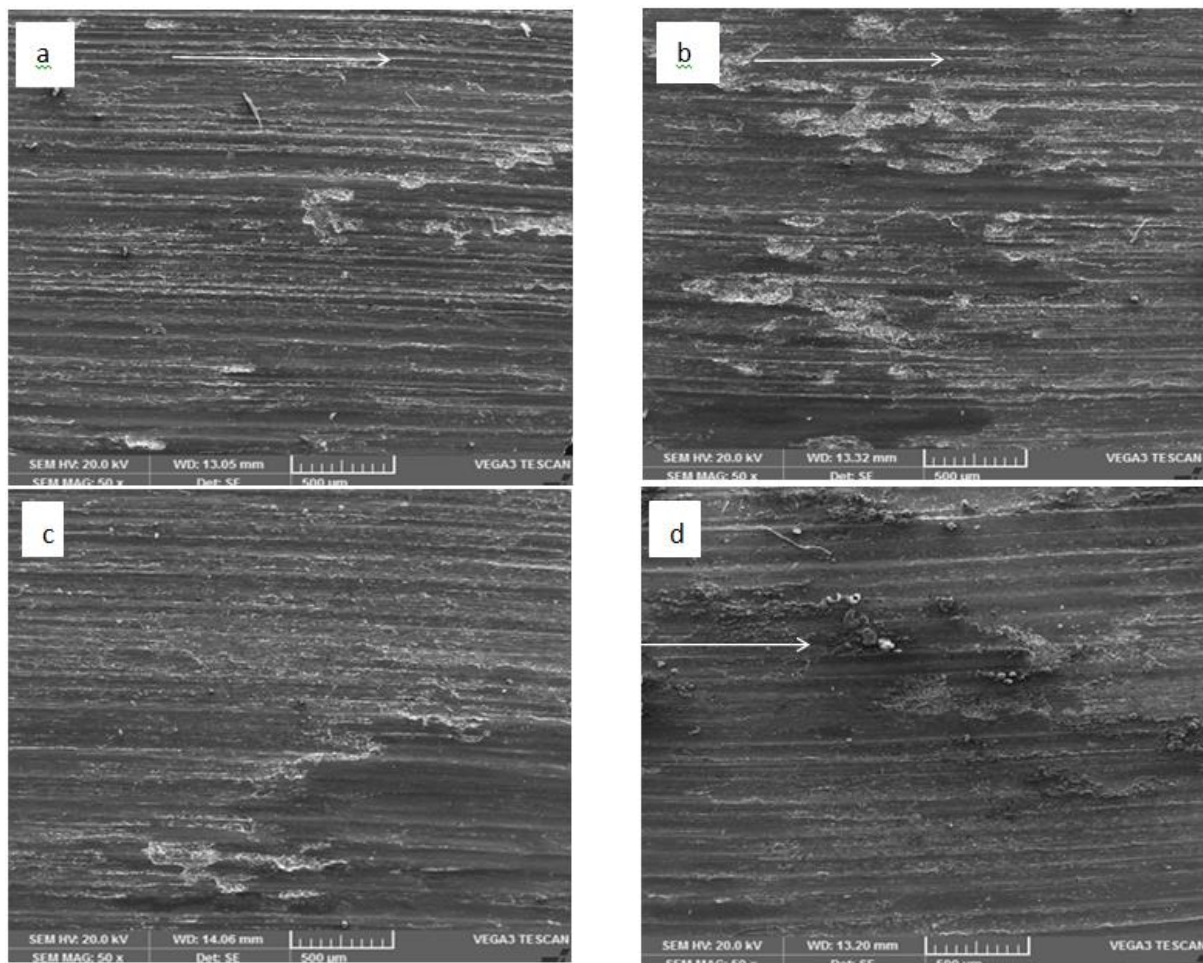


Figure 8. Variation of Volumetric wear rate with sliding distance of 8 wt. % of TiC composite

### SEM Analysis

The examination of the wear surfaces of the AA7075 and AA7075/TiC composites at a presented magnification 50X reveals a well-defined pattern of grooves and scratches running parallel to one another in the sliding direction (indicated by the white arrows) as shown in Fig. 9. It can be seen that the grooves are deeper in the matrix alloy as compared to the composites tested under similar conditions (19.62N, 2.61m/s and 3 Km) due to the absence of hard TiC particles. The examination of wear surface of AA7075 matrix alloy tested at above conditions was characterized by smearing and scratches, a typical characteristic of the sliding wear (Figure 9a) [46]. However, the worn surfaces (Figure 9b-c) reveal that grooves are much shallower in composites than that of the matrix alloy due to the presence of TiC particles. In

addition, it, as evident in Figure 9c, exhibits a comparatively smooth worn surface and grooves are much finer and closely spaced in AA7075/8 wt. percentage TiC particles due to the sliding action of a larger number of hard particles and debris. Due to the increase in TiC particle on the surface of matrix, the plastic deformation of matrix can be resisted with the presence of TiC that acts as a barrier to the moment of dislocation, which causes the more wear resistance than matrix alloy [47]. This clearly indicates that with the improving weight percentage of reinforcement, the hardness of the specimen greatly improves resulting in improving the wear resistance of the reinforced component. Figure 9d shows the worn surface of the AA7075/10 wt. % TiC composite with small cavities visible on the surface. However, a further increase in the reinforcement to 10 wt. % leads to the decrease in the wear resistance.



**Figure 9.** SEM micrographs of worn surfaces at sliding velocity 2.61m/s, sliding distance 3km and normal load 19.62N of (a)AA7075 (b)AA7075+2%TiC (c)AA7075+8%TiC (d)AA7075+10%TiC

### Conclusions

For all heat treatment conditions, AA7075 reinforced with 2µm TiC particle showed better mechanical and tribological properties than those of the AA7075 matrix material and the increased weight percentage of TiC content increased the density, hardness and wear resistance of the composites. The degree of improvement of wear

resistance of AMMC is strongly dependent on the kind of reinforcement as well as on its weight fractions. The volumetric wear rate of AA7075 and AA7075 reinforced with TiC composites increased with increasing sliding distance and decreased with increasing of wt. % of reinforcement and sliding velocity. From the ANOVA table it is seen that the parameter sliding distance is the most significant parameter influencing the volumetric wear

rate, while the other parameters sliding velocity and wt. % of reinforcement are also significant within the specific test range.

## References

- [1] KHW Seah, SC Sharma, PR Rao, BM Girish “Mechanical properties of as-cast and heat-treated ZA-27/silicon carbide particulate composites”. *J. Materials and Design*, Vol.16 (1995) No.5, 277-281.
- [2] Lina M. Shehadeh , Issam S. Jalham, “The Effect of Adding Different Percentages of Manganese (Mn) and Copper (Cu) on the Mechanical Behavior of Aluminum”. *Jordan Journal of Mechanical and Industrial Engineering*, Vol.10 (2016) No. 1, 19-26.
- [3] S.V. Prasad, R. Asthana, “Aluminium-metal matrix composites for automotive applications: tribological considerations”. *Tribology*, vol.17 (2004) No.3, 445-453.
- [4] Shanta Sastry, M. Krishna, Jayagopal Uchil, “A study on damping behaviour of aluminite particulate reinforced ZA-27 alloy metal matrix composites”. *J. of Alloys and Compounds*, Vol.314 (2001) No.1-2, 268-274.
- [5] N. Natarajan, S. Vijayarangan, I. Rajendran, “Fabrication, testing and thermal analysis of metal matrix composite brake drum”. *Internal journal of Vehicle Design*, Vol.44 (2007) No.3-4, 339-359.
- [6] S. V. Prasad, R. Asthana, “Aluminum Metal-Matrix Composites for Automotive Applications”. *Tribology Letters*, Vol. 17(2004) No. 3, 445-453.
- [7] C. Thiagarajan, R. Sivaramakrishnan, S. Somasundaram, “Cylindrical grinding of SiC particles reinforced Aluminum Metal Matrix composites”. *ARPN Journal of Engineering and Applied Sciences*, vol. 6(2011), 14–20.
- [8] K. Kalaiselvan, N. Muruganand, P. Siva, “Prod. and characterization of AA6061–B<sub>4</sub>C stir cast composite”. *Materials and Design*, vol. 32(2011), 4004–4009.
- [9] Rebba Bhargavi, N. Ramanaiah, “Investigations on Mechanical Behaviour of B<sub>4</sub>C and MoS<sub>2</sub> Reinforced AA2024 Hybrid Composites”. *Journal for Manufacturing Science and Production*, DE GRUYTER Publications, vol.15 (2015), 339-344.
- [10] Martin, J. Rodriguez, J. Llorca, “Temperature effects on the wear behavior of particulate reinforced Al-based composites”. *Wear* 225–229 (1999), 615–620.
- [11] S. Basavarajappa, G. Chandramohan, “Dry Sliding Wear Behavior of Material Matrix Composites: A Statistical Approach”. *JMEPEG*, vol.15 (2006), 656-660.
- [12] V. C. Uvarajaa, N. Natarajan, K. Sivakumar, S. Jegadheeswaran, S Sudhakar, “Tribological behavior of heat treated Al 7075 aluminium metal matrix composites”. *Indian Journal of Engineering & Materials Sciences*, Vol. 22 (2015), 51-61.
- [13] Mahagundappa M. Benal, H.K. Shivanand, “Effects of reinforcements content and ageing durations on wear characteristics of Al6061 based hybrid composites”. *Wear* 262(2007), 759–763.
- [14] Ezhil Vannan , Paul Vizhian, “Corrosion Characteristics of Basalt Short Fiber Reinforced with Al-7075 Metal Matrix Composites”. *Jordan journal of mechanical and industrial engineering*, Vol.9 (2015) No.2, 121-128.
- [15] Gui-Sheng Gan, Bin Yang, “Microstructure evolution of TiB<sub>2</sub> particle-reinforced 7075 Al alloy slurry in semisolid state with different holding time”. *Rare materials*, (2015), 1-5.
- [16] Deepak Singla, S.R. Mediratta, “evaluation of mechanical properties of al 7075-fly ash composite material”. *International Journal of Innovative Research in Science, Engineering and Technology*, vol. 2 (2013) No.5, pp.951-959.
- [17] Rajendra .S .K, Ramesha .C .M, “A Survey of Al7075 Aluminium Material Matrix Composites”. *International Journal of Science and Research (IJSR)*, vol.4 (2015) No.2, 1071-1075.
- [18] R. Karthigeyan, “Mechanical Properties and Microstructure Studies of Aluminium (7075) Alloy Matrix Composite Reinforced with Short Basalt Fibre”. *European Journal of Scientific Research*, vol.68 (2012) No.4, 606-615.
- [19] S. Basavarajappaa, G. Chandramohana, J. Paulo Davimb, “Application of Taguchi techniques to study dry sliding wear behaviour of material matrix composites”. *Materials and Design*, vol.28 (2007) No.4, 1393–1398.
- [20] K.Raghu Ram Mohan Reddy, M.M.M.Sarcar, N. Ramanaiah, “Effect of heat treatment on wear behaviour of duplex Coatings on Ti6Al4V”. *Procedia Engineering*, vol.64 (2013), 888 – 895.
- [21] B.K.C.Ganesh, N.Ramanaiah, N.Bhuvaneshwari , S.V.N.Pammi , “Effect of Hank’s Solution and Shot Blasting on the Tribological Behavior of Titanium Implant Alloys”. *International Journal of Materials and Biomaterials Applications*, ISSN 2249–9679, vol.2 (2012) No.1, 5-11.
- [22] V.Ramakoteswara Rao, N.Ramanaiah and M.M.M.Sarcar, “Dry Sliding Wear Behavior of Al7075 Reinforced with Titanium Carbide (TiC) Particulate Composites”. *Proceedings of International Conference on Advances in Materials, Manufacturing and Applications (AMMA 2015)*, Tiruchirappalli, 2015.
- [23] Y. Sahin, K. Özdin, “A model for the abrasive wear behavior of aluminium based composites”. *Materials and Design*, vol. 29(2008) No. 3, 728–733.
- [24] T. Alpas ,J. Zhang, “Effect of SiC particulate reinforcement on the dry sliding wear of aluminium-silicon alloys (A356)”. *Wear*, vol. 155(1992) No. 1, 83–104.
- [25] Ramadan J. Mustafa, “Abrasive Wear of Continuous Fibre Reinforced Al and Al-Alloy Metal Matrix Composites”. *Jordan Journal of Mechanical and Industrial Engineering*, Vol. 4 (2010) No.2, Number 2, 246-255.
- [26] D. Mandal, B. K. Dutta, S. C. Panigrahi, “Dry sliding wear behavior of stir cast aluminium base short steel fiber reinforced composites”. *Journal of Materials Science*, vol. 42(2007) No. 7, 2417–2425.
- [27] P. K. Rohatgi, B. F. Schultz, A. Daoud, W. W. Zhang, “Tribological performance of A206 aluminum alloy containing silica sand particles”. *Tribology International*, vol. 43(2010) No. 1-2, 455–466.
- [28] K. Prasad, S. V. Prasad, A. A. Das, “Abrasion-induced microstructural changes and material removal mechanisms in squeeze-cast aluminium alloy-silicon carbide composites”. *Journal of Materials Science*, vol. 27(1992) No. 16, 4489–4494.
- [29] N. P. Bai, B. S. Ramasesh, M. K. Surappa, “Dry sliding wear of A356-Al-SiCp composites”. *Wear*, vol. 157(1992) No. 2, 295–304.
- [30] K. J. Bhansali, R. Mehrabian, “Abrasive wear of aluminum matrix composites”. *Journal of Metals*, vol. 34(1982) No. 9, 30–34.
- [31] S. Lee, Y. H. Kim, K. S. Han, T. Lim, “Wear behavior of aluminium matrix composite materials”. *Journal of Materials Science*, vol. 27(1992) No. 3, 793–800.
- [32] P. Sannino, H. J. Rack, “Dry sliding wear of discontinuously reinforced aluminum composites: review and discussion”. *Wear*, vol. 189(1995) No. 1-2, 1–19.
- [33] Y. Iwai, H. Yonede, T. Honda, “Sliding Wear Behaviour of SiC Whisker-Reinforced Aluminum Composite”. *Wear*, Vol. 181-183(1995) No. 2, 594-602.
- [34] Daoud, M. T. Abou El-Khair , A. N. Abazim “Microstructure and Wear Behavior development of Squeeze Cast 7075 Al-Al<sub>2</sub>O<sub>3</sub> Particle Composites”. *Proceedings of the 14<sup>th</sup>*

- International Offshore and Polar Engineering Conference, Toulon, 2004.
- [35] Montgomery, D. C. Design and analysis of experiments. 4<sup>th</sup> Edition. NY: John-Wiley & Sons, Inc.; 2006.
- [36] Abbas Al-Refaie, Tai-Hsi Wu, Ming-Hsien Li, "An Effective Approach for Solving The Multi-Response Problem in Taguchi Method". Jordan journal of mechanical and industrial engineering, Vol.4 (2010) No.2, 314-323.
- [37] S.Basavarajappa, G. Chandramohan, "Wear Studies on Metal Matrix Composites: a Taguchi Approach". J. Mater. Sci. Technol., Vol.21 (2005) No.6, 845- 850.
- [38] P. Muralikrishna, N. Ramanaiah, K. Prasadarao, "Optimization of process parameters for friction stir welding of dissimilar aluminum alloys (AA2024 -T<sub>6</sub> and AA6351-T<sub>6</sub>) by using Taguchi method". International journal of industrial engineering computations, vol.4 (2013), 71—80.
- [39] P.V.Chandra Sekhar Rao, A.Satya Devi, K.G.Basava Kumar, "Influence of Melt Treatments on Dry Sliding Wear Behavior of Hypereutectic Al-15Si-4Cu Cast Alloys". Jordan journal of mechanical and industrial engineering, Vol.6 (2012) No.1,55-61.
- [40] M. Uthayakumar, S. Thirumalai Kumaran, S. Aravindan, "Dry Sliding Friction and Wear Studies of Fly Ash Reinforced AA-6351 Metal Matrix Composites". Hindawi Publishing Corporation Advances in Tribology, vol.2013 (2013), 1-7.
- [41] V.RamakoteswaraRao, N.Ramanaiah and M.M.M.Sarcar, "Fabrication and investigation on Properties of TiC reinforced Al7075 material matrix composites", Applied Mechanics and Materials, vol.592-594 (2014), 349-353.
- [42] M. Srinivasa Rao, V. V. S. Bhaskara Raju, T. Subrahmayam, N. Ramanaiah, "Taguchi optimization and effect of Process Parameters on AA5083 Alloy Friction Stir Welds". International Journal of Applied Engineering Research, ISSN 0973-4562, vol.10 (2015) No.24, 21127-30.
- [43] M. Sudheer, Ravi kantha Prabhu, K. Raju, Thirumaleshwara Bhat, "Modeling and Analysis for Wear Performance in Dry Sliding of Epoxy/Glass/PTW Composites Using Full Factorial Techniques". Hindawi Publishing Corporation, ISRN Tribology, (2013), 1-11.
- [44] Shouvik Ghosh, Prasanta Sahoo, Goutam Sutradhar, "Wear Behaviour of Al-SiCp Metal Matrix Composites and Optimization Using Taguchi Method and Grey Relational Analysis". Journal of Minerals and Materials Characterization and Engineering, vol.11 (2012) No.11, 1085-1094.
- [45] Rong Liu, D.Y. Li, "Modification of Archard's equation by taking account of elastic/pseudo elastic properties of materials". Wear, vol.251 (2001) No.1-12, 956-964.
- [46] A.Mandal, B.S. Murty, M. Chakraborty, "Sliding wear behaviour of T<sub>6</sub> treated A356-TiB<sub>2</sub> in-situ composites". Wear, vol.266 (2009) No.7-8, 865-872.
- [47] A.Baradeswaran, ElayaPerumal, "Study on mechanical and wear properties of Al 7075/Al<sub>2</sub>O<sub>3</sub>/graphite hybrid composites". Composites: Part B, vol.56 (2014), 464-471.

# Greenhouse Gas Emissions Reduction Potential of Jordan's Utility Scale Wind and Solar Projects

Nidal Hussein \*

Assistant Professor, Department of Civil Engineering, Isra University, Amman – Jordan

Received Jan., 31, 2015

Accepted May, 24, 2016

## Abstract

Jordan's high reliance on foreign energy sources forced the country to reconsider its energy consumption policies and address the issue of reliance on international energy markets for direct imports. Moreover, renewable energy sources offer important environmental, social and economic benefits. Wind and Solar energy, in particular, carries a very good potential in solving the energy problem in Jordan, diversify its energy supplies and reduces greenhouse gas emissions. This paper focuses on the Green House Gas (GHG) emission reduction associated with the implementation of Jordan energy strategy's solar and wind projects. Four different scenarios were investigated based on the replaced traditional fuel type used for electricity generation that the proposed project will replace. The study shows that the proposed solar and wind project will result in a significant reduction of the country's projected greenhouse gas (GHG) emissions of 1.93 – 3.21 mega tons of CO<sub>2e</sub> annually.

© 2016 Jordan Journal of Mechanical and Industrial Engineering. All rights reserved

**Keywords:** PV, WIND, JORDAN, EMISSION REDUCTION, GHG, CO<sub>2</sub>.

## 1. Introduction

As the world is moving toward more environmentally friendly economies, mainly by depending on cleaner sources of energy associated with fewer negative environmental impacts, renewable energy is attracting a tremendous attention. During the past few years, the cost of the renewable energy has witnessed significant drop and consequently became more competitive. Renewable energy viewed as a significant part of the solution to Jordan complicated energy problems.

Energy considered the major setback to achieving Jordan's goals in terms of social and economic sustainable development. It consumes about 20% of the country's GDP in a country that is currently importing about 96% of its energy needs [1]. Energy price dramatic hike in 2007 was the main drive for energy importing countries, like Jordan, to develop ambitious strategies aiming at securing local sources of energy.

Beside its direct economic benefits and energy security, local renewable energy offers several benefits such as mitigating environmental pollution, providing public health benefits, and creating significant job opportunities that lead to a strong economic growth rate. However, some adverse environmental impacts are associated with the adaptation of renewable energy choices such as land usage and visual distraction of rooftop PV system installation.

Environmental benefits can be amplified by increasing the share of local clean energy specially in countries like Jordan that are blessed with plenty of sunshine of high solar radiation of 5-7 kWh/m<sup>2</sup> per day with over 300 sunny days per year [2]. Etier et al. analyzed the solar radiation in Jordan and found that the majority of Jordan areas receive global radiation of 2080 kW-h/m<sup>2</sup> and more [3]. Figure 1 shows the Global Horizontal Irradiation (GHI) received by Jordan where most of the country receives over 2000 kW-h/m<sup>2</sup> [4]. Jordan also has a good potential for wind energy, with a wind speed ranging between 7.5 to 11.5 m/s in several areas [2]. Such forms of alternative sources of energy help in reducing harmful gaseous emissions associated with energy consumption.

## 2. Jordan's Renewable Energy Sector

Jordan's energy strategy originally targeted an increase of the renewable energy share in its energy mix to a 1000 MW wind projects and a 600 MW solar generation capacity by the year 2020 [1]. In light of the overwhelming progress in implementing the strategy, the county raised its target for solar energy. The Jordanian Minister of Energy has recently announced that the country is expected to commission about 1,800 MW of wind and solar power capacity by 2018, raising the target for solar capacity to 1,000MW by 2020 [5].

\* Corresponding author e-mail: n.hussein@iu.edu.jo.

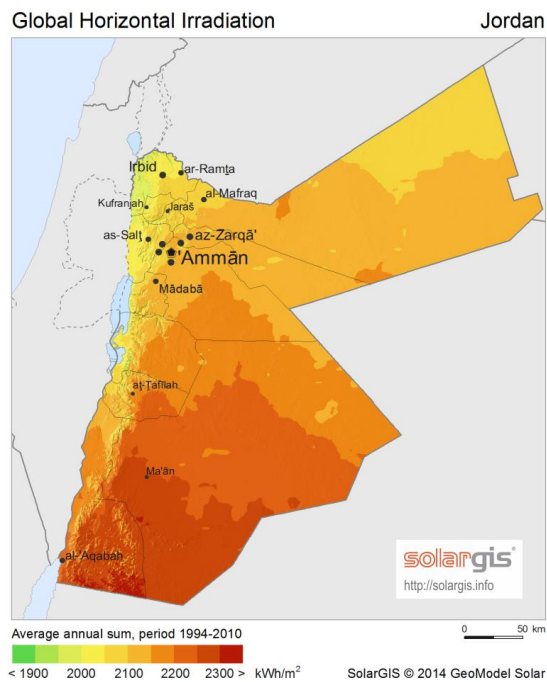


**Figure 1:** Global Horizontal Irradiation (GHI) for Jordan[4]

Consequently, the country currently targets 1000 MW wind projects and a 1000 MW solar generation capacity by the year 2020. Table 1 summarizes the ongoing wind and solar energy projects in Jordan as per the Ministry of Energy and Mineral Resources. These projects are expected to be commissioned and connected to the grid by 2018 [6].

**Table 1:** Ongoing Wind and Solar Energy Projects in Jordan

Project	Technology	Capacity (MW)
Jordan Wind / Tafilah	Wind	117
Ma'an Wind energy	Wind	80
Wind Energy /first phase of Direct Proposals	Wind	585
Al-Fujej	Wind	90
<b>Total wind projects</b>		<b>872</b>
Azraq PV	PV	5.17
First Phase of Direct Proposals (12 projects)	PV	565
Philadelphia / Mafraq	PV	10
Second Phase of Direct Proposals (4 projects) / Mafraq	PV	200
Al Qweirah	PV	103
<b>Total Solar Project</b>		<b>883.17</b>

Jordan has a good experience in utilizing thermal solar energy to provide hot water for Jordanian residences and businesses. Photovoltaic (PV) off-grid systems have been used for water pumping and as a power sources in communications equipment in remote areas of the country. In Jordan, there are about one million square meters of solar heating systems installed in residential and commercial buildings [7]. Renewable energy, in Jordan, offers a strong potential for securing a good source of local energy that covers a high proportion the country's energy

needs. Among the different types of renewable energy, solar and wind energy received a considerable interest in Jordan.

The main challenge that faces a better utilization of renewable energy in Jordan is the lack of appropriate renewable energy infrastructure that is not robust enough to meet Jordan's current energy demands [8]. Previous experience indicates that in order to make renewable energy program successful, the right policy must be adopted nationally with the right incentives to overcome any resistance to such a new technology [9][10][11].

Technical difficulties are expected to rise initially specially when it comes to the readiness of the existing infrastructure to support new renewable energy generation project specially central utility scale projects due to the variability and uncertainty in the output of renewable energy generation [12]. The technical barrier in the case of Jordan is similar to what other countries with similar conditions faced at the beginning of their adoption of a renewable energy generation. In a recent study focusing on the barriers to renewable energy, the technologies adopted in India have been investigated. In that study, which offers an extensive literature review, twenty eight barriers have been identified and categorized into seven dimensions of barriers, i.e., Economic & Financial; Market; Awareness & Information; Technical; Ecological & Geographical; Cultural & Behavioral; and Political & Government Issues [13]. High initial capital cost, lack of financing mechanism and subsidies, lack of consumer awareness to technology, lack of sufficient market base, and lack of local and national infrastructure are examples of priority barriers that will be applicable to renewable energy market in Jordan.

### 3. Governmental Effort to Promote Renewable Energy

By November 2012, the government of Jordan completed the legal framework to encourage electricity users to use solar energy by installing Photo Voltaic (PV) solar system and connect it to the national grid. Electricity exchange with the grid is regulated by the net metering system. The government aims to make the solar energy an important contributor to the country's overall energy needs.

Under electricity net metering system, the customer's electric meter keeps track of how much energy is consumed and how much excess energy is generated by the PV system and sent back into the electric utility grid. Therefore, the customer has to pay only for the net amount of electricity used from the utility over and above the amount of electricity generated by their solar system. Furthermore, the net meter accurately captures energy generated and consumed providing customers with annual performance data.

In parallel with introducing the legal framework of grid connected systems, the government of Jordan has introduced a five-year plan to reform the pricing mechanism that gradually eliminates subsidies and ultimately leads to cost recovery by the end of 2017. The electricity pricing mechanisms divides consumers into activity-based segments such as residential, industrial, service, domestic, etc.; each segment is divided into several blocks according to the monthly electricity consumption in kw-h. The economic feasibility of a

potential PV system in Jordan depends mainly on the price of the electricity produced, which in case of net metering system equivalent to the electricity tariff for a certain segment. Based on a previous study, an increase in electricity price will ultimately raise the interest of consumers to adopt renewable energy solutions, including solar energy [14].

Jordan is currently upgrading its national grid to integrate new mega-size project expected to start operating by 2017. The new grid, being known as the green corridor dedicated for renewable energy project, is expected to be completed by 2017 [1]. During the transitional period, distributed generation scheme can be considered using the existing national grid without the need for major grid upgrades; it also reduces losses due to the distribution over a long distance.

According to the instruction issued by the Electricity Regulatory Commission, the electricity customer can install a PV system that could cover all its average monthly power consumption over a year. Therefore, and in order to decide on the possible and best PV system size, the historical monthly power consumption data are needed.

#### 4. Renewable Energy and Climate Change

With the growing environmental concerns over climate change, clean energy attracted the attention of researchers and policy makers. Traditional fossil fuel consumption is responsible for 56.6% of Green House Gases (GHGs) emissions, widely believed to be the major contributor to global warming [15]. About 28 billion tons of CO<sub>2</sub> are released to the atmosphere annually from burning traditional fossil fuels worldwide [16].

The United Nations (UN) organized Rio de Janeiro's earth summit to address this issue. Few years later, the UN framework Convention on Climate Change was held in Kyoto. Kyoto protocol quantitatively and qualitatively detailed greenhouse gases emission reduction targets. International efforts currently focus on GHG reduction as outlined by the Kyoto Protocol [17].

Jordan ratified the protocol and committed itself to GHG emissions reduction. Recently, during the Paris 2015 UN Climate Change Conference, Jordan's Minister of Environment noted that Jordan was the first country in the region to produce a National Climate Change Policy, under which the Kingdom targets a 14% GHG emissions reduction by 2030 below the Business As Usual (BAU) scenario. The country plans to meet its commitment by implementing 70 projects, mainly in the energy and transportation sectors [18].

#### 5. Green House Gases (GHG) Emission Reduction

Cleaner options of utility scale electricity generation offers environmental benefits that can be evaluated in terms of avoided emissions of GHG compared to business

as usual situation. Although several types of gases are emitted to the atmosphere, the equivalent amount of CO<sub>2</sub> is used to evaluate the environmental impact of each mode of electricity generation per kw-h produced (g CO<sub>2</sub>e/kw-h).

Currently, oil, diesel and natural gas are the most important feedstock used to generate electricity in Jordan. According to the most recent annual statistical bulletin of 2014 issued by Jordan's energy and minerals regulatory commission, 7442, 7177, 3276 GW-h of electricity were generated using oil, diesel, and natural gas, respectively [23]. Therefore, any added capacity coming from a clean source of energy will result in an avoidance of GHG emission compared to the current situation. Three scenarios will be considered where the planned solar and wind utility scale power plant is replacing oil, diesel, or natural gas power plants.

**Table 2:** Lifecycle GHG emissions for the different electricity generation technology

Technology	Greenhouse gas emission (gCO <sub>2</sub> e/kw-h)	Average (gCO <sub>2</sub> e/kw-h)
Oil	733 [19]	733
Natural Gas	499 [19]	456
	469 [20]	
	400 [15]	
Diesel	715 [15]	715
Photovoltaic (PV)	85 [19]	61
	60.1 [21]	
	39 [20]	
Nuclear	29 [19]	48
	66 [22]	
Wind	26 [19]	26

Wind turbines operating in Jordan are expected to produce 3.42 GW-h annually per 1 MW installed capacity [24]. Photovoltaic (PV) solar systems produce 1.86 GW-h annually per 1 MWp installed capacity [25].

As illustrated in Table 1, the total capacity of the ongoing wind project is 872 MW and expected to generate about 2982 GW-h annually. The ongoing solar projects have a total capacity of 883.17 (MW) and expected to generate 1643 GW-h annually. The combined electricity generated from all solar and wind project will total 4625 GW-h annually. This new generation capacity is replacing a need for new power plants that use traditional feedstock of oil, diesel, or natural gas. This alternative approach of electricity generation will help the country in reducing its projected equivalent CO<sub>2</sub> emissions. On average solar and wind energy emits an equivalent of 61 and 26 g CO<sub>2</sub>e/kw-h. For the proposed solar and wind project, the weighted average of 38 g CO<sub>2</sub>e/kw-h. As stated earlier, Jordan generates 7442, 7177, 3276 GH-h of electricity using oil, diesel, and natural gas, respectively. Therefore, the current energy mix emits on average 675 g CO<sub>2</sub>e/kw-h.

**Table 3:** GHG emissions reduction for the different electricity generation technology scenarios

Scenario no.	GHG reduction (gCO <sub>2</sub> e/kw-h)	GHG reduction (MegaTon CO <sub>2</sub> e/yr)
Scenario 1	695	3.21
Scenario 2	677	3.13
Scenario 3	418	1.93
Scenario 4	637	2.95

Three scenarios are investigated based on the replaced traditional feedstock. Scenario 1, 2 and 3 are based on the assumption that the ongoing solar and wind projects are replacing a generation capacity from oil, diesel or natural gas, respectively. The produced electricity by these projects is compensating for electricity that needs to be produced either from oil, diesel or natural gas. A fourth scenario is considered that bases the comparison on the current energy mix in Jordan. In this fourth scenario, the produced electricity by these projects is compensating for electricity that needs to be produced from oil, diesel and natural gas in the same ratio that is used in Jordan for electricity generation. Table 3 summarizes the potential for CO<sub>2</sub>e reduction due to the commissioning of proposed solar and wind projects in Jordan.

The annual CO<sub>2</sub>e reduction due to the implantation of Jordan plans of building and operating several solar and wind power plant appears to be significant. Based on the current energy mix in Jordan (Scenario 4), the implementation of the plan will prevent 2.95 Mega ton of CO<sub>2</sub>e annually.

According to the Department of Horticultural Science at North Carolina State University, on average, a tree can absorb as much as 22 kg of carbon dioxide per year and can sequester 1 ton of carbon dioxide by the time it reaches 40 years old [26]. Therefore, based on the fourth scenario, commissioning the ongoing solar and wind power plant is equivalent to planting and growing a little less than three million tree for 40 years annually.

## 6. Conclusions

In Jordan's ongoing solar and wind utility scale, twenty three projects were investigated in terms of their role in reducing the country's CO<sub>2</sub>e emissions. These projects have a total production capacity of 1755.17 MW. They are expected to be all commissioned and connected to the national grid by 2018. These projects are expected to provide several economic benefits and to have a high potential for creating significant number of good jobs to the country's struggling economy. Moreover, they will help the country meeting its commitment regarding greenhouse gas (GHG) emissions associated with the traditional modes of electricity generation. Four scenarios, based on the replaced traditional feedstock, were analyzed. The analysis shows that upon operation, these projects will prevent 1.93 – 3.21 mega tons of CO<sub>2</sub>e from being emitted to the atmosphere annually.

## References

- [1] Ministry of energy and mineral resources of Jordan, "Updated Master Strategy of Energy Sector in Jordan for the period (2007-2020)". (2007).
- [2] Ministry of Energy and Mineral Resources. Renewable Energy Investing in Jordan Enabling Environment. Franco Jordanian Forum on Renewable Energy, Amman – Jordan, (2014).
- [3] I. Etier, A. Al Tarabsheh, M. Ababneh, "Analysis of Solar Radiation in Jordan". Jordan Journal of Mechanical and Industrial Engineering. Vol. 4 (2010) No. 6, 733 – 738.
- [4] GHI Solar Map © 2014 GeoModel Solar. <http://solargis.info> (accessed March 2, 2016).
- [5] Jordan raises solar capacity target to 1,000MW by 2020. <http://www.thenational.ae/business/energy/jordan-raises-solar-capacity-target-to-1000mw-by-2020> (accessed March 10, 2016)
- [6] Ministry of Energy and Mineral Resources: Renewable Energy Projects. <http://www.memr.gov.jo/Pages/viewpage.aspx?pageID=201> (accessed March. 7th, 2016).
- [7] Al Jayyousi O. Renewable Energy in the Arab World: Transfer of Knowledge and Prospects for Arab Cooperation. 1<sup>st</sup> edition. Amman, Jordan: Friedrich Ebert Stiftung; 2015.
- [8] B. Jerw, M. Dababneh, I. Alahmad, "Photovoltaic Road Lighting Management System:(Amman - Airport) Highway Case Study". 4th Jordan International Conference and Exhibition for Roads and Transport, Amman, Jordan (2014).
- [9] L. Mundaca, J. Luth-Richter, "Assessing 'green energy economy' stimulus packages: Evidence from the U.S. programs targeting renewable energy". Renewable and Sustainable Energy Reviews. Vol. 42 (2015), 1174–1186.
- [10] E. Frederiks, K. Stenner, V. Hobman, "Household energy use: Applying behavioural economics to understand consumer decision-making and behavior. Renewable and Sustainable Energy Reviews". Vol. 41 (2015), 1385–1394.
- [11] D. Elliott, "Renewable energy and sustainable futures", Renewable and Sustainable Energy Reviews, Vol. 32 (2000), 261–274.
- [12] C. Li, H. Shi, Y. Cao, J. Wang, Y. Kuang, Y. Tan, Y. Wei, "Comprehensive review of renewable energy curtailment and avoidance: A specific example in China". Renewable and Sustainable Energy Reviews. Vol. 41 (2015), 1067–1079
- [13] S. Luthra, S. Kumar, D. Garg, A. Haleem, "Barriers to renewable/sustainable energy technologies adoption: Indian perspective". Renewable and Sustainable Energy Reviews. Vol. 41 (2015), 762–776.
- [14] S. Moshiri, "The effects of the energy price reform on households consumption in Iran". Energy Policy. Vol. 79 (2015), 177–188.
- [15] IPCC Second Assessment on Climate Change. International panel on climate change. Cambridge, UK: Cambridge University Press; (1996).
- [16] Wright M, Hearps P, Zero carbon Australia stationary energy plan, Australian Sustainable Energy, Melbourne Energy Institute University of Melbourne, (2010).
- [17] United Nations Framework Convention on Climate Change, "Kyoto Protocol Reference Manual on Accounting of Emissions and Assigned Amount", (2008).
- [18] Paris deal to give momentum to Jordan's efforts to address climate change <http://www.jordantimes.com/news/local/paris-deal-give-momentum-jordans-efforts-address-climate-change#sthash.6XIUeRZW.5SvNgiX6.dpuf> (accessed March 10, 2016).

- [19] World Nuclear Association, "Comparison of Lifecycle Greenhouse Gas Emissions of Various Electricity Generation Sources". London, United Kingdom; (2011).
- [20] P. J. Meier, "Life-Cycle Assessment of Electricity Generation Systems and Applications for Climate Change Policy Analysis". UWFD-1181, Fusion Technology Institute, Madison. (2002).
- [21] G. Hou, H. Sun, Z. Jiang, Z. Pan, Y. Wang, X. Zhang, Y. Zhao, Q. Yao, "Life cycle assessment of grid-connected photovoltaic power generation from crystalline silicon solar modules in China". *Applied Energy*, Vol. 164 (2016), 882–890.
- [22] Sovacool B, "Valuing the greenhouse gas emissions from nuclear power: A critical survey". *Energy Policy*, Vol. 36 (2008), 2950 – 2963.
- [23] Energy and Minerals Regulatory Commission (EMRC), *Annual Statistical Bulletin*. Jordan (2014).
- [24] Cube Engineering, *Tafila Wind Farm: Environmental and Social Impact Assessment (ESIA)*. Jordan; Cube Engineering GmbH (2013).
- [25] Y. El-Tous, "Grid Connected PV System Case Study: Jiza, Jordan" *Modern Applied Science*; Vol.6, (2012) No. 6, 92-98.
- [26] Tree Facts.  
<https://www.ncsu.edu/project/treesofstrength/treefact.htm>  
(accessed March. 10th, 2016).



# Load Characteristics of Pick Cutting Coal Seams with Coal and Rock Interface

Chenxu Luo <sup>a</sup>, Shuangxi JING <sup>a</sup>, Xiaoming HAN <sup>a</sup>, Yu LIU <sup>a</sup>, Changlong Du <sup>b</sup>

<sup>a</sup>School of Mechanical and Power Engineering, Henan Polytechnic University, Jiaozuo 454000, China

<sup>b</sup>School of Mechanical and Electrical Engineering, China University of Mining and Technology, Xuzhou 221116, China

Received July, 11, 2015

Accepted Feb., 15, 2016

## Abstract

A series of experiments of a pick cutting coal seam in different forms were conducted on a cutting testbed of coal and rock. Rotational speeds of the pick and initial velocities of the coal seam in the experiments are uniformly set to be 60 r/min and 0.6 m/min, respectively. Based on the amplitude domain analysis of the cutting force-time signals of the pick cutting rock with different Compressive Strength (CS), it is found that force increment between the pick cutting rock and uniform coal seam linearly increases with the increase of CS difference between fault and coal, and the larger the CS is, the larger the load fluctuation is. Amplitude domain analysis of the signals of the pick cutting coal seam with coal and rock interface at different locations shows that the force increment of the pick cutting the coal seam with coal-rock interface at the center of the coal seam is the largest, compared with those of the pick cutting the coal seam with coal-rock interface at the top and at the bottom, but smaller than the sum of them.

© 2016 Jordan Journal of Mechanical and Industrial Engineering. All rights reserved

**Keywords:** helical vane drum, coal-rock interface, pick, coal seam, cutting load.

## 1. Introduction

With the increasing development of the coal industry and continual improvement of coal science and technology, mining of the special seams, which were difficult to be excavated previously, has been put on the agenda. Especially, excavation of coal seams consisting of coal seam with coal-rock interface, formed from the change of geological structures, has become an important direction of coal mining. Drum shearer, as one of the most important tools in coal mining, has attracted many attentions from researchers both in China and foreign countries. A lot of research work has been done on pick of shearer based on theoretical, experimental and numerical simulation methods. The first model for prediction of the peak cutting force of conical pick was established by Evans based on the maximal tension stress theory [1], then Roxborough *et al.* [2] and Goktan [3] both modified the Evans mathematical model appropriately. According to experimental data from various experiments of cutting different structure rock by conical picks, regression expressions of the relationship between peak cutting force of conical picks and rock CS, tensile strength, dynamic and static modulus of elasticity and brittle index were established. The conclusion was drawn that the cutting performance of the pick is affected mainly by the rock compressive strength, and basic rules governing the relationships between specific energy and chip sizes were

explained [4-7]. Numerical methods were also applied to simulate the rock cutting processes for predicting the peak cutting force in the literature [8, 9]. However, there are some differences between theoretical results of the existing models and the experimental data [10], because the accuracy of the empirical models usually cannot be counted upon due to insufficient experimental data. So a considerable amount of related experiments are necessary and significant. The relationship between Cutting Specific Energy Consumption (CSEC) of the pick and pick geometric parameters was further studied in the present work, on the basis of coal cutting experiments of five drums with different types of picks [11, 12]. Xia *et al.* [13, 14] studied the load characteristics of picks and load distribution using simulation methods. They pointed out that the maximum load of picks follows a normal distribution, which provided a theoretical guidance for the study of stress distribution of picks. Ayhan *et al.* [15] studied the relationship among the CSEC, the respirable dust and the relevant parameters of a pick. Results demonstrated that the CSEC and the respirable dust are correlated with the pick geometry, the pick arrangement, the shearer haulage speed and the drum rotary speed. Mishra [16] studied the influence of pick types on the cutting effect and built the relationship between the heat produced by pick during rock cutting and the cutting parameters.

Duet *et al.* [17] established a drum load fluctuation model to obtain relationships between pick arrangements and drum fluctuating loads, drum rotary speeds and haulage

\* Corresponding author e-mail:

speeds and pointed out that the pick with a punnett square arrangement has a smaller cutting load fluctuation than that of other pick arrangement forms. Li *et al.* [18] analyzed the optimization principle for the pick arrangement, and described the optimized arrangement of checkerboard pick, which as a result laid the foundation for the drum's pick arrangement optimization. Liu *et al.* [19-21] studied the influence of motion parameters and structure parameters of pick on its cutting efficiency, CSEC, vibration characteristics, etc.

A lot of the above-mentioned studies on the load characteristics or cutting performance of pick aimed at uniform coal seams. Under realistic conditions, however, coal seams usually have complicated formation and consist of coal seam with coal-rock interface of different patterns. Relatively, there are few studies on the load characteristics of pick cutting complex-structure coal seams. Liu *et al.* [22] studied experimentally the cutting load characteristics of pick cutting rock of three different structures which are hard-soft-hard rock, soft-hard rock and soft-hard-soft rock, respectively; Ma *et al.* [23] established simulation models of pick cutting complex coal seams, which could predict the influence of different kinds of loads on the pick stress status under different conditions. In the present paper,

therefore, three artificial coal seam each of which contains rock of different CS and three artificial coal seam each of which consists of one or two coal seam with coal-rock interface at different locations were made and experiments of a pick cutting those coal seam were carried out to obtain corresponding cutting force data, then the analysis were conducted to master the cutting load characteristics.

## 2. Introduction of a Test System for Cutting Coal-Rock Seams

Experiments were conducted on a Cutting Testbed of Coal and Rock (CTCR) (shown as Fig. 1), which was described in [19]. The rotary speed  $n$  (r/min) of the pick is within the range of [0, 120]; the velocity of the coal seam  $v_1$  (m/min), which is moving close to the drum along its axial direction, is within [0, 2]; the velocity of the coal seam  $v_2$  (m/min), which is moving along the direction perpendicular to the drum axis, is within [0, 1]. The pick used in the experiment is shown in Fig. (2a) and its motion mode is shown in Fig. (2b), from which it can be seen that half the picks on the pick are cutting coal simultaneously during the pick rotating and going deep into the coal seam. The structural parameters of the pick are listed in Table 1.

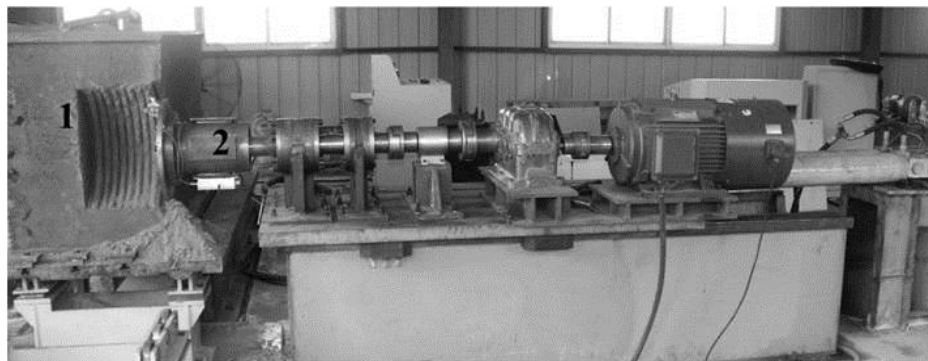
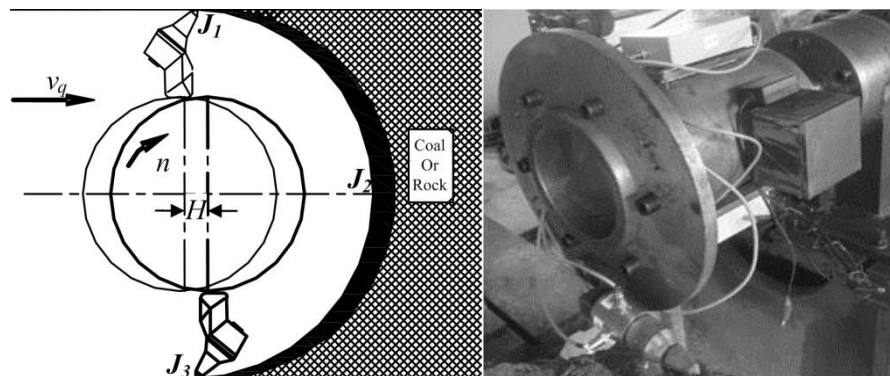


Figure 1. A cutting testbed of coal and rock: 1 and 2 indicate a coal seam and a helical vane drum, respectively.



a) b)

Figure 2. A pick used in the experiments:

(a) a photograph of the pick and (b) a schematic of the pick cutting coal seam process

Table 1. Structure parameters of the pick

Parameter	Diameter $D$ (mm)	Vane number $n$ (-)	Helical angle $e$ ( $^{\circ}$ )	Pick impact angle $a$ ( $^{\circ}$ )	Cutting line space $t$ (mm)
Value	560	2	75	25	30

The process of a shearer pick cutting seams containing coal and coal seam with coal-rock interface is very complicated, especially when the pick is encountering the coal-minor fault interface. At that moment, the pick will transit its status from only cutting coal to cutting rock suddenly. Due to the fact that coal and rock are different in physical properties, such as hardness and CS, large load fluctuations of the pick will occur in this situation, which can affect the cutting performance and reliability of the shearer. So, in order to study the load characteristics of pick cutting complex coal seams, in the experiments, coal seam in different forms (see Fig. 3) were made. Fig. (3a) shows a coal-fault seam, which means that the pick will pass through the coal seam, the coal-fault interface and finally the minor fault. Fig. (3b) shows coal seams consisting of coal seam with coal-rock interface at top and bottom, respectively. In this case, pick will cut coal and coal seam with coal-rock interface simultaneously. Homogeneous coal seams and coal seam with coal-rock interface with different CS are made with different ratios of coal and cement, according to the method of manufacturing artificial rock seams in [19].

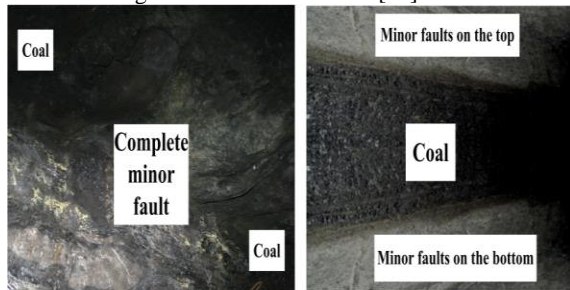


**Figure 3.** Coal seams consisting of different coal seam with coal-rock interface: (a) complete minor fault; (b) coal seam with coal-rock interface on the top and bottom.

### 3. Experimental Study on Pick Cutting Coal-Fault Seams

#### 3.1. Cutting tests of coal seams and rock seams with different CS

To study the cutting force characteristics of the pick when cutting the homogeneous coal seams and rock seams, five experiments were conducted for the three types of homogeneous coal seam with different CS, which are 0.69 MPa, 1.58 MPa, 2.73 MPa and two type of homogeneous rock seam with different CS, which are 4.55 MPa and 8.71 MPa, respectively. The rotational speeds of the pick in the five experiments are uniformly set to 60 r/min and the initial velocities of the coal seam are all set to 0.6 m/min.

The cutting force-time signals for the five different

conditions are shown in Fig. 4. The data are analyzed statistically and the results are listed in Table 2. It can be seen that all the curves show a trend of fluctuation around zero at Stage 1 ( $J_3 \sim J_1$ ), then as the  $h$  rising, the cutting force rising continuously at Stage 2 ( $J_1 \sim J_2$ ) and finally fluctuating around a higher level at  $J_2$ , then reducing continuously at Stage 3 ( $J_2 \sim J_3$ ). As the CS of rock is higher than that of the homogeneous coal seam, the force value waves around 800 N. The relationship between force increment and CS increment is shown in Table 2. It can be seen from the experimental value and the expression for the fitting value that the force increment linearly increases with the increase of CS difference between rock and coal seam.

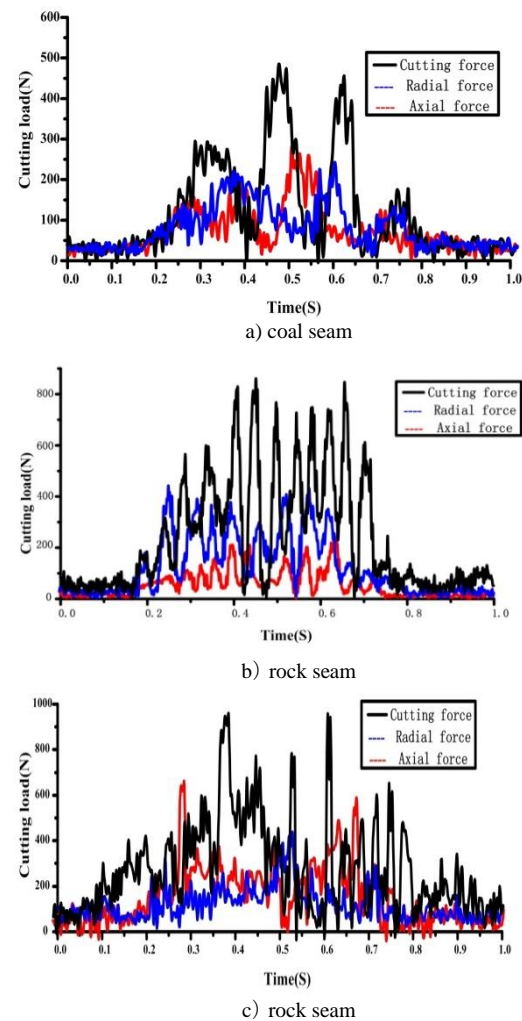


**Figure 4.** Cutting force v.s. time curves for pick cutting coal or rock seam of the form in Fig. 4 with different CS: (a) coal seam 2.73 MPa, (b) rock seam 4.55 MPa, (c) rock seam 8.71 MPa

**Table 2.** Cutting load statistics for different compressive strength coal and rock

	Mean cutting force	Mean peakcutting force	Standard deviation	Mean radial force	Mean peakradial force	Standard deviation	Mean axialforce	Mean peakaxial force	Standard deviation
Coal 0.69 MPa	194.55	475	16.80	51.44	247	16.55	61.2356	235.3821	11.41
Coal 1.58 MPa	217.34	490	17.83	57.50	257.8	15.28	74.8175	253.6794	13.64
Coal 2.73 MPa	229.01	515	17.13	65.83	269.2	16.98	88.2838	281.1141	14.15
Rock 4.55 MPa	324.55	855	19.84	151.24	537.08	16.53	158.059	509.693	15.76
Rock 8.71 MPa	367.34	890	15.59	187.31	557	18.66	212.3393	549.928	14.55

### 3.2. Cutting tests of minor fault at different location of coal seam with coal-rock interface

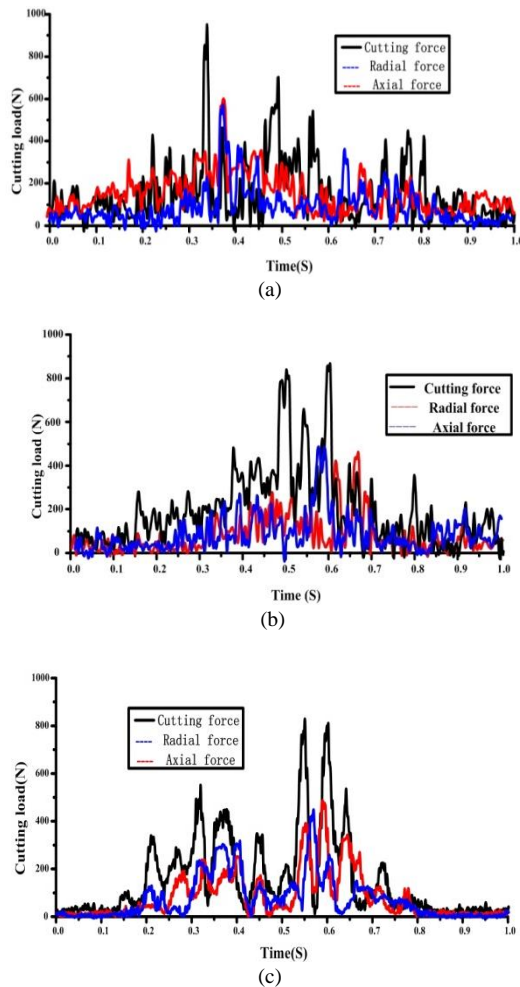


**Fig. 5.** Cutting force v.s. time curves for pick cutting coal seam of the form in Fig. (3a) with coal-rock interface of different location: (a) top, (b) center, (c) bottom

Fig. 5 shows the cutting force for the pick cutting coal seam containing rock of different CS. Obviously, cutting force for Stage 1 and 3 approximately follow normal distributions. In Fig. 5, Stage 2 has two peaks, force values are in a larger fluctuation range. Fig. 5 shows cutting force for pick cutting coal seam containing coal seam with coal and rock interface at different locations. It is not hard to be seen that cutting force for the Stage 1 and 3 follow approximate normal distributions; probability density

distribution in Stage 2 is scattered, that is, force values for Stage 2 are in larger fluctuation range, which means that the pick will suffer a more serious problem. The force value corresponding to cutting force peak of Stage 3 in Fig. 5 is the largest.

As shown in the load above in the cutting process of coal and coal seam with coal-rock interface cutting load, cutting load is gradually increasing with the time, this process is the corresponding cut pick cut into the seam, due to the cutting thickness increasing with time until the cutting pick rotation at the horizontal position with rotary center (maximum cutting thickness), so the pick load will slowly increase in this stage, the cutting load variation is consistent with cutting load variation in homogeneous coal seam. As pick cutting into the cutting rock of coal seam, the load suddenly drops, produce the process, load reduction is due to the cutting pick cut into the rock of coal seam, the compressive strength of coal seam is less than the rock, cutting pick to crush coal load is small, but the rock strata are not affected by the cutting pick cutting coal seam. As pick cutting from the phase transition to the coal rock, the process due to the compressive strength of coal seam is less than the rock, in the process of rock broken, coal seam have been damaged, so load is lower than before. As pick cutting once again return to coal cutting stage, but because of this stage pick rotation direction and the direction of feed for the obtuse Angle, cutting thickness is reduced, so the load evenly reduceing. the axial and radial force change trend are similar with the cutting force.

The cutting force-time signals under three different conditions are shown in Fig. 5. The data were analysed statistically and the results are listed in Table 3. It can be seen in terms of mean and standard deviation that the cutting force and its fluctuation of the pick cutting the minor fault at its top are lower than those of the pick cutting minor fault at its bottom. Due to the existence of the haulage speed  $v_2$ , the line speed of a pick at the top of the pick is larger than that at the bottom when the pick is rotating, so the transient cutting thickness at the top is smaller. As a result, the cutting force of the pick cutting the minor fault at its top is smaller. It can also be found in Table 3 that the cutting force of the pick cutting coal seam with coal-rock interface at its center simultaneously is the largest, but the force increment in this case is larger than the sum of the force increments in the other two cases. Seen from the Table 3, we can see that the cutting force changes as the different location of coal seam with coal-rock interface. And the cutting load of the center location is larger than the other locations, as the center has the biggest thick of coal-rock interface.

**Table 3.** Cutting load statistics for different location of coal seam with coal-rock interface

Coal seam form	Mean force (N·m)	Mean peak force(N·m)	Standard deviation	Mean force (N·m)	Mean peak Force (N·m)	Standard deviation
Top	326.41	779.126	16.92	182.27	490.45	16.92
Center	437.1	865.267	15.37	219.04	522.79	15.37
bottom	414.18	788.127	14.32	191.08	510.84	14.32

### 3.3. Cutting tests of different compressive strength coal seam with coal-rock interface

To study the cutting force characteristics of the pick when cutting the complete coal-minor fault seams, three experiments were conducted for the twotypes of coal seam in Fig. (3a), consisting of coal seam with coal-rock interface with different CS, which are 4.55Mpa and 8.71Mpa, respectively. The homogeneous coal seams have aCS of 0.69 MPa. The rotational speeds of the pick in the five experiments are uniformly set to 60 r/min. The initial velocities of the coal seam are all set to 0.6 m/min.

The cutting force-time signals for the three different compressive strength are shown in Fig. (5b). The data are analyzed statistically and the results are listed in Table 4. It can be seen that all the curves show a trend of fluctuation around a lower level at Stage 1, then rising continuously at Stage 2 and finally fluctuating around a higher level at Stage 3. As the CS of minor fault is higher than that of the homogeneous coal seam, the force value waves around 200N when half the picks on the pick are cutting the uniform coal seam simultaneously. The force will not begin to rise until the pick comes across the coal seam with coal-rock interface. The force value is increasing as the pick going deep into the fault when the number of picks cutting the minor fault at the same time is from one to half the total pick number. After that, The resistance soars when picks turn to cut the minor fault. With the proceeding of the pick cutting the minor fault, the force value keeps rising until the pick completely enters it, and the force value stays fluctuating around the high level. The higher the difference of CS between coal seam with coal-rock interface and coal seam is, the longer it takes the force to come to the high level, which indicates that haulage speed  $v_2$  gets smaller when pick cutting harder rock. Combined with Table 4, it can be observed that the higher the CS of the coal seam with coal-rock interface is than that of the uniform coal seam, and the larger the fluctuation of the force at Stage 3 is, and the larger the increments of cutting forces at Stage 3 and at Stage 1 are.

The relationship between force increment and CS increment is shown in Table 4. It can be seen from the experimental curve and the expression for the fitting curve that the force increment linearly increases with the increase of CS difference between minor fault and coal seam. So when designing pick used for cutting coal seams consisting of coal seam with coal-rock interface, not only the cutting power should be increased, but the impact on

the pick caused by a sudden rise of the cutting force should also be taken into consideration. Based on the relationship between the cutting force increment and the CS increment, strength of transmissiongears in the rocker arm could be enhanced appropriately to improve both stability and reliability.

So when designing pick used for cutting coal seams consisting of coal seam with coal-rock interface, not only the cutting power should be increased, but the impact on the pick caused by a sudden rise of the cutting force should also be taken into consideration. Based on the relationship between the cutting force increment and the CS increment, strength of transmissiongears in the rocker arm could be enhanced appropriately to improve both stability and reliability.

## 4. Conclusions

Experiments of a pick cutting coal seam of different forms were conducted on a cuttingtestbed of coal and rock. The rotational speeds of the pick inthe experiments are uniformly set to 100r/min and the initial velocities of the coal seam are all set to 1.5 m/min. Analysis on the cutting force-time signals of the pick cutting rock of different CS shows that force increment between the pick cutting rock and uniform coal linearly increases with the increment of CS difference between coal seam with coal and rock interface. Analysis on the signals of the pick cutting coal seam with coal and rock interface at different locations shows that the force increment of the pick cutting the coal seam with coal-rock interface at the top and bottom simultaneously of the coal seam is larger than the respectively top and bottom case, but smaller than the sum of the two. All the force-time curves show a trend of fluctuation around a lower level when the pick only cuts uniform coal-seam, rising continuously when cutting coal seam with coal-rock interface and finally fluctuating around a higher level when cutting coal seam with coal-rock interface steadily.

## Acknowledgements

The authors are grateful for the funding of this work by the Henan province education department applied research project fund(16A460005) and Henan Polytechnic University doctor research project fund (660407/020) and China Postdoctoral Science Foundation Funded Project (Project No. 2016M592289).

**Table 4.** Cutting load statistics for different compressive strength coal seam with coal-rock interface

	Mean cutting force( Coal)	Mean cutting force( Rock )	force increment	Mean radial force( Coal)	Mean radial force( Rock )	force increment
Coal 1- Rock 1	194.55	375	180.45	51.44	160.2	108.76
Coal 2- Rock 1	229.01	390	160.99	57.5	157.8	100.3
Coal 3- Rock 1	244.55	415	170.45	65.83	147	81.17
Coal 1- Rock 2	207.34	485	277.66	54.24	281.11	226.87
Coal 2- Rock 2	224.81	496	271.19	56.31	257	200.69
Coal 3- Rock 2	267.34	513.67	246.33	68.28	237.08	168.8

## References

- [1] Evans, "A theory of the picks cutting force for point-attack". *International Journal of Mining Engineering*, Vol. 2(1984) Issue 1, 63-71.
- [2] Roxborough F.F, Liu Z.C. "Theoretical considerations on pick shape in rock and coal cutting". *Proceedings of sixth underground operator conference, Australia*, Vol. 1(1995), 189-193.
- [3] Goktan R.M. "A suggested improvement on Evans's cutting theory for conical bits". *Proceedings of fourth symposium on mine mechanization automation*, Vol. 1 (1997), 57-61.
- [4] C.X. Luo, H.X. Jiang, "Experimental study on the axial force of shearer drum cutting coal and rock". *Recent Patents on Mechanical Engineering*, Vol. 8 (2015) No. 1, 268-234.
- [5] N. Bilgin, M. A. Demircin, "Dominant rock properties affecting the performance of conical picks and the comparison of some experimental and theoretical results". *International Journal of Mining Engineering*, Vol.43 (2006) Issue 1, 139-156.
- [6] C. Balci, N. Bilgin, "Correlative study of linear small and full-scale rock cutting tests to select mechanized excavation machines". *International Journal of Rock Mechanics & Mining Sciences*, Vol.44 (2007) Issue 3, 468-476.
- [7] H. Tuncdemir, N. Bilgin, H. Copur, C. Balci, "Control of rock cutting efficiency by muck size". *International Journal of Rock Mechanics & Mining Sciences*, Vol.45 (2008) Issue 2, 278-288.
- [8] C.X. Luo, C. L. Du, "Influence of drum motion parameters on shearer cutting properties". *Telkomnika*, Vol.12 (2014) No.1, Jan.
- [9] P. John, U.M. Loui, K. Rao, "Numerical studies on chip formation in drag-pickcutting of rock". *Geotechnical and Geological Engineering*, Vol.30 (2011) Issue 1, 145-161.
- [10] O. Su, N. A. Akcin, "Numerical simulation of rock cutting using the discrete element method". *International Journal of Rock Mechanics & Mining Sciences*, Vol.48 (2011) Issue 3, 434-442.
- [11] C.X. Luo, Z.T. Han, Y. Yuan, "Study on thermal-structural analysis for shearer ranging arm shell". *Jordan Journal of Mechanical and Industrial Engineering*, Vol.9 (2015) No. 1.
- [12] Y. Bo, "Numerical simulation of continuous miner rock cutting process". *Dissertation, West Virginia: West Virginia University*, (2005).
- [13] Ajay Goyal, Suresh Dhiman, Shailendra Kumar, Rajesh Sharma, "A Study of Experimental Temperature Measuring Techniques used in Metal Cutting". *Jordan Journal of Mechanical and Industrial Engineering*, Vol.8(2014) No. 2.
- [14] Y. M. Xia, S. J. Nie, Y. Y. Bu, H. M. Zhao, "Distribution properties of cutting tooth's maximum load of spiral mining head for cobalt-crust". *Journal of Central South University: Science and Technology*, Vol.38(2007) Issue 3, 512-516.
- [15] M. Ayhan, E., "Comparison of globoid and cylindrical shearer drums' loading performance". *The Journal of South African Institute of Mining and Metallurgy*, Vol.106 (2006) Issue 1, 51-56.
- [16] B. Mishra, "Analysis of cutting parameters and heat generation on bits of a continuous miner—using numerical and experimental approach". *Dissertation, West Virginia: West Virginia University*, (2007).
- [17] X.P. Li, H. Guo, J.N. Liu, Y.L. Liu, "Dynamical characteristics of the linear rolling guide with numerical simulation and experiment". *Telkomnika*, Vol. 11 (2013) Issue 1, 436-442.
- [18] X. H. Li, B. Song, D. Wang, Q. Y. Lin, "Design and simulation study of man-machine contact surface system for grooving section pattern of horizontal cutting head". *Journal of Liaoning University of Technology: Natural Science Edition*, Vol.29 (2009) Issue 6, 392-395.
- [19] Jerzy Rojek, Eugenio Onate, Carlos Labra, "Discrete element simulation of rock cutting". *International Journal of Rock Mechanics & Mining Sciences*, Vol.48 (2011):996-1010.
- [20] S.Y. Liu, C.X. Luo, "Vibration experiment of shearer walking unit". *Applied Mechanics and Materials*, Vol.268 (2013) Issue 1, 1257-1261.
- [21] S.Y. Liu, C.X. Luo, "Experimental modal research on the cutting system of EBZ-75 type boom-roadheader". *Applied Mechanics and Materials*, Vol. 278-280 (2013), p. 295-298.
- [22] S.Y. Liu, C.L. Du, X.X. Cui, K.D. Gao, "Characteristics of different rock cut by helical cutting mechanism". *Journal of Central South University of Technology*, Vol.18 (2011) Issue 5, 1518-24.
- [23] X. H. Ma, X. W. Yu, Y.M. Lu, Q. J. Tang, "Numerical simulation of shearer drum loads on complex coal seam". *Journal of Hei Longjiang Institute of Science and Technology*, Vol. 22 (2012) Issue 1, 42-46.

# Improving Mixing in Water Aeration Tanks Using Innovative Self-Powered Mixer and Power Reclamation from Aeration Tank

Ammar A. T. Alkhalidi <sup>a</sup>, Patrick Bryar <sup>b</sup>, Ryo S. Amano <sup>b</sup>

<sup>a</sup> Energy Engineering Department - German Jordanian University

<sup>b</sup> Department of Mechanical Engineering - University of Wisconsin-Milwaukee

Received July, 21, 2016

Accepted August, 25, 2016

## Abstract

The primary objective of the present paper is to increase the Standard Oxygen Transfer Efficiency (SOTE) in aeration tank. To achieve this without increasing the power required to pump air into aeration tanks, a mixer and turbine blades were added to the regular fine bubble aeration diffuser. The turbine blade extracts power from the moving water current and transfers this power to the mixer at the top of the diffuser. A support structure was mounted above the air to connect the turbine blade and the mixer on one shaft. Furthermore, an electrical generator was connected to the shaft to extract surplus energy from the system at high flow rates. Results showed that the mixer powered by the turbine blade extracted power induce less oxygenated water into the core of the bubble column without using additional energy. Thus, this system can lead to a more efficient distribution of oxygen within the water tank. Furthermore, it was found that the turbine blade captured more energy than needed by the mixer, the excess energy was collected using electrical generator. Results showed that self-powered mixer increase the SOTE up to 25%. At the same time 11% power used in air pumping can be reclaimed using the electrical generator at high flow rates.

© 2016 Jordan Journal of Mechanical and Industrial Engineering. All rights reserved

**Keywords:** Wastewater Treatment, SOTE, Aeration Tank Mixing, Power Reclamation .

## Nomenclature

COD	chemical oxygen demand.
SOTE	standard oxygen transfer efficiency.
RPM	rotations per minute.
SS2	Silver Series 2 commercial diffuser commonly used in aeration industry.
S-N	Sharp Nub membrane invented by [10]
PIV	particle image velocimetry.

## 1. Introduction

Wastewater treatment facilities strive to increase the efficiency of the process of recycling water to be reused. The aeration process, introduction of pressurized air to collected water through diffusers located at the bottom of the containing tank, consumes 50%-70% of the financial cost invoked within a wastewater purification operation [1]. Aeration process efficiency depends on several factors such as the air mass flow rate, depth of diffuser submergence, and the nature of the contents in the wastewater [2].

Water oxygenation process was investigated by Pankhania *et al.* [3] in a laboratory scale membrane

aeration bioreactor (MABR) with a void volume of 1.35 liters for its ability to treat synthetic wastewater. DeGuzman [4] invented an apparatus for mixing gas and liquid. Levitsky *et al.* [5] studied the water oxygenation in an experimental aerator with different air/water interaction patterns.

New innovative way to improve mixing in the aeration tank without using extra power was investigated by Alkhalidi and Amano [6]; they used a new innovative air injection method to agitation water and air bubble dispersion; hence, the improved OTE in the aeration basin without extra power depletion. Hudnell *et al.* [7] investigated improving wastewater mixing and oxygenation efficiency with solar-powered circulation.

Bubbles behavior under water was investigated by Dani *et al.*'s work [8]. A trail of oxygenated water was observed when air bubbles travel upwards in water, as shown in Fig1.

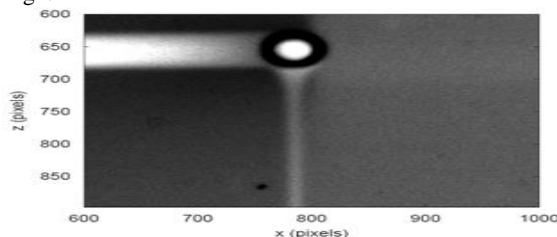


Figure 1. Trail of oxygen behind an air bubble moving upward [8].

\* Corresponding author e-mail: .

Based on the results found by Dani *et al.* [8] when subsequent bubbles travel upwards through the wake of the first bubble, they travel on the same highly oxygenated path. This decreases the effectiveness of the bubble oxygenation due to the reduction in the air concentration gradient between inside and outside the bubble.

The driving force of the aeration process is the difference in oxygen concentration levels that exists inside and outside of the bubble. In the present work, a new innovative method of mixing that induces less oxygenated water into the core of the bubble column to overcome the problem of bubbles traveling on the same oxygenated path, hence the improved oxygenation process.

## 2. Experimental Observation Setup

The observation tank consists of a clear flat panel plexi-glass, 0.9m x 0.9m x 1.2m. This tank was used to mimic the aeration tank in wastewater treatment plant where standard PVC air diffusers 0.23m (9 Inch) are installed at the bottom. The setup was equipped with an accurate pressure regulator flow meter and pressure gages to control the experimental conditions precisely. Bubbles velocity was measured by particle image velocimetry (PIV).

During the experiment, it was observed that when air is allowed through the diffusers installed at the bottom of the aeration tank, it developed a water bubble current within the tank. This current is called 'bubble column' that was created by buoyancy force while driving bubbles toward the water surface. Figure 2 illustrates the currents and the bubble column within the confines of visualization tank used in this work.

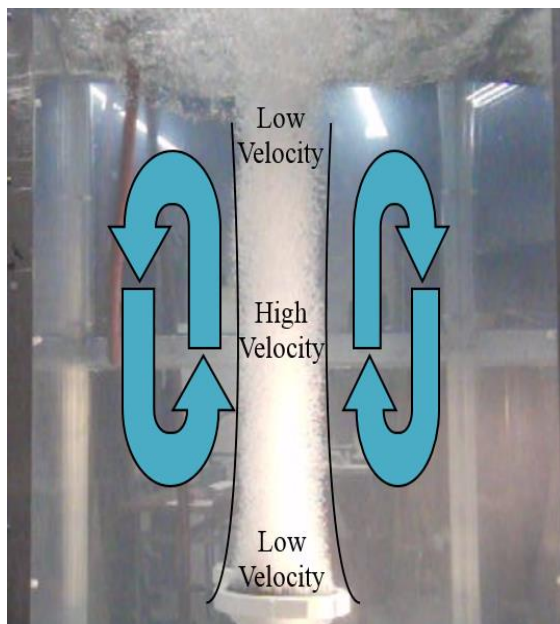


**Figure 2.** Bubble column, collimation of air bubbles as the progress to the surface of the water. Vertical black lines illustrate the uniformity of the column. Teal arrows illustrate the flow of the water current

The bubbles' velocity was measured using PIV at different heights (0, 100, 200, 300, 400 and 500 mm above the membrane) for different flow rates. Results are shown in Fig. 3.

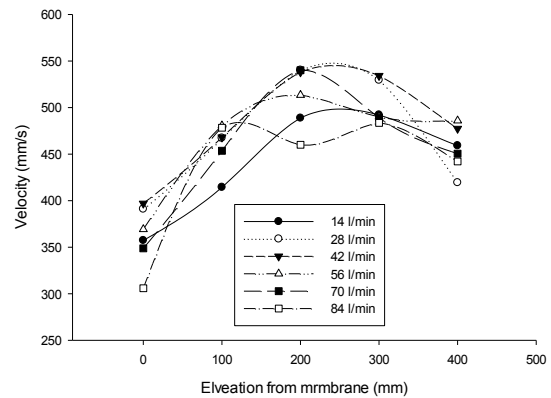


**Figure 3.** water column velocity at different height from membrane and at different flow rates

The results presented in Fig. 3 show that the maximum velocity location is between 200 mm and 300 mm above the membrane. In addition, the minimum velocity occurs right above the membrane.

Both the water current showed in Fig. 2 and the velocity profile showed in Fig. 3 depict that high kinetic energy exists in the middle of the of the bubble column and low energy at both ends of the column. Based on that, a new idea emerged to install a propeller (Turbine) to extract power from the high velocity location in the water column. This extracted power will be used to operate a mixer at the top of the membrane (low velocity region) to induce the mixing in that region. The mixing will drive the less oxygenated wastewater into the water column. Therefore, the oxygen concentration difference between inside and outside the air bubble will increase and, as a result, the SOTE will increase.

A supporting structure, shown in Fig. 4, was designed and built to hold the blade in place. Friction between the rod that holds the propeller and the stabilizers was assumed negligible due to lubrication from the water present in the tank.



**Figure 4.** Supporting structure illustration

The blade installed to extract the power in the middle of the bubble column is a household fan blade with 0.178m diameter.

The mixer installed at the bottom is a costume-made with 0.178m diameter. The self-powered mixer airfoil design assists the middle blade by extracting additional energy from water stream. Mixer blades are twisted upwards for the top blade and downwards for the bottom blade to mix the bubble column. The design of the self-powered mixer enables it to mix the water near the diffuser with small external energy. The mixer, shown in Fig. 5, was built on a rapid prototyping machine and implemented in testing rig for testing.

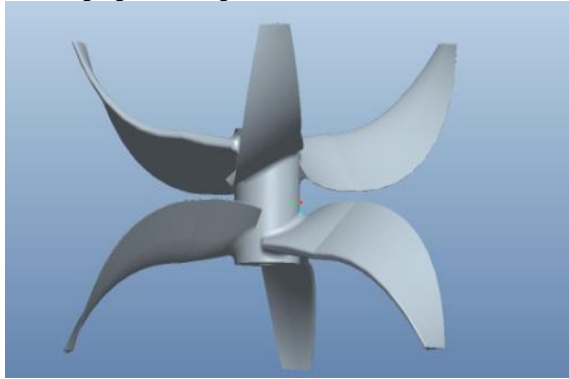


Figure 5. Illustration of the dual blade mixing system.

Test tank and self-powered mixer were built according to the design discussed above. Tests were conducted to investigate the effect of mixing at the top of the membrane on the SOTE.

3. Results

A power generation analysis, based upon resistive load, was conducted by the use of generic generator. The generator was chosen based on its ability to generate high power under a low RPM. This generator was connected directly to the shaft containing the self-powered mixer and the additional blade. Additionally, a 2.5-100 ohm potentiometer was connected in series with this generator. Lastly, a data logging and a generic ohmmeter were connected to the potentiometer in parallel.

For the purpose of the power analysis, the resistive load was measured at intervals from 5 ohms to 95 ohms at increments of 10 ohms. At each iteration, voltage was measured between 850 and 1000 times, and the maximum value was used to determine the peak power generation of the system.

This process was repeated for the airflow rates from 14 l/min to 84 l/min and was varied using 14 l/min intervals. The results from this analysis can be seen in Fig. 6.

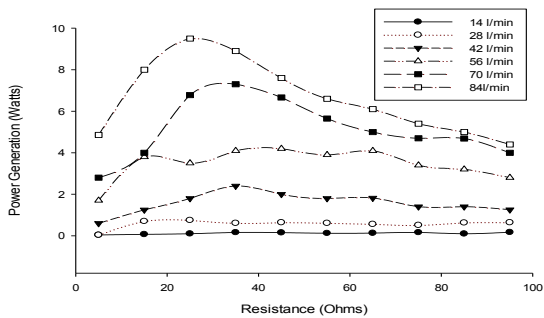


Figure 6. A comparison between power generation and resistive load at different flow rates.

In order to render this information better, a comparison between data generated from newly proposed system and the power used by a generic pond air blower was utilized. It was determined that the blower system was a good comparison point since it consumes all of the power within the water aeration phase of wastewater treatment [9]. A generic pond air blower was chosen based on the head pressures and designed flow rates. Both attributions are comparable to the proposed system within the confinement of the experimental tank. A comparison of the results is shown in Fig. 7.

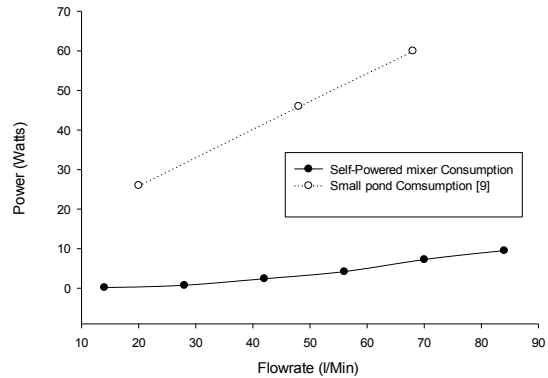


Figure 7. A comparison of power reclamation from self-powered mixer and power requirements of a generic blower small pond consumption [9].

Figure 7 shows that the electrical power consumed by small ponds for air pumping could be reduced up to 80% by installing the new proposed system. One advantage of the proposed system is that it can be added to any existing fine bubble aeration system.

Finally, an SOTE analysis was conducted in compliance with clean water act [10]. SOTE was tested though the use of three dissolved oxygen probes affixed within a cylindrical testing tank 750 L in size to eliminate dead zones in the tank. The self-powered system was tested using two membranes, commercially standard membrane SS2 and the Sharp Nub membrane. Both membranes were tested twice with and without the attachment of the electrical generator.

The Sharp Nub membrane is a laboratory membrane invented by Amano and alkhaldi [11]. It uses a nozzle that forces bubbles to split into three smaller bubbles. Thus, it produces much smaller bubbles than the SS2 membrane. The results are shown in Fig. 8.

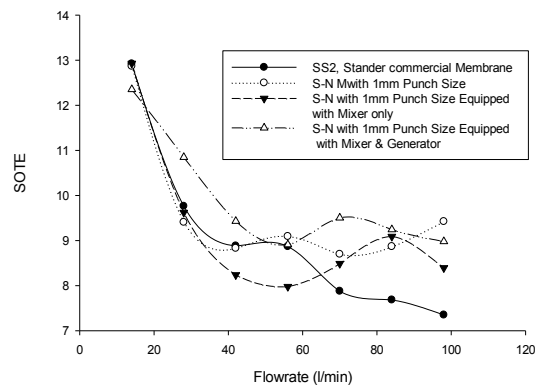


Figure 8. Graphical illustration of resulting SOTE results for sharp-Nub membrane and compared to SS2 rubber diffuser.

The results presented in Fig. 8 indicate an increase in SOTE, at high flow rates, after 60 l/min, for both cases of using the self-powered mixer only and using the self-powered mixer attached to the generator. It should be noted that a resistive load was maintained at 40 ohms, that is, almost at the highest power generation point as shown in Fig. 6.

#### 4. Conclusions

Bubble column velocity was investigated using PIV. It was found that the velocity varies with the depth from the water surface. In the present paper, energy was extracted from a high velocity location in the water column and reapplied at the low velocity regime to improve SOTE distribution. This was achieved by utilizing an innovative self-powered mixer device located right above the membrane combined with turbine blade at the highest velocity location.

The use of the self-powered mixer indicated an increase in SOTE of approximately 25% at high flow rates in the best cases using the Sharp Nub diffuser system. Moreover, results indicate a significant ability to reclaim power, at higher airflow rates. This power reclamation was able to yield gains up to 11%.

#### References

- [1] American Society of Civil Engineering, "A Standard for the Measurement of Oxygen Transfer in Clean Water", 1984, New York, N.Y.
- [2] A. Alkhalidi, & R. Amano, Factors Affecting Fine Bubble Creation and Bubble Size for Activated Sludge. *Water and Environmental Journal*, vol. 29, No 1, 2015, pp. 105-113.
- [3] M. Pankhania, K. Brindle, and T. Stephenson, Membrane aeration bioreactors for wastewater treatment: completely mixed and plug-flow operation, *Chemical Engineering Journal*, Vol. 73, No. 2, 1999, pp. 131–136.
- [4] V. DeGuzman, Apparatus for mixing gas and liquid, 1994, Patent number US 5376311 A
- [5] S. Levitsky, L. Grinis, J. Haddad, and M. Levitsky, Water oxygenation in an experimental aerator with different air/water interaction patterns. *HAIT Journal of Science and Engineering B*, Vol. 2, No. 1-2, 2005, pp. 242-253.
- [6] A. Alkhalidi, H. Al Ba'ba'a and R. Amano, Wave generation in Subsurface Aeration System: A New Approach to Enhance Mixing in Aeration Tank in Wastewater Treatment. *Desalination and Water Treatment*, 2016, DOI:10.1080/19443994.2016.1172263.
- [7] H. Hudnell, D. Green, R. Vien, S. Butler, G. Rahe, B. Richards, and J. Bleth, *Clean Technologies and Environmental Policy*, Vol. 13, No. 5, 2011, pp 731-742.
- [8] A. Dani, F. Guiraud, A. Cockx, "Local measurement of oxygen transfer around a single bubble by planar laser-induced fluorescence", *Chemical Engineering Science*, Vol. 62, No. 24, 2007, pp. 7245-7252.
- [9] C. Tucker, "Pond Aeration", SRAC publication, September 2005.
- [10] ASCE, *Front Matter and Software, Measurement of Oxygen Transfer in Clean Water: ANSI/ASCE 2-91*, 1993, pp. i–x, doi: 10.1061/9780872628854.fm.
- [11] Amano R. and Alkhalidi A., Membrane for Air Diffuser, 2013, Patent number US 20130099401 A1.

# Novel Approach to Enhance the Performance of Production Systems Using Lean Tools

Hazem Kaylani <sup>\* a</sup>, Ahmad Almuhtady <sup>b</sup>, Anas M. Atieh <sup>a</sup>

<sup>a</sup> School of Applied Technical Sciences, Industrial Engineering Department, German Jordanian University, Amman Madaba Street, Amman, Jordan

<sup>b</sup> School of Applied Technical Sciences, Mechanical and Maintenance Engineering Department, German Jordanian University, Amman Madaba Street, Amman, Jordan

Received May, 16, 2016

Accepted June, 25, 2016

## Abstract

Value Stream Mapping (VSM) is a tool used for analyzing the current state of a production system and designing a future state by analyzing and improving the flow of material and reducing inefficiencies. However, aiming at improving performance without considering potential machine failures and other uncertainties in the production process may lead to an inaccurate future value stream map.

The purpose of the present study is to introduce a novel approach that combines discrete event simulation, Design Of Experiments (DOE), and Failure Modes and Effects Analysis (FMEA) to enhance the VSM processes. Simulation modeling is utilized to evaluate production system performance and the severity of potential failure modes under several operational conditions. FMEA and DOE are then used to select the best systems enhancements which can be used to generate future map. The results of our approach show that failure modes can drastically affect the system performance if not taken into consideration, resulting in a non-representative future VSM. The proper selection of operational levels can reduce the severity of failures and at the same can provide high performance levels.

© 2016 Jordan Journal of Mechanical and Industrial Engineering. All rights reserved

**Keywords:** Value Stream Mapping (VSM); simulation; Design Of Experiments (DOE); Failure Mode and Effect Analysis (FMEA); process flowchart; enhancement algorithm; glass fabrication case study.

## 1. Introduction

Value stream mapping, design of experiments, and simulation are three independent lean tools that are used in industrial engineering. Failure mode and effect analysis has been used to detect potential failure modes in engineering systems. A conceptual infusion model that integrates the four tools is proposed in the present study.

Rother and Shook (1999) provided the guideline for the procedure of VSM in manufacturing. VSM is a process-oriented tool that helps visualize the processes where both materials and information are mapped (Bin et al., 2016; Rohac and Januska, 2015; Tyagi and Vadrevu, 2015). VSM includes two themes; Current State Map (CSM) and Future State Map (FSM) (Ar and Al-Ashraf, 2012). The CSM includes the current production health status and any potential non-value added activities. The non-value added might include long lead-times, processing delays, and improper handling/utilization of resources. The second theme is FSM, which might be considered as an updated version (with reduced non-value adding activities) of the

current value state map. The FSM produces a more lean principle system, that will result in more balanced production line and is more focused towards “pull system” where each process only produces the quantity and quality that is required by the following process (Lu et al., 2011; Rother and Shook, 1999). It has been argued that sometimes VSM is not capable of standing alone due to its static nature; thus, for VSM to be efficient, other tools are necessary to improve the efficiency of VSM (Flores, 2015). While these tools are numerous, common examples include discrete event simulation and design of experiments (Abdulmalek and Rajgopal, 2007; Agyapong-Kodua et al., 2009; Ali et al., 2015; Gurumurthy and Kodali, 2011; Jasti and Sharma, 2014; Lu et al., 2011; McDonald et al., 2010; Rohana et al., 2013; Woehrlé and Abou-shady, 2010; Xia and Sun, 2013; Xie and Peng, 2012).

Simulation is a great tool that makes it possible to visualize processes, helps in alternative selections, and optimizes operations (Alrabghi and Tiwari, 2014). It has become as a proved tool for enhancing performance in facilities and organizations. Furthermore, simulation provides a virtual environment that can mimic the actual

\* Corresponding author e-mail: Hazem.Kaylani@gju.edu.jo.

environment. Thus, simulation not only complements lean concepts, but also highlights feasible options. This last point can solve the fundamental limitation of VSM (static manual nature), giving it a dynamic perspective (Abdulmalek and Rajgopal, 2007; Gurumurthy and Kodali, 2011; Khalid et al., 2014; McDonald et al., 2010, 2002; Sigari and Clark, 2013; Swallmeh et al., 2014; Xia and Sun, 2013).

Design Of Experiments (DOE), also referred to as designed experiment or experimental design, is a useful tool used to predict the interrelation between experimental factors by developing proper factorial design. Factorial design facilitates the study of the effects that several factors may simultaneously have on a process. When performing an experiment, varying the levels of the factors at the same time is both time and cost efficient, and allows for the study of interactions between the factors. DOE is performed under controlled conditions where a selected process' inputs (factors), which may have impact on the selected process' outputs (responses), are investigated. Depending on the number of factors and the size of the problem, two types of factorial designs can be used. Full factorial experiments are used when dealing with a small number of levels, as responses are measured at all combinations of the factor's levels. For larger problems, it is not feasible to do that, hence fractional factorial design is used to minimize time and cost where information about high order interactions are excluded (Montgomery, 2015).

Conventional VSM does not take into consideration potential failures of the production system explicitly; faults or failures can significantly disrupt the production. These failures are usually listed under what is known as failure modes. For example, a machine breakdown in the system can be considered a failure mode. The degradation of the quality of the produced parts, or incorrect dimensions can be considered as a failure mode or a failure mode effect depending on whether the cause is known or not. For instance, if the latter is caused by the degradation of the machine tool through usage, the degradation of the machine tool itself is the failure mode and the degradation of the quality is a failure mode effect.

While these failures are mostly potential possibilities, their impacts are important enough to affect the decision-making. Failures in the production system have received significant attention in the literature. The efforts targeted the prevention or reduction of these failures (and in some cases accommodating their occurrence) over two main levels. The higher-level is concerned with maintenance-related decision-making (such as the evolution of maintenance policies, paradigm, and maintenance-influenced production policies) (Du et al., 2014; Liu et al., 2015; Paciarotti et al., 2014).

The lower-level is concerned with process-related maintenance (such as the continuous development in sensory and fault detection and estimation techniques).

Tools were developed to assist in each of these levels and in many cases to link them together. For example, the Remaining Useful Life (RUL) is estimated from techniques developed in the lower level and represents an important asset (tool) for the decision-making in the higher level.

One of the most useful tools that join both levels is the Failure Modes and Effects Analysis (FMEA). FMEA is a

step-by-step systematic tool for identifying all possible failures in a design, a manufacturing or assembly process, or a product or service (Almannai et al., 2008; Chen and Ko, 2009; Chen and Wu, 2013; Ekmekcioglu et al., 2012; Paciarotti et al., 2014; Wu et al., 2014). FMEA ranks them, and prioritize the highest impact item on the system (Paciarotti et al., 2014).

It studies one failure mode in the system at a time, as complex systems with multi-failures components are impractical to analyze especially when the a series of different effect combination exists (Paciarotti et al., 2014; Xiaoa et al., 2011). FMEA, could be applied in many different industries (Oldenhofa et al., 2011; Paciarotti et al., 2014; Xiaoa et al., 2011). Information gathered and listed in FMEA can be of qualitative (descriptive) or quantitative forms. For instance, in addition to listing all potential failure modes, a description of their potential effects, their potential causes or mechanisms, the current process controls, and the recommended actions can be incorporated in the FMEA presentation.

Literature reveals that several efforts have been made to integrate the previously mentioned tools towards achieving enhancements. Integrating simulation and DOE is found in (Avenida et al., 2007; Li et al., 2014). VSM and simulation (Ali et al., 2015; Helleno et al., 2015; Tyagi and Vadrevu, 2015), and FMEA with DOE (Fahmy et al., 2012; Senthilvelan, 2014; Shishebori et al., 2015).

The objective of the present study is to integrate VSM, DOE, FMEA along with discrete event simulation. Figure 1 clarifies the mutual added value of using these tools simultaneously. The benefit of VSM in both stages, CSM and FSM, is to visualize the processes and identify the potential areas of enhancement. DOE provides the variable input of the simulation model. Simulation helps to assess the current state map, compare the output scenarios of DOE, and provide information for FSM. FMEA will assess the severity of failures, and its impact on Key Performance Indicators (KPI). The approach, detailed in an algorithmic setup in the next section, is capable of achieving a more efficient and a less costly process improvement. It is worthwhile to mention that this approach was evaluated using a real case study in a leading glass-fabrication facility.

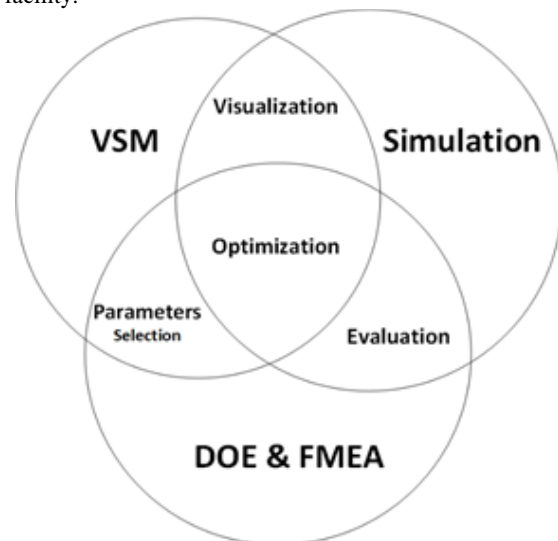


Figure 1. Integration of VSM, Simulation, DOE and FMEA

## 2. Methodology

The integrated approach is detailed in Figure 2. The production operations of a major glass factory in Jordan are considered as the main example, but the approach is generic enough to allow for numerous applications and setups. After the data is collected, product families, process boundaries, and material flow are identified.

### 2.1. VSM-CSM

Initially, a VSM representing the CSM of the production facility is established (see Figure 3). It will help

to visualize process flow as well as identify production status and any potential alerts (Andons) that might cause problems to the production system. For example, the CSM in Figure 3 illustrates the different processes involved in the glass production. Details of these processes are available in previous work (Atieh *et al.*, 2015). According to the production logbook (historical data) and CSM, four processes are identified as major (shown in blue in fig. 3); these are Cutting, Edging, Drilling, and Tempering. The other five processes are identified as minor as their contribution to the total production represents less than 10%

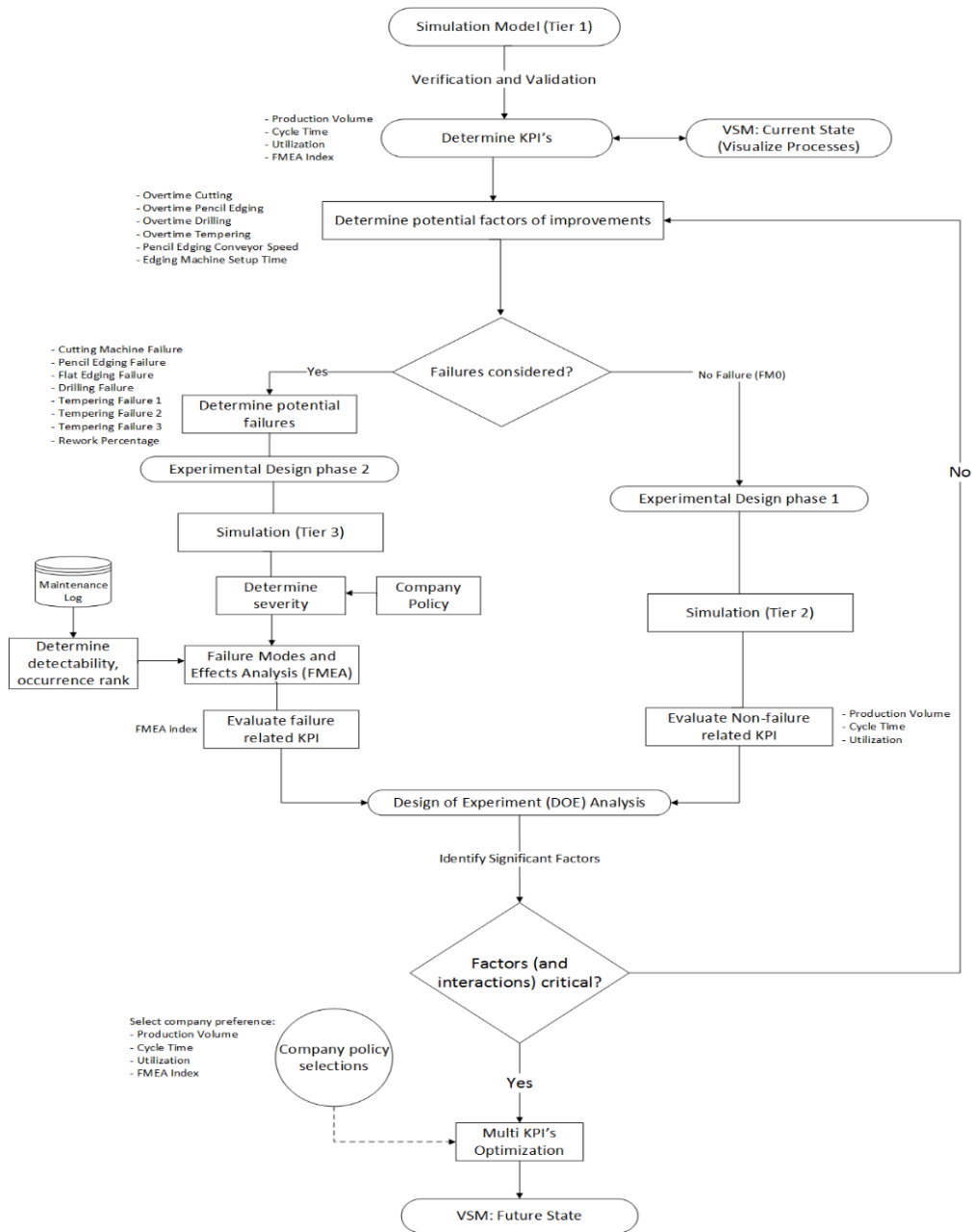


Figure 2. Algorithm Framework

## 2.2. Simulation Model

After analyzing historical data related to production rates, available resources, setup times and process times, a simulation model representing the current operations at the production facility is created. The model of the case study, which was built using Arena-Rockwell Automation Technologies Software version 14.7, was developed to incorporate rework as it reflects in terms of cost that is added to the process. The model covers all production resources at the glass factory and was verified to mimic the logic of the actual production flow at the factory. Validation was also performed by comparing results to real production data. It is recommended that any simulation model is set to run for several replications with ample run length to achieve steady state. In the present study, 10 replications and 160 days were chosen, respectively. Preliminary tests indicate that 14 days warm-up period is needed to remove any bias in the results. The model is capable of evaluating different KPIs given any combination of input factors' levels (detailed in next section). Three variations of the simulation model are created: Tier 1, Tier 2, and Tier 3. Tier 1 is used in the preliminary runs to evaluate CSM for potential problematic areas. Tier 2 is used after the design of experiments, and Tier 3 is used with the FMEA analysis.

## 2.3. Determining Input Factors and Responses (KPIs)

In order to analyze and improve the process in any system, two sets of information have to be identified: the outputs (responses or KPIs) with which improvement can be measured, and the input factors, which can affect the outputs. Only feasible factors need to be considered.

Based on company policy, it is found that three performance measures: daily production volume (KPI-1), resources utilizations (KPI-2), and production lead times (KPI-3) are the most desirable in terms of evaluating the system performance. While it is customary to evaluate these KPIs within the normal healthy operational conditions, one can anticipate the severity of the numerous potential failures on them. Therefore, while these KPIs will be evaluated at the healthy conditions, an additional KPI has been devised (FMEA index: KPI-4) to cover for the failure modes and their potential effects. Details of this KPI are provided in Section 2.5.

With regard to KPI-1, the daily production volume is estimated from simulation by averaging the production of one month. The assessments of utilizations are not straightforward, especially with unavailable quality data (for the calculation of the Overall Equipment Efficiency (OEE)). Therefore, we devise the utilization index (KPI-2) which is discussed separately in Section 2.3.1. The production lead time (KPI-3) is calculated based on the average flow time of all products produced during a one month period.

In our case study, the following input factors are considered as being feasible. First, overtime is introduced on the following machines: cutting machine, pencil edging machine, drilling machine, and tempering machine. For all machines, overtime manifests in an additional four operational hours to the 8-hour shift. Additionally, and as indicated in the previous work (Atieh *et al.*, 2015), pencil edging represents a challenge in the production time due to long setup and process times. Therefore, the company is interested in evaluating the option to reduce the setup time and/or increase the conveyer speed by investing in a new setup through certain machine upgrades. This results in six feasible input factors.

### 2.3.1. Utilization Index

The utilization index is adopted as KPI-2. It compares the improvement (or worsening) of the utilization of the resources in the system against its nominal value in the default setup (all factors at low level). On the one hand, it is known that excessive utilization of resources (or machines) reduces their life expectancy, and increases the probability of failures. On the other hand, under-utilized resources represent investment, which has not been fully exploited. Therefore, popular optimal utilization values are in the range of 80-90%.

We propose to evaluate the utilization index for every experiment (combination) through the following equation:

$$U_i = \sum_{j=1}^N w_j [|U_j^* - U_{0j}| - |U_j^* - U_{ij}|]$$

$\forall j = 1, \dots, N$  resources (machines)

$\forall i = 1, \dots, n$  experiments (combinations)

where  $U_i$  is the utilization index for the  $i^{\text{th}}$  experiment (combination);

$w_j$  is the weighted factor associated with the utilization of the  $j^{\text{th}}$  resource (or machine) in the system;

$U_j^*$  is the optimal utilization value of the  $j^{\text{th}}$  resource (or machine);

$U_{0j}$  is the nominal utilization value of the  $j^{\text{th}}$  resource (or machine) in the default setup (all factors at low level);

$U_{ij}$  is the utilization value of the  $j^{\text{th}}$  resource (or machine) in the  $i^{\text{th}}$  experiment (combination).

$U_j^*$  can be determined from Original Equipment Manufacturer (OEM) recommendations or from the organization's policy. The weighted factors reflect the importance of a particular resource in reference to the collective resources. For example, the percentage of the production, which utilizes a specific resource, can be used to determine its utilization-weighted factor.

The target optimal utilization value was set to 75% for all the resources (machines); it is considered in our case study based on the company's policy. The targeted resources (machines) in the utilization index are from the four major processes (5 machines) indicated earlier: cutting, edging (pencil or flat), drilling and tempering.



## 2.4. Design of Experiments

The DOE is used to create the factorial design for the experimental runs on the input factors and their levels. The DOE considered all the input factors, with a suitable number of levels for each. For our case study, we consider the above six input factors, with each at two levels, resulting in a total of 64 runs for full factorial design. Two phases of DOE are performed; Phase 1 is concerned with experimental design and analysis of the production system behavior without considering effect of failure. Responses KPI-1, KPI-2, and KPI-3 are evaluated at all combinations of the experimental factors' levels using simulation model Tier-2.

After analyzing the factorial design, the best design is found using the desirability approach (Derringer G, 1980; "Design of Experiments, Minitab user Manual," 2005).

For the scenarios when at least one failure mode exists, DOE phase 2 utilizes the same input factors mentioned above but uses KPI-4 as a response variable, namely failure modes and effects analysis index (FMEA-Index). KPI-4 takes into consideration the effect of failure mode severity on system performance and is obtained by applying Severity Analysis, which is explained in section 2.5. Simulation Tier 3 is used to evaluate severity of potential failures on system performance for the given 64 experimental runs.

If the input factors and their interactions are found to be non-significant or do not provide a reasonable enhancement, another set of feasible factors must be considered. Otherwise, the DOE phase is finished with the understanding of the relationship between the input factors (and their interactions) and the responses.

## 2.5. Failure Mode and Effect Analysis (FMEA)

Potential failures, which may affect the KPIs, have to be identified. Their potential effect is to be studied in order to assist the DOE phase and what follows it in terms of analysis. A modified FMEA procedure (in reference to the standard one (Defeo, 2014)) is utilized. The procedure transforms the severity rate into a measure for the failures effects on the KPIs under study. Details of this are available in Section 2.5.1. The rest of the FMEA standard procedure (potential effect(s) of failure, its cause(s)/mechanism(s), occurrence and detectability rates) can be obtained from historical data and/or maintenance logs. Occurrence rates are calculated by counting the number of incidents that a certain failure has occurred.

Then this number is normalized to the standard range of FMEA (1 for the failure mode with least frequency of occurrence and 10 for the most frequent one).

The detectability rate indicates how much design control can detect potential cause/mechanism and subsequent failure mode. This is very dependent on the process/system at hand and the potential failures of concern.

After calculating the severity rate (Section 2.5.1), the Risk Priority Number (RPN) of each failure mode at each combination of input factors/experiment can be easily

obtained by multiplying the severity rate, the occurrence rate, and the detectability rate.

In order to combine all the RPNs for a specific experiment into one representative value (namely FMEA-Index), a weighted average can be used if all the RPNs are within the same order. However, averaging is well-known to be sensitive to extreme values. Therefore, while this method statistically covers for the failure modes with high RPN (important to take into consideration), it is also affected by the low RPNs. Therefore, a simple augmentation to the previously mentioned method of combining the RPNs is to exclude the lowest 10% of RPNs from the averaged pool.

In reference to our case study, failures in production systems are quite common, leading to major production problems (Andons) in terms of reduced production rates and/or increased production lead time. Table 1 lists the FMEA for our case. These failure modes are identified based on historical data including the maintenance logbook of machine failures and feedback provided by production personnel regarding the most critical failures. Insignificant failures with extremely low occurrences and/or related to extremely underutilized resources have been disregarded, and only the most frequent eight have been listed. Table 1 lists as well, times to repair machines. Since these times do not depend on previous repair tasks, the Exponential distribution is used to simulate the Mean Time To Repair (MTTR).

### 2.5.1. Severity Analysis

The association of a severity rating in the FMEA is extremely important as it

directly affects the risk priority number from which the FMEA index will be

calculated. While the occurrence rating and the detectability rating can be evaluated from maintenance logs, the severity is almost ambiguous and can only be estimated when joining maintenance logs with production ones. To overcome such a problem, we introduce a simulation-based severity rating procedure that takes into consideration the organization's policy.

First, the maintenance logs are used to identify the time to repair for the main failure modes chosen in the design of the FMEA. Then, the failures are input into the simulation model, and runs are made to estimate the impact of each of these failure modes on the KPIs of interest. Expectedly, the period during which the failure mode is introduced, and the days after it are studied extensively. The failure modes are as well introduced to each experiment (combination) of enhancing factors.

The KPIs of interest resulting from the healthy (no fault) mode and the ones resulting during the failure mode are compared for each combination. In order to combine the contributions of the different KPIs, a weighted average inspired from the organization's policy can be used. For example, a production facility can have a severity index which focuses on the production volume, lead time, and combined resources utilization. This will result into an equation such as:

$$S_{ik} = w'_1 * \frac{L_{ik} - L_{i\phi}}{L_{i\phi}} + w'_2 * \frac{P_{i\phi} - P_{ik}}{P_{i\phi}} + w'_3 * \left[ \sum_{j=1}^N w_j [|U_j^* - U_{ij\phi}| - |U_j^* - U_{ijk}|] \right]$$

$\forall k = 1, \dots, M$  Failure modes ;  $\forall j = 1, \dots, N$  resources;

$\forall i = 1, \dots, n$  experiments (combinations)

where  $S_{ik}$  is the  $k$ th severity index for the  $i$ th experiment (combination);

$w_{1'}$ ,  $w_{2'}$ , and  $w_{3'}$  are the weighted factors associated with the different KPIs (lead time, production volume, resource utilization) changes because of failure;

$L_{ik}$  is the lead time in the  $i$ th experiment during the  $k$ th failure mode;

$L_{i\phi}$  is the lead time in the  $i$ th experiment during the no failure (no fault) mode;

$P_{ik}$  is the production volume in the  $i$ th experiment during the  $k$ th failure mode;

$P_{i\phi}$  is the production volume in the  $i$ th experiment during the no failure (no fault) mode;

$w_j$  is the weighted factor associated with the utilization of the  $j$ th resource (or machine) in the system;

$U_j^*$  is the optimal utilization value of the  $j$ th resource (or machine);

$U_{ij\phi}$  is the utilization value of the  $j$ th resource (or machine) in the  $i$ th experiment (combination) during the no failure (no fault) mode;

$U_{ijk}$  is the utilization value of the  $j$ th resource (or machine) in the  $i$ th experiment (combination) during the  $k$ th failure mode.

Finally, the severity index for each failure mode at each combination are transformed to the standard FMEA one to ten rating with ten being the most severe failure mode.

No.	Potential Failure Mode	MTTR (Hrs)	Potential Effect(s) of Failure	Sev	Potential Cause(s)/ Mechanism(s) of Failure	Occur	Detect	RPN	Recommended Action(s)
1	Cutting Machine Failure	16	Non-straight cuts (Harder to Edge), Incorrect product dimensions	Function of experiment (combination)	Degraded machine tool and/or parts: Oil pump, knives, etc. miscalibration	2	2	Sev x Occur x Detect	Replace or calibrate cutting diamond
2	Flat Edging Machine Failure	20	Rough Edges Or breakage of panels / Increased WIP		Conveyor system: loose conveyer belt, motor dysfunction, jammed , miscalibration, etc.	9	3		Replace polishing and/or diamond wheels OR Adjust feed rate
3	Pencil Edging Machine Failure	20	Rough Edges Or breakage of panels / Increased WIP		Conveyor system: loose conveyer belt, motor dysfunction, miscalibration, etc.	8	4		Install Tool Detectors
4	Drilling Machine Failure	4	Panels breakage / Increased WIP		Degraded machine tool: Broken Drill Pneumatic press failure	8	7		Ensure the table is stable OR replace cutting diamond OR adjust feed rate
5	Tempering/ Furnace Failure 1	16	Stalling products/Increased WIP		Conveyor system	8	5		Check and/or replace rollers (if they absorb heat differently they affect the heat distribution)
6	Tempering/ Furnace Failure 2	45.6	Excessive unbalanced expansion of glass leading to breakage		Heating system: Heaters malfunction, relays, chiller, etc.	7	2		Check and/or replace heaters (heat distribution needs to be equal)
7	Tempering/ Furnace Failure 3	16	Products characteristics that do not meet customer requirements (e.g. strength)		Control/sensors	7	4		Install new detectors and frequent calibrations
8	Rework% increase	N/A	Increased WIP, increased cost, increased product lead time		Various: Human errors, improper machine set up. cumulative machine tools degradation, etc.	7	10		Systematic inspections of tools and products, Modify manufacturing procedure, Apply lean manufacturing tools

2.6. Optimal Solution

While DOE provides the statistical analysis to describe the relationship between the responses (KPIs) and the input factors, it does not explicitly provide the optimal solution for a given response or a combination of responses. Nonetheless, it facilitates it through the regression equations generated in the DOE analysis stage.

The optimization can be achieved using the desirability function approach to find the best solution. First individual desirability is obtained for each KPI according to the targets set for each. Second, the composite desirability is determined using weighted geometric mean of the individual desirabilities. Finally, a reduced gradient algorithm with multiple starting points that maximizes the composite desirability is applied to determine the numerical optimal solution (Derringer G, 1980; “Design of Experiments, Minitab user Manual,” 2005).

Optimized solutions are obtained for several scenarios by setting different weights for the response variables. The weights should be selected according to the organization’s policy. The more failure-conscious the organization would like to be, the larger the weight assigned to the FMEA-index must be. The methodology will be more efficient if solutions for individual KPIs are investigated first then different combinations using several weights are considered. Finally, a subjective selection of one of solution will be made by consulting with the organization’s management.

For our case study a solution that will maximize KPI-1 and KPI-2, and minimize KPI-3 and KPI-4 is sought.

3. Results and Discussion

Implementing the algorithmic procedures detailed

above for our case study and using Arena® simulation software version 14.7 and Minitab® 17.1.0, the following results are obtained.

3.1. DOE Factorial Plots

DOE factorial plots are generated for individual response variables to determine significant input factors for each of these responses individually.

3.1.1. Production Volume

Inspection of Figure 4 reveals that the most critical factor to improve the daily production rate is the tempering overtime factor indicating the necessity of increasing the availability of tempering resources, mainly the furnace. All other factors were found to be insignificant in terms of our case study. We also note here that inspection of the interaction plots showed that the input factors do not interact with each other in terms of this response variable.

3.1.2. Utilization-Index

Unlike the production volume, the Utilization-Index KPI is affected by all input factors. It can be improved by adding more overtime to the bottleneck tempering machine and reduce time on the other less-busier machines; drilling, pencil edging, and cutting. This is expected since Utilization-Index measures the deviation of machine utilization from the company’s target utilization of 75%.

The results show that drilling station current utilization is about 70% and increasing time availability of this machine reduces the utilization to 31% distancing it further from the target value. Once again, the interaction between different input factors was found to be minimal.

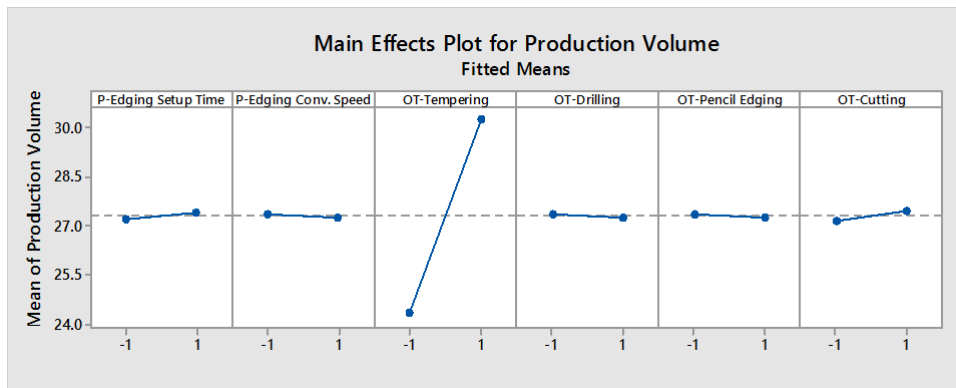


Figure 4. Main Effect plot for production volume

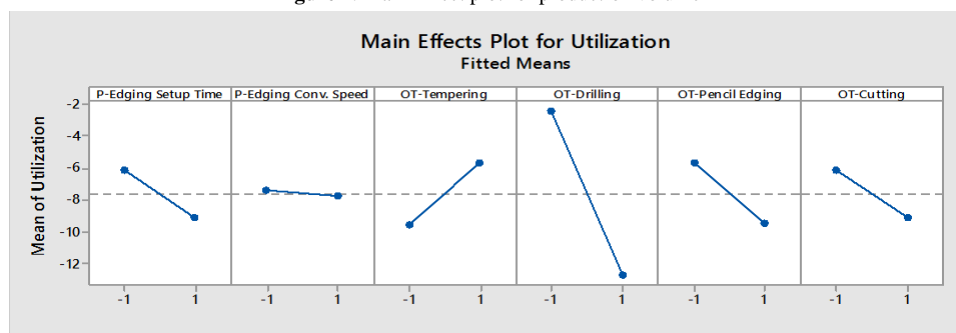


Figure 5. Main Effect plot for utilization

3.1.3. Lead Time

Similar to Production Volume, this KPI is mainly affected by overtime on tempering input factor. To reduce lead time it is imperative to increase tempering machine availability. This is intuitive, as the tempering machine has been shown to be a primary bottleneck (Atieh *et al.*, 2015). Once again, the interaction between different input factors was found to be minimal.

3.1.4. FMEA-Index

As the production system at hand has several under-utilized machines, failure modes have been found to be significant particularly for the lead time. Additionally, the lead time is considered one of the most important performance measures the company is looking to enhance. Therefore, the severity index has been chosen to evaluate the severity of the failure over the lead time.

Unlike the previous KPIs, this response variable indicates complex behavior with the different input factors. For example, on the one hand overtime on tempering is shown in Figure 7 to increase the FMEA-Index as a single response affected by a single factor. However, interaction between input factors (see Figure 8) is shown to be strong and in our case can invert the effect of the single factor. The figure shows that the reduction of the setup time on the pencil edging machine will reverse the effect of the overtime on tempering.

This outcome is explained by the fact that both resources have high utilizations and are considered as potential bottlenecks in the production system. Overtime on tempering will generally relieve the production system (enhancing all its KPIs). Therefore, failures will result in a potential loss of this relief, and hence the FMEA-Index will increase when this input factor is considered on its own. Nonetheless, this factor can (with the interaction of

other factors) reduce the FMEA-Index. Particularly, there is a strong cross over interaction between overtime on tempering machine and setup time of pencil edging machine with P-value of 0.019.

This explains why overtime on tempering will be chosen for all the optimal solutions detailed later coupled with a reduced pencil edging setup time or increased conveyer speed. If both have been selected together, the rate of work flow will increase and once the failure occurs (for example at tempering), the WIP increases at the other resources leading to an increase in waiting times. That will reflect on the lead time and consequently worsens the FMEA-Index value. Furthermore, not selecting both input factors will once again highlight the criticality of the tempering machine during failure in a similar manner to not having overtime on tempering (default setup-all factors at low level).

Pencil edging overtime is also a significant factor and Figure 7 shows that it should have higher value to reduce FMEA-Index. In addition, Figure 8 shows that overtime on drilling and cutting machines have strong crossover interaction indicating that having overtime on either one of them should be sufficient.

It is clear that since the FMEA-Index is designed to measure the potential loss of enhancement a change of input factor(s) can provide, in addition to the fact that the enhancement is measured in terms of several KPIs, it will be almost impossible to track physically every input factor's effect. Therefore, statistical analysis such as this approach becomes important. This is in line with the fact that changing an input factor will have dynamic effects on the whole production system and not only on a single machine or component. This can only be captured through simulation which results were used in the DOE analysis.

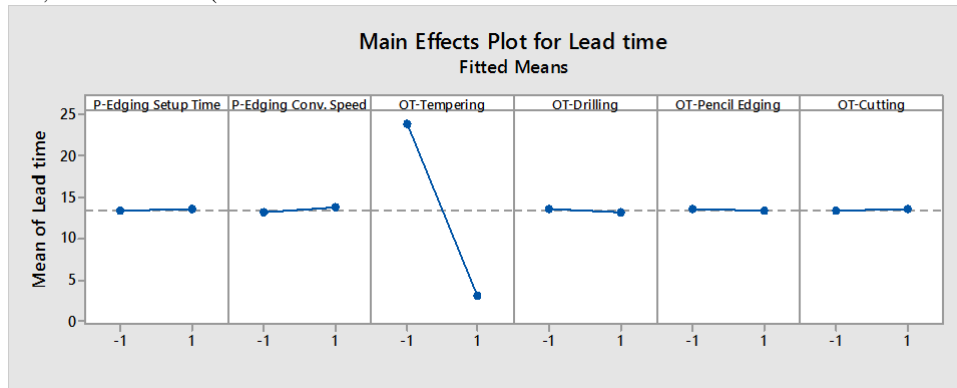


Figure 6. Main Effect plot for lead time

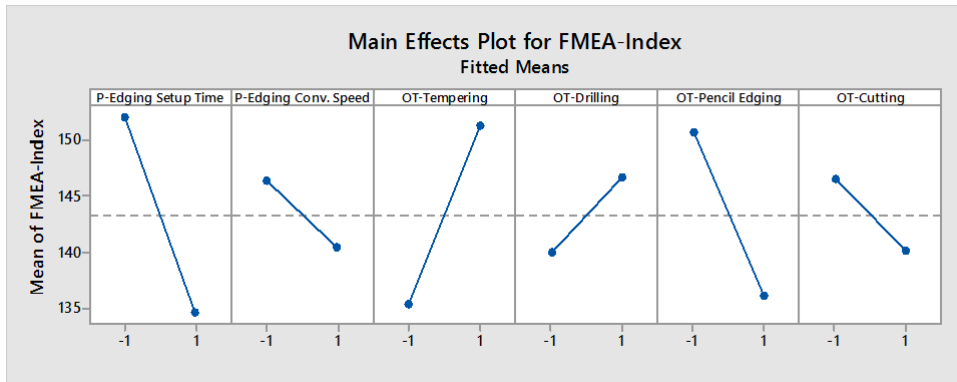


Figure 7. Main Effect plot for FMEA-Index

3.1.5. Joint View

For all four KPIs, the input factor; over time on tempering is the most significant one with highest slope indicating the urgent need to increase the availability of the tempering machine. This result is expected as the preliminary analysis showed that this process is considered as a bottleneck. Introducing overtime on tempering will not only increase productivity and decrease lead time but also the utilization mean effect plot indicates that it is not recommended to have any overtime on other machines except for the tempering as all other machine are underutilized and increasing availability time will reduce their utilization way under the target value of 75%. However, the FMEA-Index plots illustrate some important interactions that can help reduce it, and consequently reduce the risk of failure. To decide the best combination of input factors, optimization is performed using several scenarios as illustrated in the following section.

3.2. Optimization Analysis

Optimization analyses are performed and compared for each single response variable individually and for a selection of weighted combinations of all responses together. The three best solutions for each scenario are considered in the comparison.

3.2.1. Single Response

Optimization analysis for each response separately resulted in a slightly different set of combination factors as illustrated in Figure 9. The numbers between brackets represent the response value for each solution. Some of the obtained levels of input factors were common among most solutions, for example, all solutions show that overtime on tempering is needed for all scenarios, pencil edging overtime is needed considering Production volume, Lead Time, and FMEA-Index but not recommended when considering Utilization-Index. All four charts show significant enhancement in the value of each response variable compared to no-improvement scenario. Best production volume obtained was 33.51 panels/day while best lead time was 1.73 days. To decide what would be a

good combination of input factors that will optimize all four responses simultaneously multiple-response optimization is discussed in the following section.

3.2.2. Multiple Responses

To find a solution that will enhance all responses simultaneously, optimization was carried on several combinations of response variables using different weights. The weights were selected carefully to be in line with company policy. Mainly three of these combinations are illustrated in Figures 10, 11, and 12.

In Figure 10, the optimization was performed mainly on the three traditional responses; Production volume, Utilization, and Lead time while a 0% without consideration of the FMEA-Index. First, it can be clearly seen that the results drastically enhances the two main KPIs, lead time and production volume. The optimizer was switching between focusing on enhancing the production volume, lead time and utilization. For example, the production volume has the best value in solution 1, the lead time has the best value in solution 3, while the utilization has the best value in solution 2. One important issue regarding the provided solutions is the large value of the FMEA-Index associated with them, indicating that these solutions present preferable outcome in the healthy mode and are susceptible to failure.

Figures 11 and 12 consider all KPIs including FMEA-Index. Therefore, different sets of solutions have been generated with set in Figure 12 focusing on the production volume. It can be seen from the figures that a solution which does not compromise the enhancements in the traditional KPIs and the FMEA-Index can be attained. We note that achieving the best possible value in all KPIs simultaneously is not achievable. While some solutions achieve excellent levels in some KPIs, other KPIs are less or not enhanced at all. Nonetheless, we recommend generating enough solutions with different sets of weights in order to create a reasonable pool of alternatives from which one solution is subjectively selected.

In the case study, the best solution was selected to be solution 1 produced with weights as; 40% for production volume, 20% for overall resources utilizations, 20% for lead time, and for 20% FMEA-Index.

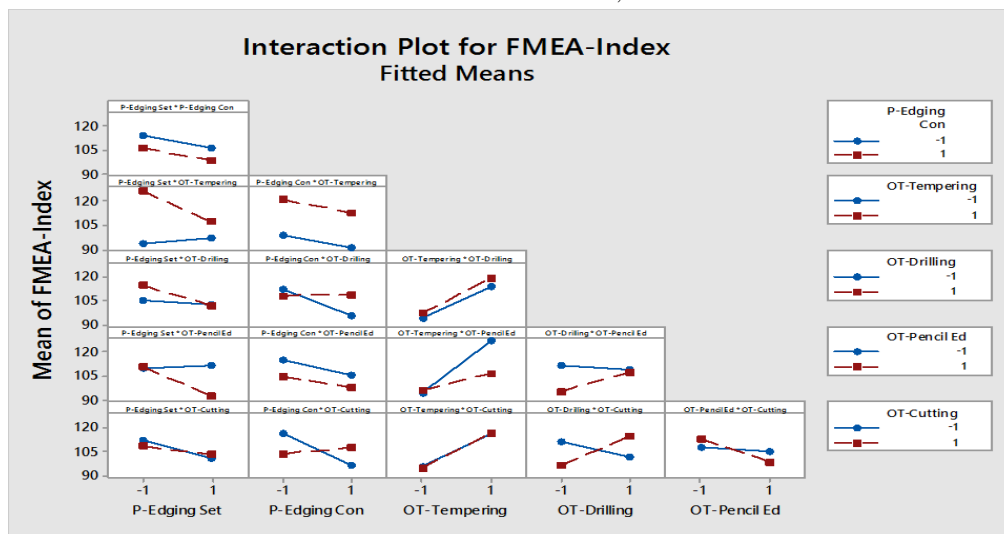


Figure 8. interaction plot for FMEA-Index

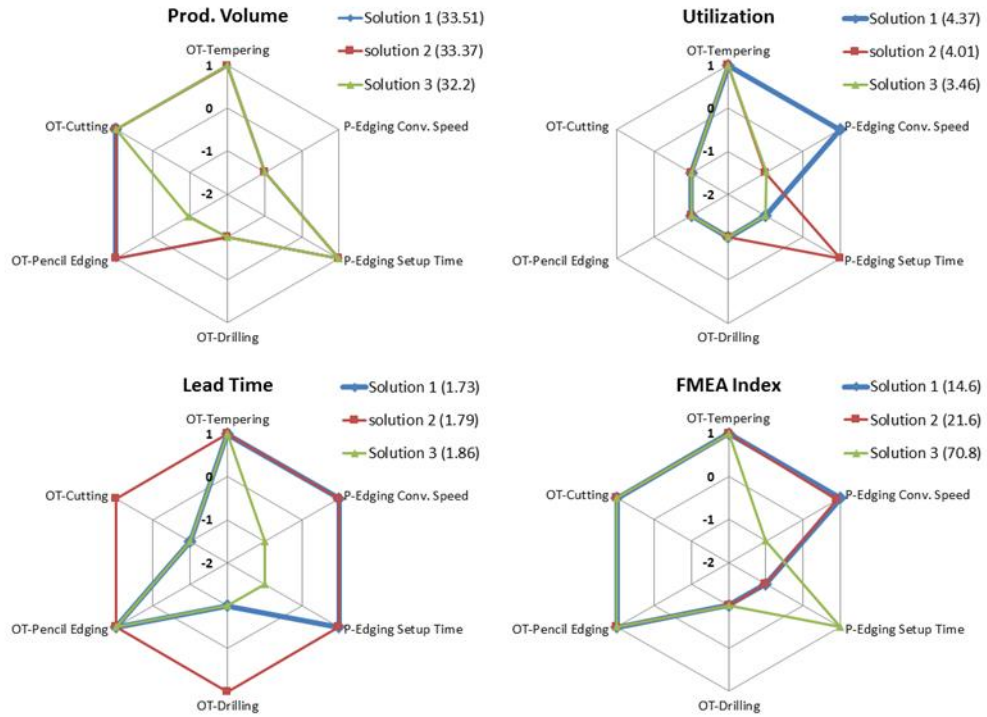
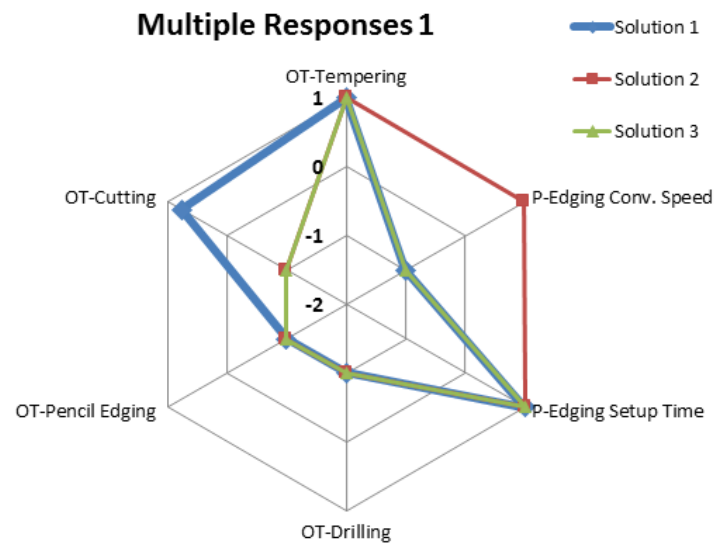


Figure 9. Single response optimization



	Vol. Production	Utilization	Lead Time	FMEA Index
<b>Weight in Opt.</b>	40%	30%	30%	0%
<b>Solution 1</b>	31.9	-1.07	3.12	159.1
<b>Solution 2</b>	31.6	0.13	4.80	90.5
<b>Solution 3</b>	30.2	4.37	2.66	148.9

Figure 10. Multiple responses optimization 1

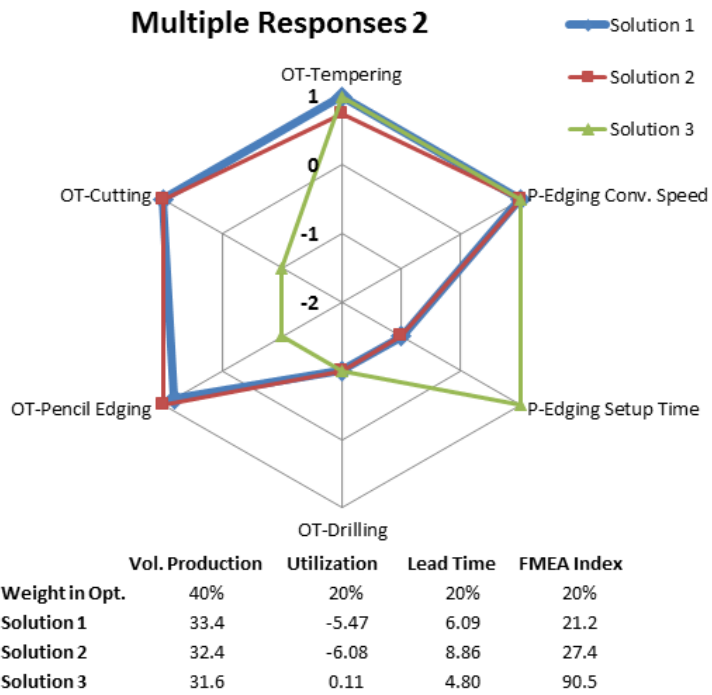


Figure 11. Multiple responses optimization 2

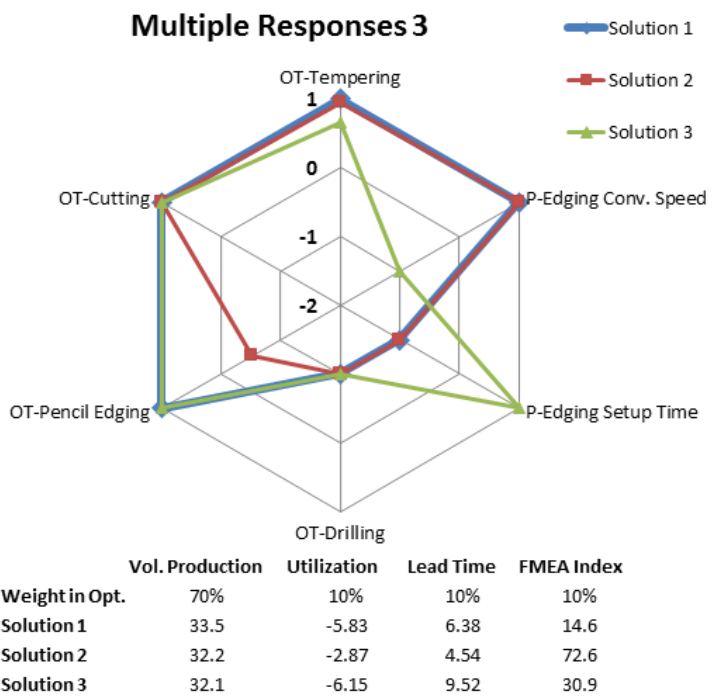


Figure 12. Multiple responses optimization 3

### 3.3. VSM-FSM

VSM-FSM was constructed as an extra evaluation methodology to measure the enhancement in the production system. The FSM values were updated using the output of simulation model as illustrated in Figure 13. Based on the selected optimized solution described in Section 3.2, for multiple-response variables, a significant enhancement in system performance was observed. Considering the production volume, the daily production in square meters was increased from 24.7 panels/day (220 sqm) to 33.4 panels/day (298 sqm). This increase, represent a 35% enhancement in daily production volume. In addition, the work in process WIP for all four major processes (highlighted in blue) were dramatically reduced

except for tempering. For example the WIP for drilling, was reduced from 368 to 35 sqm. While tempering process WIP increased from 635 to 831 sqm, this increase is justified by the increase in daily production volume. Consequently, the overall lead times was reduced for all processes by 56%. While cycle times were enhanced by 5%. This enhancement is a result of the infusion of all previous mentioned tools described above in the new proposed methodology. The utilization of all machines was observed to either be reduced or stayed constant. The major reduction in machine utilization was on tempering which was reduced from 99.99% to 89.9%. Hence, this case study can prove that the application of proposed algorithm can result in major enhancement of production performance.

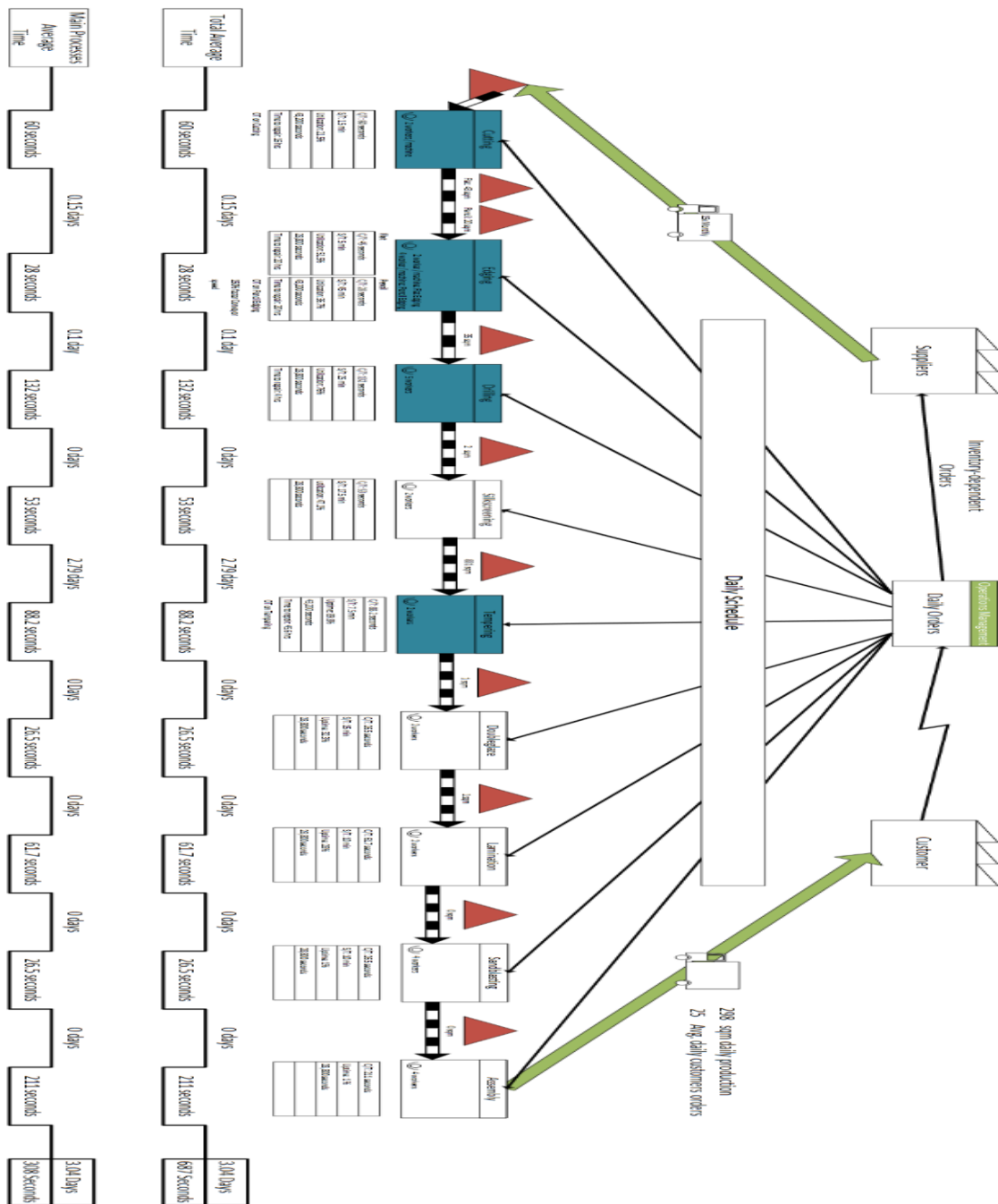


Figure 13. VSM-future state map (FSM)

#### 4. Conclusion

Different types of failures can occur in any production system, causing interruptions to production process, leading to lower production rates and increased lead times. Planning resources to meet production requirements without considering the risk of failures can lead to catastrophic consequences to any organization. Although VSM is used for planning future system improvements, it does not explicitly take into consideration risk of failures. In the present study, we

show that the VSM procedure can be improved considerably by utilizing three lean tools: FMEA, discrete event simulation, and DOE. The proposed methodology offers a valuable contribution since it helps to optimize several KPIs simultaneously, identify critical factors affecting production, assess severity of different failures, and select the best levels of factors that will maximize performance and reduce risk of failures.

We have demonstrated the effective use of our methodology by applying it to a real case study of glass-fabrication facility. Results show that introducing four-hour overtime on a tempering station will enhance system performance considerably. This is expected as the utilization of the furnace is very high, over 95%, and is considered a bottleneck in the production process. However, the Utilization-Index and FMEA-Index plots show that other factors are also significant. Improving the Utilization-Index will help in having a more balanced production system, but should not be considered alone as it may deteriorate important performance measures, like production volume and lead time. In addition, several interactions between input factors were identified which can help in selecting proper levels of input factors. Results also show that neglecting to consider risk of failure might lead to an unrealistic estimate of production volume. Selecting input factors carefully can reduce the failure risk, but still produce good values of other KPI's.

#### References

- [1] Abdulmalek, F.A., Rajgopal, J., 2007. Analyzing the benefits of lean manufacturing and value stream mapping via simulation: A process sector case study. *Int. J. Prod. Econ.* 107, 223–236. doi:10.1016/j.ijpe.2006.09.009
- [2] Agyapong-Kodua, K., Ajaefobi, J.O., Weston, R.H., 2009. Modelling dynamic value streams in support of process design and evaluation. *Int. J. Comput. Integr. Manuf.* 22, 411–427. doi:10.1080/09511920802527574
- [3] Ali, N. Bin, Petersen, K., Bernard, B., Franc, N. De, 2015. Evaluation of simulation assisted value stream mapping : two industrial cases. *Inf. Softw. Technol.* 68, 45–61.
- [4] Almannai, B., Greenough, R., Kay, J., 2008. A decision support tool based on QFD and FMEA for the selection of manufacturing automation technologies. *Robot. Comput. Integr. Manuf.* 24, 501–507. doi:10.1016/j.rcim.2007.07.002
- [5] Alrabghi, A., Tiwari, A., 2014. State of the art in simulation-based optimisation for maintenance systems. *Comput. Ind. Eng.* 82, 167–182. doi:10.1016/j.cie.2014.12.022
- [6] Ar, R., Al-Ashraf, M., 2012. Production Flow Analysis through Value Stream Mapping: A Lean Manufacturing Process Case Study. *Procedia Eng.* 41, 1727–1734. doi:10.1016/j.proeng.2012.07.375
- [7] Atieh, A.M., Kaylani, H., Almuhtady, A., Al-tamimi, O., 2015. A value stream mapping and simulation hybrid approach: application to glass industry. *Int. J. Adv. Manuf. Technol.* doi:10.1007/s00170-015-7805-8
- [8] Avenida, J.A.B.M., Pinho, A.F. de, Leal, F., Marins, F.A.S., 2007. APPLICATION OF DESIGN OF EXPERIMENTS ON THE SIMULATION OF A PROCESS IN AN AUTOMOTIVE INDUSTRY José, in: *Proceedings of the 2007 Winter Simulation Conference.* pp. 1601–1609.
- [9] Bin, N., Petersen, K., Schneider, K., 2016. FLOW-assisted value stream mapping in the early phases of large-scale software development. *J. Syst. Softw.* 111, 213–227.
- [10] Chen, L.-H., Ko, W.-C., 2009. Fuzzy linear programming models for new product design using QFD with FMEA.pdf. *Appl. Math. Model.* 33, 633–647. doi:10.1016/j.apm.2007.11.029
- [11] Chen, P.-S., Wu, M.-T., 2013. A modified failure mode and effects analysis method for supplier selection problems in the supply chain risk environment: A case study. *Comput. Ind. Eng.* 66, 634–642. doi:10.1016/j.cie.2013.09.018
- [12] Defeo, J., 2014. *Juran's Quality Management and Analysis* 6th Ed. McGraw-Hill Education.
- [13] Derringer G, S.R., 1980. Simultaneous Optimization of Several Response Variables. *J. Qual. Technol.* 12, 214–219.
- [14] *Design of Experiments, Minitab user Manual*, 2005.
- [15] Du, Y., Mo, H., Deng, X., Sadiq, R., Deng, Y., 2014. A new method in failure mode and effects analysis based on evidential reasoning. *Int. J. Syst. Assur. Eng. Manag.* 5, 1–10. doi:10.1007/s13198-014-0218-5
- [16] Ekmekcioglu, Mehmet, Kutlu, Ahmet, C., 2012. A Fuzzy Hybrid Approach for Fuzzy Process FMEA: An Application to a Spindle Manufacturing Process 5, 611–626. doi:10.1080/18756891.2012.718104
- [17] Fahmy, R., Kona, R., Dandu, R., Xie, W., Claycamp, G., Hoag, S.W., 2012. Quality by Design I: Application of Failure Mode Effect Analysis ( FMEA ) and Plackett – Burman Design of Experiments in the Identification of “ Main Factors ” in the Formulation and Process Design Space for Roller-Compacted Ciprofloxacin Hydrochloride I. *AAPS PharmSciTech* 13, 1243–1254. doi:10.1208/s12249-012-9844-x
- [18] Flores, E., 2015. Evaluating Lean Manufacturing Proposals through Discrete Event Simulation – A Case Study at Alfa Laval Master thesis work 30 credits , Advanced level Sönke Detjens.
- [19] Gurumurthy, A., Kodali, R., 2011. Design of lean manufacturing systems using value stream mapping with simulation: A case study, *Journal of Manufacturing Technology Management.* doi:10.1108/17410381111126409
- [20] Helleno, A.L., Pimentel, C.A., Ferro, R., Santos, P.F., Oliveira, M.C., Simon, A.T., 2015. Integrating value stream

- mapping and discrete events simulation as decision making tools in operation management. *Int. J. Adv. Manuf. Technol.* 1–8. doi:10.1007/s00170-015-7087-1
- [21] Jasti, N.V.K., Sharma, A., 2014. Lean manufacturing implementation using value stream mapping as a tool: A case study from auto components industry. *Int. J. Lean Six Sigma* 5, 89–116. doi:10.1108/IJLSS-04-2012-0002
- [22] Khalid, N.K.M., Hashim, A.Y.B., Salleh, M.R., 2014. On Value Stream Mapping and Its Industrial Significance. *J. Ind. Intell. Inf.* 2, 88–90. doi:10.12720/jiii.2.2.88-90
- [23] Li, M., Yang, F., Wan, H., Fowler, J.W., 2014. Simulation-based experimental design and statistical modeling for lead time quotation. *J. Manuf. Syst.* 37, 362–374. doi:10.1016/j.jmsy.2014.07.012
- [24] Liu, H.-C., You, J.-X., Shan, M.-M., Shao, L.-N., 2015. Failure mode and effects analysis using intuitionistic fuzzy hybrid TOPSIS approach. *Methodol. Appl. Soft Comput.* 19, 1085–1098. doi:10.1007/s00500-014-1321-x
- [25] Lu, J.-C., Yang, T., Wang, C.-Y., 2011. A lean pull system design analysed by value stream mapping and multiple criteria decision-making method under demand uncertainty. *Int. J. Comput. Integr. Manuf.* 24, 211–228. doi:10.1080/0951192X.2010.551283
- [26] McDonald, T., Van Aken, E., Rentes, A., 2010. Utilising Simulation to Enhance Value Stream Mapping: A Manufacturing Case Application. *Int. J. Logist. Res. Appl.* 5, 213–232. doi:10.1080/13675560210148696
- [27] McDonald, T., Van Aken, E., Rentes, A., 2002. Utilising Simulation to Enhance Value Stream Mapping: A Manufacturing Case Application. *Int. J. Logist. Res. Appl.* 5, 213–232. doi:10.1080/13675560210148696
- [28] Montgomery, D.C., 2015. *Design and Analysis of Experiments*. Wiley.
- [29] Oldenhofa, M.T., Leeuwena, J.F. van, Nautaa, M.J., Kastea, D. de, Odekerken-Romboutsa, Y.M.C.F., Vredembregta, M.J., Wedaa, M., Barendsa, D.M., 2011. Consistency of FMEA used in the validation of analytical procedures. *J. Pharm. Biomed. Anal.* 54, 592–595.
- [30] Paciarotti, C., Mazzuto, G., D’Ettorre, D., 2014. A revised FMEA application to the quality control management. *Int. J. Qual. Reliab. Manag.* 31, 788–810. doi:10.1108/IJQRM-02-2013-0028
- [31] Rohac, T., Januska, M., 2015. Value Stream Mapping Demonstration on Real Case Study. *Procedia Eng.* 100, 520–529. doi:10.1016/j.proeng.2015.01.399
- [32] Rohana, A., Nooririnah, O., Isa, H., Kamat, S.R., Mehad, M.P., 2013. Lean waste analysis and improvement using dynamic value stream mapping. *Glob. Eng. Technol. Rev.* 3, 1–8.
- [33] Rother, M., Shook, J., 1999. *Learning to See: Value Stream Mapping to Add Value and Eliminate MUDA* Spi Edition. Lean Enterprise Institute, Brookline, MA.
- [34] Senthilvelan, A.M.T., 2014. Optimizing Process Parameters of Screw Conveyor (Sugar Mill Boiler) Through Failure Mode and Effect Analysis (FMEA) and Taguchi Method. *J. Fail. Anal. Prev.* 14, 772–783. doi:10.1007/s11668-014-9887-2
- [35] Shishebori, D., Akhgari, M.J., Noorossana, R., Khaleghi, G.H., 2015. An efficient integrated approach to reduce scraps of industrial manufacturing processes: a case study from gauge measurement tool production firm. *Int. J. Adv. Manuf. Technol.* 76, 831–855. doi:10.1007/s00170-014-6273-x
- [36] Sigari, S., Clark, R., 2013. Applying lean thinking to improve the production process of a traditional medium-size British manufacturing company. *Int. J. Inf. Oper. Manag. Educ.* 5, 154–169.
- [37] Swallmeh, E., Tobail, A., Abo-hamad, W., Gray, J., Arisha, A., 2014. Integrating Simulation Modelling and Value Stream Mapping for Leaner Capacity Planning of an Emergency Department. *Sixth Int. Conf. Adv. Syst. Simul.*
- [38] Tyagi, S., Vadrevu, S., 2015. Immersive virtual reality to vindicate the application of value stream mapping in an US-based SME. *Int. J. Adv. Manuf. Technol.* 1259–1272. doi:10.1007/s00170-015-7301-1
- [39] Woehrle, S.L., Abou-shady, L., 2010. Using Dynamic Value Stream Mapping And Lean Accounting Box Scores To Support Lean Implementation. *Am. J. Bus. Educ. AJBE* 3, 67–76.
- [40] Wu, Z., Ming, X.G., Song, W., Zhu, B., Xu, Z., 2014. Nuclear Product Design Knowledge System Based on FMEA Method in New Product Development. *Arab. J. Sci. Eng.* 39, 2191–2203. doi:10.1007/s13369-013-0726-7
- [41] Xia, W., Sun, J., 2013. Simulation guided value stream mapping and lean improvement: A case study of a tubular machining facility. *J. Ind. Eng. Manag.* 6, 456–576. doi:10.3926/jiem.532
- [42] Xiaoa, N., Huanga, H.-Z., Lia, Y., Hea, L., Jinb, T., 2011. Multiple failure modes analysis and weighted risk priority number evaluation in FMEA. *Eng. Fail. Anal.* 18, 1162–1170.
- [43] Xie, Y., Peng, Q., 2012. Integration of value stream mapping and agent-based modeling for OR improvement. *Bus. Process Manag. J.* 18, 585–599. doi:10.1108/14637151211253747





الجامعة الهاشمية



المملكة الأردنية الهاشمية

المجلة الأردنية  
للمهندسة الميكانيكية والصناعية

JJMIE

مجلة علمية عالمية محكمة  
تصدر بدعم من صندوق البحث العلمي

<http://jjmie.hu.edu.jo/>

ISSN 1995-6665

# المجلة الأردنية للهندسة الميكانيكية والصناعية

## مجلة علمية عالمية محكمة

المجلة الأردنية للهندسة الميكانيكية والصناعية: مجلة علمية عالمية محكمة تصدر عن  
الجامعة الهاشمية بالتعاون مع صندوق دعم البحث العلمي في الأردن

### هيئة التحرير

#### رئيس التحرير

الأستاذ الدكتور أحمد الغندور.

قسم الهندسة الميكانيكية و الصناعية، الجامعة الهاشمية، الزرقاء، الأردن.

#### الأعضاء

الأستاذ الدكتور ناصر الحنيطي  
الجامعة الاردنية

الأستاذ الدكتور محمد أحمد حمدان  
الجامعة الاردنية

الأستاذ الدكتور محمد هياجنه.  
جامعة العلوم والتكنولوجيا الاردنية

الاستاذ الدكتور نسيم سواقد.  
جامعة مؤتة

الاستاذ الدكتور أمين الريبيدي.  
جامعة البلقاء التطبيقية

### فريق الدعم

#### تنفيذ وإخراج

م . علي أبو سليمة

#### المحرر اللغوي

الدكتور قصي الذبيان

ترسل البحوث إلى العنوان التالي

رئيس تحرير المجلة الأردنية للهندسة الميكانيكية والصناعية

الجامعة الهاشمية

كلية الهندسة

قسم الهندسة الميكانيكية

الزرقاء - الأردن

هاتف : 00962 5 3903333 فرعي 4537

Email: [jjmie@hu.edu.jo](mailto:jjmie@hu.edu.jo)

Website: [www.jjmie.hu.edu.jo](http://www.jjmie.hu.edu.jo)